NORTHWESTERN UNIVERSITY

The Hierarchical Structure and Graded Chemical Distribution of Human Enamel

A DISSERTATION

SUBMITTED TO THE GRADUATE SCHOOL

IN PARTIAL FULFILLMENT OF THE REQUIREMENTS

for the degree

DOCTOR OF PHILOSOPHY

Field of Materials Science and Engineering

By

Karen A. DeRocher

EVANSTON, ILLINOIS

September 2020

ABSTRACT

The Hierarchical Structure and Graded Chemical Distribution of Human Enamel

Karen A. DeRocher

Biological organisms have the extraordinary ability to form mineral structures with unparalleled control. From curved single crystals to hierarchically structured skeletal parts, biomineralization processes produce materials with properties that are highly optimized for their intended applications. These processing techniques occur at ambient conditions using materials abundant in the environment, and therefore represent a much more sustainable synthesis process than many industrial manufacturing techniques. Herein we report the characterization of one such biomineral: human dental enamel.

Human enamel exhibits an ordered structure across many length scales, from the millimeter down to the nanometer. Enamel must bear masticatory forces for decades, and its mechanical properties are therefore optimized for toughness, hardness, and wear resistance. Using scanning transmission electron microscopy (STEM) and atom probe tomography (APT), we established that the hydroxyapatite (OHAp) crystals in enamel have a core-shell architecture with a core where the concentration of impurity elements (Mg, Na, F, C) is relatively high, surrounded by a relatively pure shell region. The chemical gradients in the core may contribute to toughening of the crystallites, strengthening the material as a whole.

In order to better understand how an insulating material such as hydroxyapatite evaporates in the atom probe, we performed an analysis of multi-hits generated during an experimental run.

This analysis suggested that there is some mobility of ions on the sample tip, and that phenomena such as the generation of neutral oxygen atoms may contribute to slight compositional inaccuracies in APT data.

At larger length scales, synchrotron x-ray microdiffraction experiments on thin sections of enamel revealed that crystallites are roughly co-aligned along their crystallographic c-axes in enamel rod head regions, with more deviations in the tail and interrod regions. This analysis provided evidence that the crystallite volume changes systematically within a rod, pointing to possible compositional differences in crystallites within the same rod. Additionally, crystallite counting suggests that the crystallites are not a single coherent domain, but are divided by incoherent domain boundaries along the long dimension of the crystallites.

Finally, preliminary APT analysis of teeth affected by molar incisor hypomineralization (MIH) and fluorosis allows us to determine what changes result structurally and chemically from these conditions. MIH and fluorosis do not seem to disrupt the core-shell architecture of crystallites, but do affect the bulk concentration of trace elements. Analysis of the surface zone and body of an artificial sub-surface carious lesion suggests that the crystallite structure has been more dramatically altered. There is also evidence that ions and potentially organic molecules from the solutions used to create the lesion infiltrated into the enamel and were found in the body of the lesion. Improved understanding of how these conditions affect enamel on the nanoscale may aid in the development of novel prevention and treatment techniques.

ACKNOWLEDGEMENTS

This work would not have been possible without the help and support of many people. First and foremost I would like to thank my advisor, Prof. Derk Joester, for sparking my interest in the unique field of biominerals. His support and guidance over the years has allowed me to explore the intricacies of enamel, as well as collaborate on other projects across many different research areas.

I would also like to thank my committee members, Professor Vinayak Dravid, Professor David Seidman, and Professor Stuart Stock for their insightful discussions and guidance. Additionally, I would like to thank Stuart for all of his help designing and running experiments at the advanced photon source (APS) at Argonne National Laboratory. His depth of knowledge on x-ray techniques specifically in the field of teeth and other biominerals was invaluable.

To my parents, for their constant love and support. I truly wouldn't have been able to do this without you guys. To Jonathan and Yi, thank you for lending your experience and wisdom during times I really needed it, and for all the pictures and videos of Rachel and Esther that would always brighten my day. Mary, thank you for always being there to listen when I needed someone to talk to. Mark, thank you for the hours of video games, board games, puzzles, and funny videos to make me laugh during stressful times.

I would like to thank all of the Joester group members, both past and present: Lyle Gordon, for pioneering the use of APT on enamel (and other biominerals) and always making time to answer my questions about Mathematica code or how to interpret x-ray data sets. Michael Cohen, thank you for getting me involved in this project and teaching me how to use the FIB and atom

probe. Emmie Campbell, thank you for the countless coffee runs and for continuing to be a supportive friend. Michael Whittaker, thank you for being a great sounding board for experimental ideas and interpretation of data. Paul Smeets, thank you for all your efforts, especially with the Nature paper. I learned so much from you throughout the writing process and during your time in our group, and I truly could not have asked for a better co-first author! Linus Stegbauer, thank you for sharing your knowledge of synthesis, and for the many silly conversations and debates in the office. Robert Free, thank you for being such a great colleague and friend. Between all the trips to Argonne and the time spent taking care of rats, I learned so much from you and can't thank you enough for all the insights and ideas you shared. Allessandra DiCorato, thank you for always being there to listen and offer advice. Whether it was a question about research, needing a document proofread, or something going on outside of work, you were always willing to take the time to help out and I'm extremely grateful; also thank you for being my Tomate buddy, getting giant burritos was often the highlight of my week! Victoria Cooley thank you for always being so supportive, for continuing the enamel project, and for always being such a good resource for experimental ideas, data analysis techniques, and interesting podcasts. Jessica Walker, Bradley Moreno, Danielle Duggins, and Utthara Rameshbabu: thank you for being such a wealth of scientific knowledge, and also for your friendship and for contributing to a collaborative and close-knit group dynamic. Finally to the rest of the group members, thank you so much for being an important part of this process.

To all the people I have had the privilege of collaborating with during my time at Northwestern: Professor James Rondinelli, thank you for the helpful discussions and for offering your group's expertise on performing density functional theory calculations; Professor Prasanna

Balachandran, thank you for performing the calculations that became such an important part of our findings; Professor Lena Kourkoutis, Berit Goodge, and Michael Zachman, thank you for your assistance performing STEM experiments, and helping us understand and analyze the data that was collected; Professor Ana Bedran-Russo, thank you for giving us an additional prospective on our enamel studies, and for supplying us with many teeth that we used for our analysis; Professor Sophia Houari-Mejri, thank you for expanding our interests into additional dental diseases like molar incisor hypomineralization and fluorosis.

I'd also like to thank the dedicated staff and scientists at Northwestern core-facilities, at Argonne National Lab, and at CAMECA without whom none of this would be possible. Dieter Isheim, thank you for your extensive knowledge of atom probe tomography, from sample prep all the way to data analysis. You have been such a great resource for gathering and interpreting data. Ben Myers, Karl Hagglund, and Paul Smeets, thank you for all the help on the FIB, and for all your hard work keeping it up and running. Carla Shute, thank you for your assistance cutting and polishing samples and preparing them for future analysis. Dr. Ruqing Xu, thank you for your assistance with micro-diffraction experiments at Argonne National Lab. Finally to Katherine Rice for assisting with our first experiments on the improved atom probe; these experiments were pivotal to us gaining a clearer understanding of the structure of enamel crystallites, and informed our future analysis.

To the rest of my Northwestern friends. Ha-Kyung thank you for being such a great friend, roommate, and running buddy. From camping to half marathons to running Ragnar, many of my best memories from grad school were things we did together. To the rest of the cohort: Karl, Yue, Sam, Say, Sarah, Amit, and Charlotte, thank you for the hours of fun, food, and general good times.

To Garrett and Christie, thank you for being the best roommates I could have asked for. Garrett, thank you for all the delicious food, and for all the hilarious hypothetical questions and stories that made the apartment such a fun place to come home to. Christie, thank you for the hours of trying to figure out new recipes, the Friday night Jet's and Bambu, and for always being there to listen and commiserate over struggles with work or with matters outside the lab. You've become such a great friend and I will miss you so much!

To my Tier One family: Adriana, Mike, April, Vicki, Bob, Jen, Curtis, and Luci, thank you for the hours of training together, the jokes, the funny videos, and for so many "just one mores." You guys became such an important part of my time in Chicago, and I will miss you all.

Finally, Shawn, thank you for your love and support through all the ups and downs over the last several years. For being there when I needed to advice, for celebrating with me when things went well, and for constantly pushing me to be a better scientist and person. I truly couldn't not have done it without you, and I'm so grateful for all the experiences we've shared and will continue to share.

TABLE OF CONTENTS

LIST OF TABLES

LIST OF FIGURES

1.   INTRODUCTION

1.1   MOTIVATION

Biological organisms exhibit the extraordinary ability to form mineralized tissues with unparalleled control. From curved single crystals to skeletal parts with many levels of organization, biomineralization processes can be used to create very intricate structures with order spanning many length scales.[1-2] Synthetic and industrial processes used to fabricate such complex materials would undoubtedly require large amounts of energy, with many fabrication steps and tight control over environmental factors such as temperature, pressure, pH, and purity of precursor materials. Biological organisms, on the other hand, achieve this goal using bottom-up processes under ambient conditions with materials that are abundant in their environment.

The ability to learn from, and ultimately mimic, these biological processes is of particular interest to the scientific and engineering communities. Such methods could enable the creation of novel materials with desirable mechanical and chemical properties without the use of extreme conditions or expensive (and potentially toxic) precursor materials. While biominerals have been, and continue to be extensively studied, in many cases the exact mechanisms behind the mineralization process is not well understood. One complication is that these materials can be difficult to characterize at each length scale of their hierarchical structure. Their inherent structural complexity often makes conventional characterization techniques difficult, if not impossible. Herein we discuss our attempts to overcome some of these obstacles while investigating human tooth enamel.

1.2 MATRIX-MEDIATED BIOMINERALIZATION

Biomineralization processes fall into two categories. First, mineralization may be organic matrix-mediated, when an organism creates an organic framework into which ions are introduced and where they will then crystallize. In these processes the mineral type, crystallographic orientation, and structure are all controlled by genetics (**Figure 1.1a**).[3] The second type of biomineralizaton is biologically-induced. In this case, there is no matrix to affect the crystallization processes, so crystal habits are similar to those produced inorganically (**Figure 1.1b**).[3]
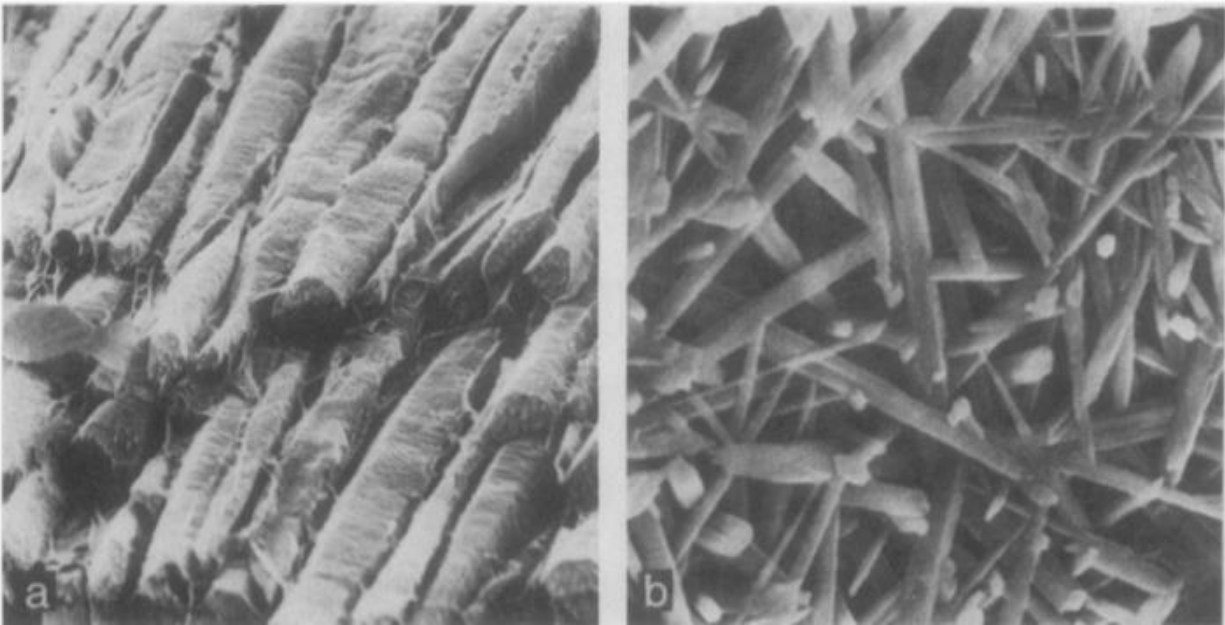
Figure 1.1. Matrix-mediated biomineralization compared to biologically-induced.
Comparison of crystals resulting from matrix-mediated biomineralization in a California mussel (**a**) and biologically induced biomineralization in the algae *Galaxaura obtusata* (**b**). Images taken from [3].

Using matrix-mediated biomineralization, organisms can create intricate mineral structures with order across many length scales. An interesting example of such materials is the shell of many marine mollusks. These shells are created and maintained by a structure called the mantel that

makes and secretes an organic matrix. This matrix controls not only the morphology of the calcium carbonate that forms, but also its polymorph. In the mollusk *Atrina rigida*, the shell has two zones. One, called nacre, consists of tablets of the polymorph aragonite (**Figure 1.2a,b**) and is the inner layer of the shell, responsible for the opalescent appearance. The second, the prismatic layer, is made of pillars of calcite oriented with the long axis of the crystals perpendicular to the shell surface (**Figure 1.2a,c**).[4]
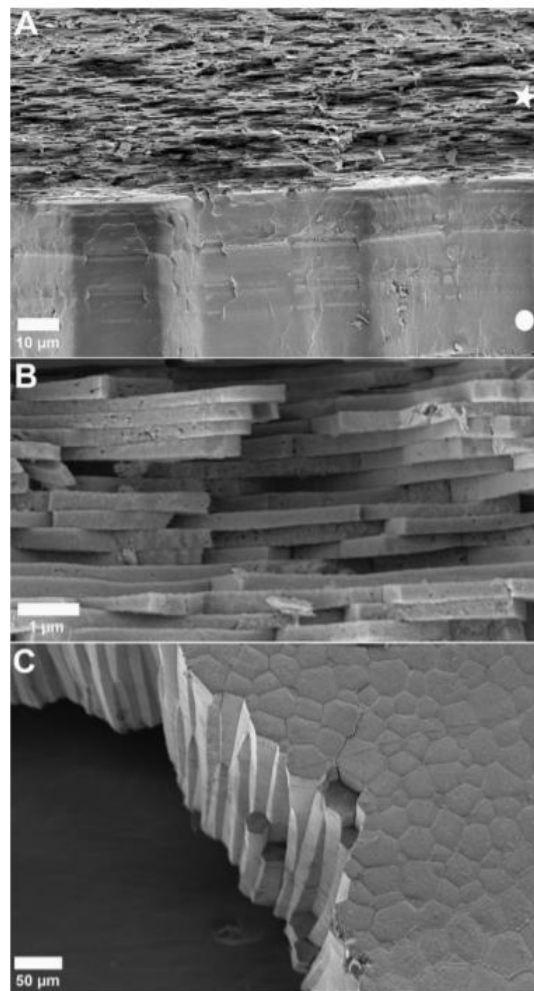
Figure 1.2. a. Scanning electron microscope image of *Atrina rigida* shell in cross-section. Nacreous layer marked by a star and the prismatic layer marked by a circle. **b.** Increased magnification of the nacre layer. **c.** Calcite pillars in the prismatic layer, shown in side view and lower magnification in (**a**). Images from [4].

In both the prismatic and nacre layers, calcium carbonate crystals are surrounded by a layer of organic material.[4-5] In the prismatic layer, which is closest to the exposed surface of the shell, this composite microstructure strengthens the shell against compressive forces from the environment. Mechanistically, the calcite crystals of the prismatic layer provide strength and stiffness, and the organic layers toughen the structure by transferring force to neighboring crystals, decreasing the load on a single crystal. The aragonite crystals in nacre, on the other hand, are wide in two dimensions, with their short dimension parallel to the long axis of crystallites in the prismatic layer. In nacre, the crystallites and the organic matrix between them prevent crack propagation. The lowest energy path for cracks is in the organic layer, so the width of the crystallites makes that path incredibly tortuous, thus drastically impeding crack propagation.

The shell of *Atrina rigida* is just one example of how biological organisms use matrix-mediated biomineralization to create highly organized structures that optimize mechanical and chemical properties. Another biomineral with highly optimized properties due to organic matrix-induced structural complexity is enamel.

1.3   ENAMEL

The hardest tissue in the human body, enamel begins to develop in the womb. At approximately 6 weeks, the epithelium above the mandible begins to thicken, creating a group of cells called the dental lamina. This lamina grows, forming the tooth bud, which grows and expands into a dome shape in the cap stage of tooth development. In this stage, the enamel organ forms from cells of the epithelial cap. Mesenchymal cells underneath the cap condense, forming the dental papilla and dental follicle. Together, these three components make up the tooth germ. In the

bell stage of tooth development, the tooth germ grows, as the cells of the enamel organ differentiate into inner and outer enamel epithelium (**Figure 1.3**).
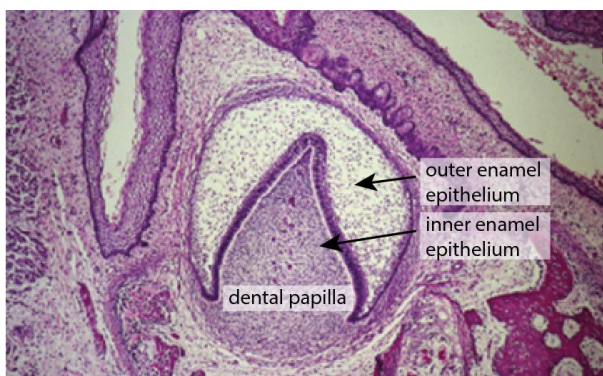
Figure 1.3. Bell stage of humane enamel development.[6]

The cells of the inner epithelium elongate and become ameloblasts. The adjacent cells in the dental papilla become odontoblasts, which move toward the center of the papilla, leaving dentin behind. The ameloblasts move outward from the inner epithelium, laying down ribbons of amorphous calcium phosphate (ACP).[7] These ribbons crystallize, and thicken until they impinge upon each other, resulting in the final enamel structure.[8] After the tooth erupts into the oral cavity, the ameloblasts are lost, so no additional enamel can form.

Enamel itself is composed of mostly hydroxylapatite ($Ca_5(PO_4)_3(OH)$) (**Figure 1.4**) and often has trace amounts of other ions, such as magnesium, fluorine, chlorine, and carbonate.[9] The presence and identity of these (and other) impurity ions can have a drastic effect on the solubility of hydroxylapatite (OHAp) at low pH levels, which are especially relevant in the oral cavity. For example, magnesium can substitute for calcium in the OHAp lattice (up to ~0.3 atom%), but its higher charge density would destabilize the crystal structure, making it more soluble in acid.[9] Fluorine can replace hydroxyl groups in the OHAp lattice and its smaller size decreases lattice energy, making the material less soluble. Carbonate can substitute for either hydroxyl or

phosphate, resulting in increased solubility of the enamel, potentially due to lattice defects caused

by the size of carbonate.
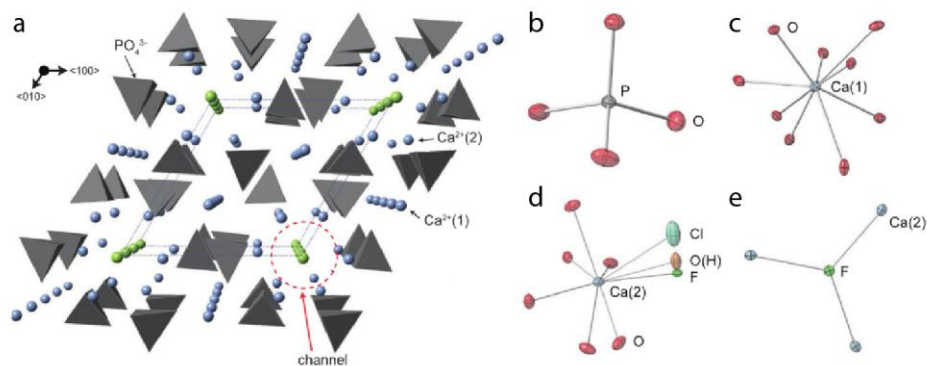
Figure 1.4. Crystal structure of apatite.
Apatite (**a**) is comprised of tetrahedral phosphate groups (**b**), Ca(1) coordinated by nine oxyanions
(**c**), Ca(2) coordinated by six oxyanions and a channel ion (**d**), and channel sites coordinated by
three Ca(2) (**e**). Adapted from [10].

Fully formed enamel has a complex microstructure, with features spanning many length

scales. A more detailed description of the hierarchical structure of enamel will be discussed in

Chapter 2; briefly, human enamel consists of bundles of thousands of hydroxylapatite crystallites,

forming a 3D structure visible using scanning electron microscopy (SEM) (**Figure 1.5**). The

complex chemistry and structure of enamel play a key role in how it is affected by exposure to

acid in the oral cavity.

2.5 nm
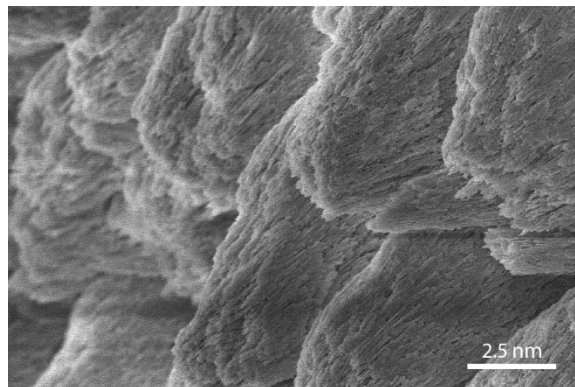
Figure 1.5. SEM image of etched enamel showing several bundles or "rods" composed of OHAp crystallites.

Dental caries, commonly called tooth decay, is the most prevalent infectious disease in the world, affecting 60-90% of children worldwide and nearly all adults.[11] Caries form when the plaque biofilm present in the oral cavity reacts with ingested sugar and starches to form an acid that dissolves the underlying enamel. This demineralization is counteracted by remineralization through contact with saliva, which is supersaturated with respect to hydroxylapatite. Previous research has suggested that the most soluble part of enamel, the periphery of the crystallites, dissolves first during acid attack.[9] The first visible sign of a caries lesion, a white spot enamel lesion (WSEL), is associated with a white, chalky, spot on the tooth (**Figure 1.6b**). Polarized light shows that the WSEL consists of a nearly fully mineralized surface zone (SZ) (**Figure 1.6c,d**) covering the body of the lesion, which has a much lower mineral content. As demineralization progresses, pores that form in the body of the lesion grow until the tissue is destroyed (cavitation), at which point the surface zone disappears.[9]
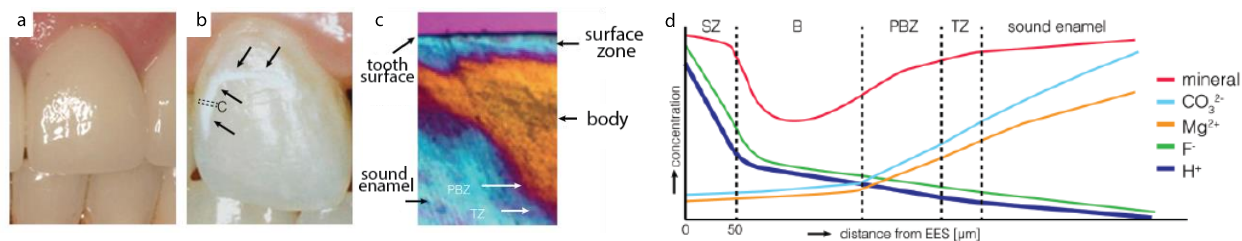
Figure 1.6. White spot enamel lesions.
a. Healthy enamel.[12] **b.** White spot enamel lesion.[12] **c.** Polarized light image of cross section of white spot enamel lesion[13] **d.** Concentration profile through the lesion.[9]

Though caries affects nearly all humans over the course of their lifetime, early studies found that all populations were not equally susceptible. For example, people whose water supplies that were high in fluorine were markedly less likely to get caries as compared to their counterparts.[14] This discovery has led to community water fluoridation (CWF) projects and use of fluoridated toothpastes, resulting in a 25% decrease in cavities in adults and children.[15] Additional studies suggest that other trace elements found in food or drinking water, such as Mo, Se, Sr, and Zr, may also be related to lower caries prevalence.[16-17] Other elements such as Mg, Cu, and Pb, have been found to have a positive correlation with high prevalence of caries.[18] Though evidence suggests that these trace elements may affect the dissolution of enamel, the exact mechanism by which they are incorporated into fully formed enamel is still unknown. Further insight into this process may lead to more efficient treatment methods and a significant decrease in the prevalence of caries. In order to study the effect of trace elements and their uptake into enamel, in is necessary to understand the chemistry and structure of enamel on the length scale of individual crystallites, a significant challenge using conventional microscopy techniques. As such, we turned to atom probe tomography, which has the spatial and chemical resolution necessary to perform these studies.

1.4 ATOM PROBE TOMOGRAPHY

Atom probe tomography (APT) has long been used to characterize metals. With sub-nanometer spatial resolution and parts per million chemical sensitivity, it is a useful tool for studying the structure and chemistry of materials on the nanoscale.[19] In APT, a needle-shaped sample is placed in a very large electric field (15-65 V/nm), resulting in the field ionization of atoms, or clusters of atoms, from the tip of the specimen (**Figure 1.7**).[19-20]
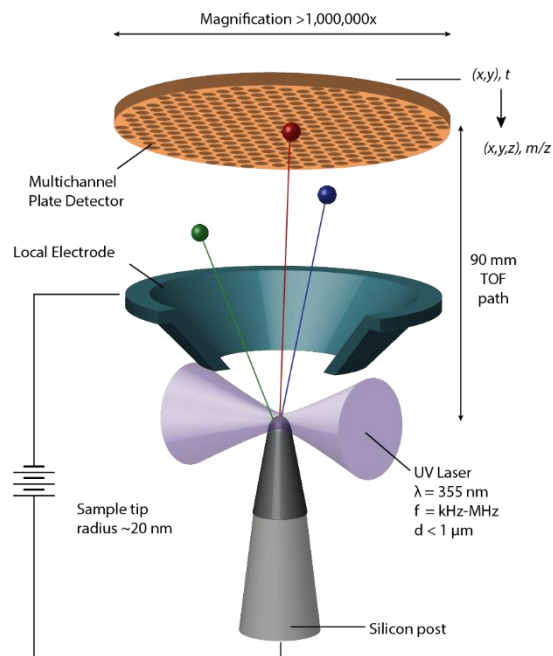
Figure 1.7. Schematic drawing of an atom probe tomograph (adapted from [10])

These ions are then accelerated through a hollow conical local electrode, and experience largely field free drift between the electrode and the detector. Ions can be identified based on their time of flight and, using identity and positional information, a 3D image of the tip can be reconstructed. The field evaporation process in metals is reasonably well understood.[19-20] Briefly, positively charged ions are sublimed or evaporated off the sample tip as a result of the high electric field

polarizing atoms, giving them a higher potential energy away from the tip (as compared to the case where no electric field is present).[20] Field evaporation may occur in two steps: (1) escape from the surface of the sample tip and (2) post-field ionization to higher charge state.[21] The escape step is generally described as thermally overcoming an energy barrier (Q_n):

$$k_n(F, T) = A \exp\left(-\frac{Q_n(F)}{k_B T}\right) \qquad \textbf{(Eq. 1.1)}$$

where k_n, the rate constant, is a function of the field inside the atom probe (F) and temperature (T), A is a constant related to the vibration frequency of atoms on the surface of the tip, and k_B is the Boltzmann constant.[21] The activation barrier depends on the escape charge state of the ions.[22] Multiplying both sides of **Eq. 1.1** by the number of atoms on the specimen surface that are likely to field evaporate and hit the detector (n_{hr}) gives the emission rate (R[ions (or atoms)/s]) [21]:

$$R = n_{hr} k_n(F, T) = n_{hr} A \exp\left(-Q_n(F)/k_B T\right) \qquad \textbf{(Eq. 1.2)}$$

The two main proposed ion escape mechanisms are charge exchange, which suggests that ionization occurs gradually as the ion escapes across the energy hump, and image hump, which assumes that the ion is fully ionized before it leaves the sample tip.[23] Generally, the charge exchange method is more widely accepted. According to this method, most metal ions escape with a 1+ or 2+ charge, but can achieve a higher charge state in strong electric fields as a result of post field ionization.[21] The advent of UV laser-assisted field evaporation has made it possible to characterize insulating materials, greatly increasing the scope of APT. This has allowed analysis of an increasing variety of materials, from meteoritic nanodiamonds to biogenic minerals.[24-30]

2. CHEMICAL GRADIENTS IN HUMAN ENAMEL CRYSTALLITES

The work from this chapter, including figures, has been reproduced, with or without modifications, from our publication: K. A. DeRocher, P. J. M. Smeets, B. H. Goodge, M. J. Zachman, P. V. Balachandran, L. Stegbauer, M. J. Cohen, L. M. Gordon, J. M. Rondinelli, L. F. Kourkoutis, D. Joester, "Chemical Gradients in Human Enamel Crystallites, *accepted,* Nature 2020.

Co-first author Paul J.M. Smeets performed the STEM experiments with assistance from collaborators at Cornell University (Berit H. Goodge, Michael J. Zachman, and Lena F. Kourkoutis). The XAS results were obtained by Lyle M. Gordon and Michael J. Cohen. I performed the APT experiments and analysis, and created the FEM model based on the DFT calculations executed by Prasanna V. Balachandran. Linus Stegbauer synthesized and characterized the Mg-OHAp single crystals.

2.1 INTRODUCTION

Dental enamel is a principal component of human teeth, providing protection to the underlying dentin. It has evolved to bear large masticatory forces, resist mechanical fatigue, and withstand wear over decades of use. Functional impairment or loss of enamel, for instance as a consequence of developmental defects or tooth decay (caries), has a dramatic impact on health and quality of life, and causes significant costs to society.[31-32] While the last decade has seen great progress in our understanding of enamel formation (amelogenesis) and the functional properties of mature enamel, attempts to repair enamel lesions or synthesize enamel in vitro have had somewhat limited success.[33-36] Fundamentally, there are no models that accurately describe phase transformations during enamel formation or the de-mineralization-remineralization cycles that

result in caries lesions. An integrated model that accounts for enamel mechanical properties is similarly lacking. This is due, at least in part, to the highly hierarchical structure of enamel and the additional complexities that arise from chemical gradients that we are only beginning to understand (**Figure 2.1**).

Enamel covers the entire crown of human teeth (**Figure 2.1a**), and can reach a thickness of several millimeters (**Figure 2.1b**). A characteristic microstructural element is the enamel rod, (**Figure 2.1c**) which is comprised of thousands of lath-like crystallites that are aligned with their crystallographic *c*-direction approximately parallel to the long axis of the rod (**Figure 2.1d**). Crystallites sectioned normal to their long axis appear as oblong, convex polygons with an edge length of 20-50 nm in the short and 70-170 nm in the long direction (**Figure 2.1e,f**). The extraordinary mechanical performance of enamel, including its surprising fracture toughness, is thought to emerge from a combination of factors at different levels of hierarchy.[37]

Enamel owes its hardness (~5 GPa) to its high mineral content (~96 wt%).[38] Nominally comprised of hydroxylapatite (OHAp; $Ca_5(PO_4)_3(OH)$), minor constituents include magnesium (0.2 – 0.6 wt%), sodium (0.2 – 0.9 wt%), carbonate (2.7 – 5 wt%), and fluoride (~0.01 wt%).[9,39] These ions can substitute on the apatite lattice and are known to modulate its solubility in water. Hence, they may have an important impact not only on the formation of enamel crystallites, but also on their dissolution. Recently, it was discovered in rodent incisor enamel that most Mg is not incorporated into crystallites, but confined between them as Mg-substituted amorphous calcium phosphate (Mg-ACP).[25] The high solubility of Mg-ACP is responsible for the highly anisotropic etching behavior of rodent enamel. APT of human enamel confirmed segregation of Mg to the

grain boundaries[29]; however, the presence of Mg-ACP in human enamel has not yet been demonstrated.
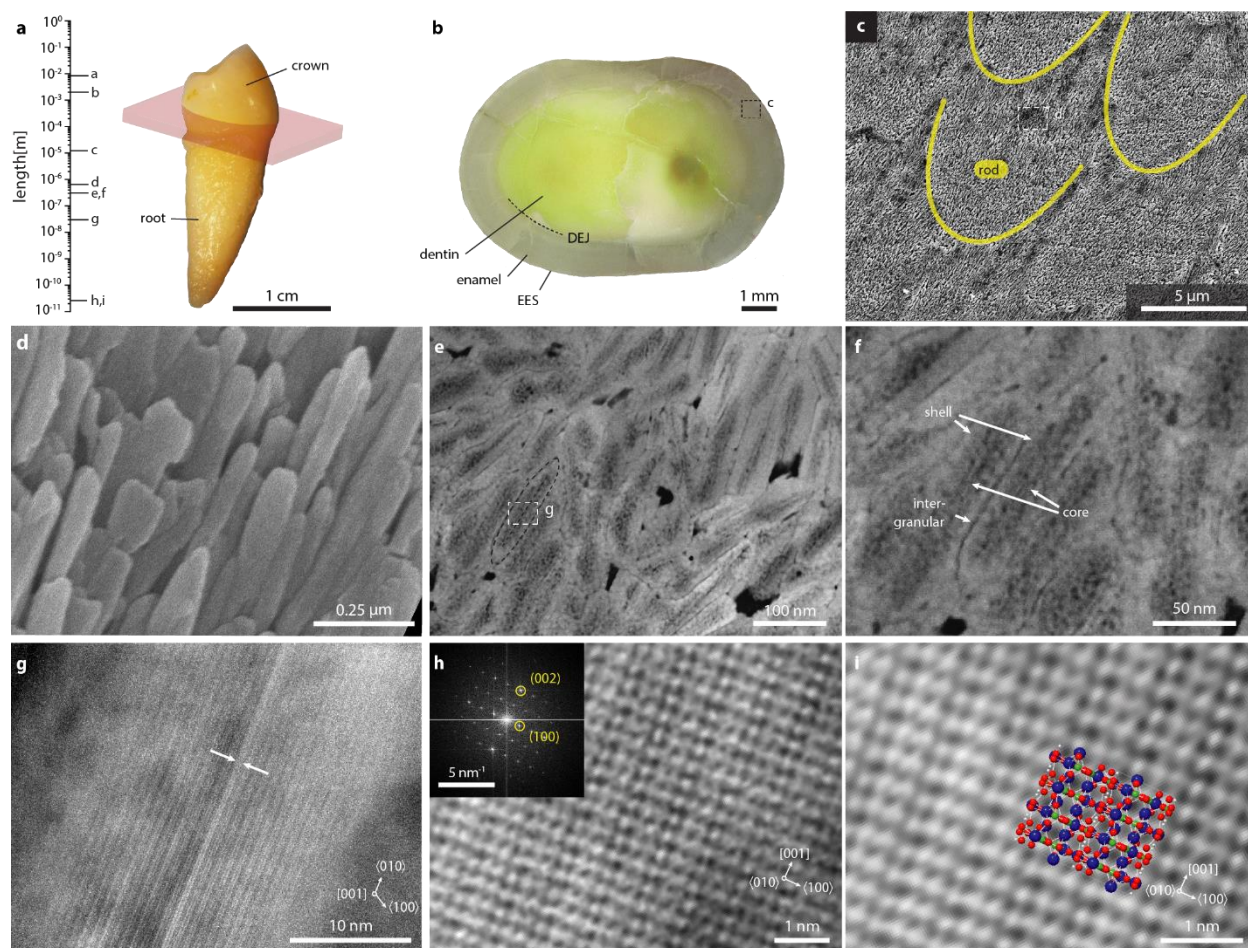
Figure 2.1. The hierarchical architecture of human enamel.
a. Length scales of enamel in a human premolar. **b.** Section parallel to the mid-coronal cervical plane (indicated in pink in **a**). **c.** SEM image of keyhole-shaped cross-sections of enamel rods in lactic acid-etched outer enamel. **d.** SEM image of OHAp crystallites. **e-g.** STEM-ADF images of enamel crystallites in cross section, oriented approximately parallel to the [001] zone axis. The CDL (arrows) appears bright in ADF. **h.** Cryo-STEM-ADF lattice image of a crystallite oriented parallel to the [010] zone axis (inset: FFT). **i.** Higher magnification of region shown in (**h**) with rendering of 2×2×2 OHAp supercell (Ca, blue; O, red; P, green; H, white). Data presented in panels **b, e-i** were recorded by Paul Smeets

Interestingly, there is evidence that the center of the crystallites in human enamel may be more soluble than the surrounding region.[40] This could be the consequence of structural defects that localize to the center of the crystallite. It has previously been suggested that the central dark line (CDL), a somewhat enigmatic feature observed in enamel crystallites by TEM under certain conditions (**Figure 2.1g**), is a marker of such defects.[41] Alternatively, the composition of the crystallites may not be constant across their diameter. Grading of individual crystallites is almost certainly established during amelogenesis. Improved understanding of the defect distribution would therefore provide insight into the environmental conditions during enamel crystallite growth and potentially elucidate the crystallization pathway itself. Furthermore, this information is required to build mechanistic models of enamel dissolution and reprecipitation during the formation of caries lesion or their repair. Finally, it is possible that mechanical properties of enamel crystallites are impacted.

We therefore set out to test the hypothesis that individual crystallites in human enamel are graded in composition. Herein, we examine their structure and composition using scanning transmission electron microscopy at cryogenic temperature (cryoSTEM) and associated quantitative imaging techniques, X-ray absorption spectroscopy (XAS), and atom probe tomography (APT). We find that, two additional levels of hierarchy are required to describe chemical gradients in enamel crystallites and, using density functional theory (DFT) calculations and finite element modeling, explore the implications of these gradients for chemical and mechanical properties, and the crystallization pathway during amelogenesis.

2.2   RESULTS AND DISCUSSION

2.2.1   ELECTRON MICROSCOPY

We focused our analysis on crystallites in the outer enamel of human premolars sectioned parallel to the mid-coronal cervical plane (**Figure 2.1b**). Premolars were selected as they are often extracted while still healthy for orthodontic reasons. Lamellae were prepared from ground and polished enamel sections using standard focused-ion-beam (FIB) methods. Advanced electron optical methods offer seamless integration of structural and chemical information at length scales from hundreds of microns to the atomic scale.[42-44] The obtainable resolution of any experiment, however, is limited by the radiation sensitivity of the material in question. For apatites in general, and for enamel crystallites in particular, the total dose should not surpass 10,000 $e^{-}/Å^{2}$.[45-46] This dose is at least three orders of magnitude lower than what is typically used for atomic-resolution elemental mapping of more robust materials.[47] For analysis of thin sections at atomic resolution, however, electron radiation artifacts such as radiolysis and mass loss, among others, are strongly reduced by operating at cryogenic conditions.[48] In addition, surface contamination due to carbon migration is minimized at these temperatures.[49] To help mitigate these effects, we therefore performed aberration-corrected scanning transmission electron microscopy at cryogenic temperature (cryo-STEM), using low dose techniques (**Table 2.1**).

Table 2.1. Typical Imaging Conditions for STEM Experiments

Parameter	Instrument					
	JEM-2100F	GrandARM 300F		Titan Themis		
Acceleration Voltage [kV]	200	300		300		
Aberration-correction	n/a	n/a		Cs		
Imaging Mode	STEM	STEM		STEM		
Nominal Sample Temperature* [˚C]	R.T.	R.T.		< -170˚C		
Convergence semi-angle [mrad]	19.2	29		21.4		
Image contrast	ADF	ADF†	HAADF †	ADF		
Collection semi-angle [mrad]	83.3−183.3	55-106	106-180	39-190		
Probe current [pA]	80	20.8	20.8	4.0	4.0	8.5
Frame edge length [pixels]	2048	2048	2048	2048	4096	1024
Pixel edge length [Å]	3.90	0.64	0.64	0.19	0.09	0.35
Dwell time [µs]	25	2	2	1	1	2
Total dose per exposure [e⁻/Å²]	822	635	635	727	2909	873

* The nominal sample temperature was read from a thermocouple near the tip of the sample rod.
† MAADF and HAADF images collected simultaneously.

A Gatan 636 dual tilt liquid nitrogen side entry holder was used for cryo-STEM in the Titan Themis. The cryo holder was baked at 100 °C while pumping on the dewar vacuum for 12 hours before use to ensure good thermal insulation of the cryogen during the experiment. Samples were inserted into the microscope at room temperature and the holder was subsequently cooled with liquid nitrogen for at least 2h prior to imaging to allow the temperature to stabilize and thermal drift to subside. Even when fully stabilized, cryo-STEM at the atomic scale often requires fast acquisition to minimize the impact of stage drift. Low-dose imaging further reduces the signal-to-noise ratio of single-frame images. Unless otherwise specified, we therefore used a post-processing approach optimized for these conditions.[44] Specifically, a series of images of enamel crystallites were collected rapidly (2-4 s/frame), with a total dose of 410-873 e⁻/Å² per exposure (e.g. **Figure 2.2a**). During post-processing, a number of successive frames were rigidly registered by cross-correlation, and averaged to minimize noise and stage drift (e.g. **Figure 2.2b**).[44] This was

followed by Fourier-filtering using a Butterworth low pass filter.[50] Specifically, an FFT from a region of the cross-correlated image was computed (e.g. **Figure 2.2d**), and multiplied by a 3rd order Butterworth filter with a cutoff frequency of half the sampling frequency (e.g. **Figure 2.2e**). Subsequently, the inverse of this filtered FFT was then computed and cropped to the same region of interest as the unfiltered image (**Figure 2.2**), to obtain **Figure 2.1h,i**. In some cases, cross-correlation was not necessary, and the image was acquired with a single frame with scan parameters chosen to result in a comparable total dose (**Figure 2.3a**).
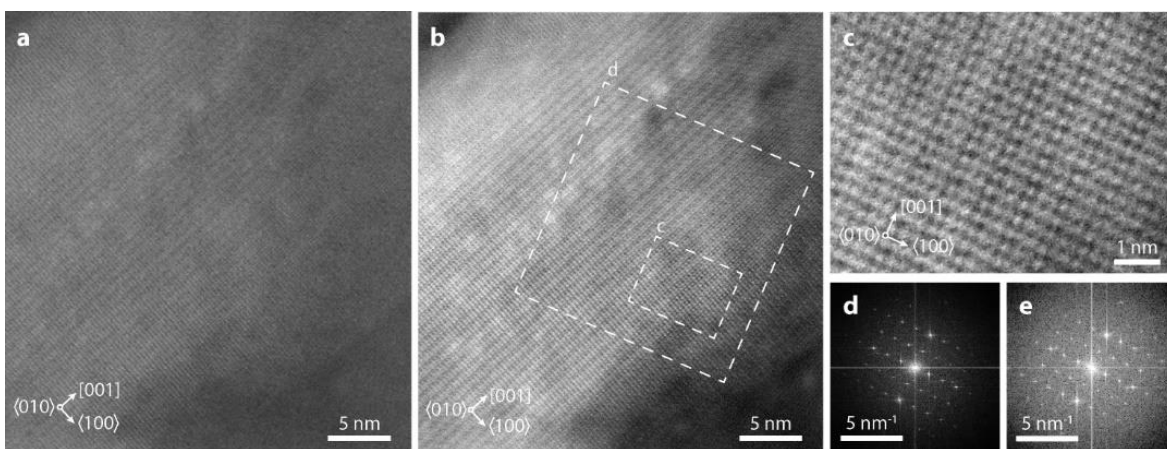
Figure 2.2. Cross-correlation of rapidly acquired high resolution cryo-STEM-ADF images. **a.** Single frame displaying part of a crystallite oriented to the [010] zone axis. **b.** Cross-correlated and averaged image generated from 9 frames. **c**. Close-up of area indicated in (**b**) without any additional filtering **d.** FFT computed for the area indicated in (**b**) (width and height are an integer power of 2). **e.** FFT of (**d**) multiplied with a Butterworth image of order 3 and a cutoff of half the sampling frequency. The image shown in **Figure 2.1h&i** are based on the inverse FFT of (**e**). Images recorded by Paul Smeets.

Individual crystallites packed in an enamel rod are readily apparent in images recorded with annular dark field (ADF) contrast (**Figure 2.1e**). Crystallites are clearly separated by narrow regions that appear darker than the crystallite (**Figure 2.1f**), consistent with expectations for a Mg-rich amorphous intergranular phase, and appear to have a shell that is brighter than the core (**Figure**

2.1e). This core-shell architecture of crystallites was observed over large areas in premolars from different individuals, indicating that it is a widespread phenomenon.

In atomic scale cryoSTEM-ADF images, the crystallite core appears as a patchwork of lighter and darker areas (**Figure 2.3a**). There is a continuous lattice across the entire crystallite, effectively ruling out that the difference in intensity is due to the presence of another phase. Taken together, these factors suggest that there is a compositional gradient across the crystallite. Specifically, the shell appears biased toward heavier elements (Ca), and the core appears biased towards lighter elements (Mg, Na) and is more prone to beam damage.[41]
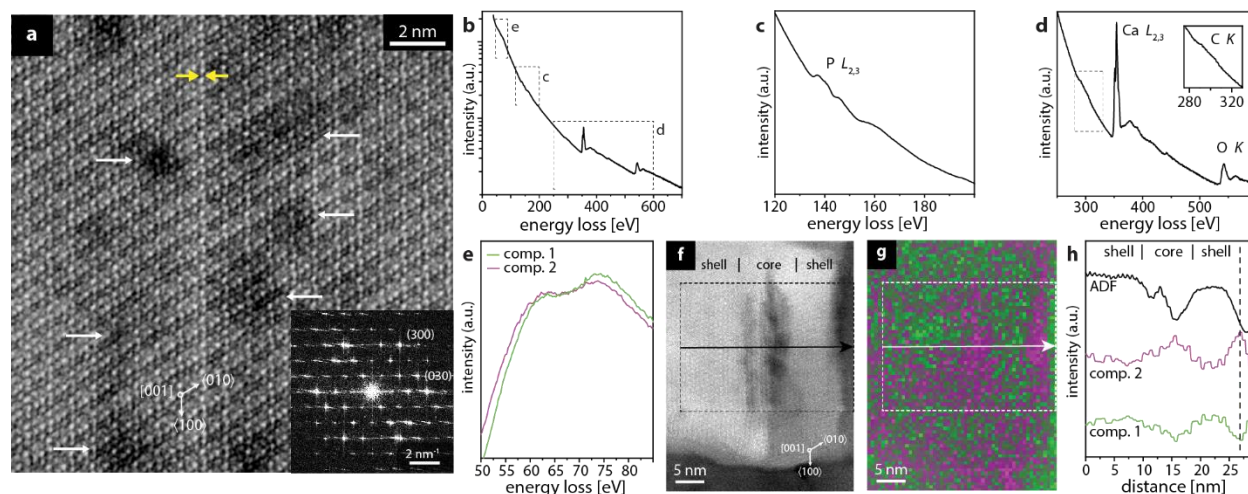
Figure 2.3. Atomic scale structure and composition of human enamel crystallites.
a. Cs-corrected cryo-STEM ADF lattice image of the core of a single enamel crystallite oriented to the [001] zone axis, close to the CDL (yellow arrows). Inset: FFT. **b-d**. Cryo-STEM EEL spectra obtained from a region containing several enamel crystallites, with higher magnification images of the P-$L_{2,3}$ edge (**c**) and the Ca-$L_{2,3}$, O-K, and C-K edges (**d**). **e**. MCR components contributing to feature near the Mg-$L_{2,3}$ edge. **f**. Cryo-STEM ADF image of an enamel crystallite. **g**. Spatial intensity map of MCR components 1 (green) and 2 (magenta) in (**f**). **h**. Average intensity profile for the region of interest indicated in (**f**) and (**g**), in the direction of the arrow. Data presented in this figure were recorded by Paul Smeets.

STEM in conjunction with energy-dispersive X-ray spectroscopy (STEM-EDS) and electron energy loss spectroscopy (STEM-EELS) enables compositional analysis at a length scales

down to the atomic. However, quantification – especially of light elements – remains challenging.[51] While STEM-EDS reported ~0.4 at% Mg, 0.7 at% Na, and 0.6 at% F in crystallites (**Table 2.2**), elemental maps were largely featureless (not shown).

Table 2.2. Composition of fluoridated human enamel by STEM-EDS

Element	all detected elements		elements expected in enamel	
	X [at%]	σ_X [at%] (N = 3)	X [at%]	σ_X [at%] (N = 3)
C	13.80	2.07	17.57	2.27
O	45.74	0.60	51.96	0.78
F	0.53	0.11	0.47	0.04
Na	0.68	0.10	0.68	0.05
Mg	0.35	0.08	0.37	0.08
P	14.4	0.61	11.68	0.70
Cl	0.31	0.10	0.28	0.01
Ca	21.03	0.80	16.99	0.88
Cu*	2.99	0.13		
Si†	0.11	0.05		
Ga‡	0.06	0.04		
Total	100		100	

*Likely from TEM grid; †unclear origin; ‡contamination from FIB processing.

STEM-EEL spectra were collected at cryogenic temperature using a low electron dose. A direct electron detector with exceptionally high quantum efficiency allowed simultaneous acquisition of all relevant inner shell ionization (core loss) edges at high resolution and low background levels while minimizing beam damage.[52]

In the core-loss region of cryoSTEM-EEL spectra, the calcium $L_{2,3}$ and oxygen K-edges are prominent (**Figure 2.3d**) and the phosphorus $L_{2,3}$ edge is clearly recognizable at increased magnification (**Figure 2.3c**), consistent with expectations.[9] The carbon K-edge is rather weak (**Figure 2.3d inset**), consistent with a composition containing small amounts of primarily inorganic carbon. Na and F were not detected. The low abundance of Mg necessitated a focus on the lower-loss region of the spectrum, where signals are much stronger for a given primary beam

dose. While a small signal is clearly visible near the expected onset of the Mg $L_{2,3}$ edge at 51 eV (**Figure 2.3e**), several other components also have edges in this region of the spectrum.

To understand variations in this low-loss signal across the sample, we used multivariate curve resolution (MCR), a chemometric approach that has recently been extended to spectroscopic methods,[53] to decompose the spectroscopic image matrix into statistically significant spectral components (**Figure 2.3e**). Spatial intensity maps reveal that component 1 is predominant in the shell of the crystallite (**Figure 2.3g,h**). Component 2, on the other hand, predominates in the intergranular Mg-ACP and the crystallite core (**Figure 2.3g,h**). Spectroscopic differences suggest distinct local bonding environments which appear to be correlated with the structural regions identified by TEM and STEM imaging, and support the notion that there are subtle compositional gradients across the crystallite and within the core. As the susceptibility of enamel to beam damage limited our ability to directly detect such gradients using STEM-based methods, we turned to x-ray absorption spectroscopy (XAS) and atom probe tomography (APT) for further characterization.

2.2.2 X-RAY ABSORPTION SPECTROSCOPY

X-ray absorption near edge structure (XANES) spectra recorded at the Mg *K*-edge provides information on the crystallographic environment of Mg atoms. The position and intensity of transitions in Mg K-edge XANES spectra are sensitive to the coordination number, geometry, bond length, and order at intermediate range. Many Mg-containing minerals can be identified by their spectral fingerprints.[54] Spectra of rodent enamel lack the pre-A, D, and E features that are characteristic of crystalline dolomite, huntite, and whitlockite (**Figure 2.4a**).[25] In contrast, the Mg-rich intergranular phase in rodent incisors shows a striking similarity to spectra of synthetic

Mg-substituted amorphous calcium phosphate (Mg-ACP). The dominant feature in Mg-ACP spectra is the transition associated with the first coordination sphere (feature B), with few or no features that depend on order beyond the first shell. The lower edge energy is indicative of a lower coordination number and shorter Mg-O bond distance. Spectra of human enamel are similar to those of rodent enamel or synthetic Mg-ACP yet display more pronounced A and B features (at ~1311 eV and 1313 eV respectively). As these features are associated with electronic transitions in the first coordination sphere and multiple scattering events from higher shells, this indicates that a fraction of the Mg in human enamel is present in a crystalline rather than an amorphous environment. In combination with the observations from STEM-ADF and STEM-EELS, this supports the notion that at least some of the Mg in human enamel substitutes on Ca lattice positions, likely in the core of the crystallite.
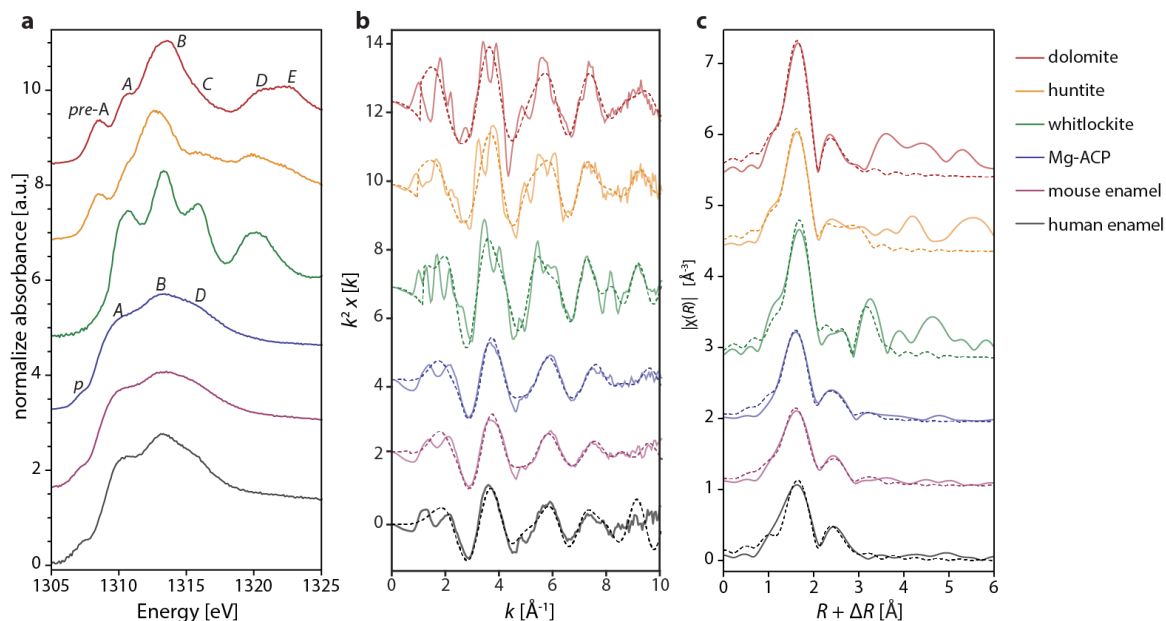
Figure 2.4. Comparison of Mg *K*-edge X-ray absorption spectra of dental enamel from different species and reference compounds.
Mg ACP, mouse enamel, and reference mineral spectra from [25]. Human enamel spectra from [55]. **a.** Mg *K*-edge XANES. **b.** Mg *K*-edge EXAFS (k^2-weighted). **c.** Mg *K*-edge EXAFS (real space). Data presented in this figure were collected and plotted by Lyle Gordon and Michael Cohen.

2.2.3 ATOM PROBE TOMOGRAPHY

Specimens for APT were prepared from outer enamel, approximately 10 µm below the buccal surface on mid-coronal cervical sections of human premolars. Some sections were fluoridated with 250 mM aqueous NaF at pH 8.4 for 24 hours before analysis. Samples were extracted from surfaces using focused ion beam (FIB) technique.[56] A total of 23 samples ('tips') were prepared for APT analysis. 18 of these represented native samples and 5 represented samples treated with NaF. During initial quality control, data sets with unsatisfactory voltage history (i.e. many large, sudden changes in the voltage) were excluded. Small data sets (<5-7 million hits) were also excluded, as it was unlikely the sample ran long enough that the reconstruction would contain whole crystallite cross sections. For this analysis, we looked at three APT data sets collected from

enamel after treatment with aqueous NaF (yield 60%, **Table 2.4**, **Figure 2.5a-c**), and two data sets

that were not treated (yield 11%, **Table 2.4**, **Figure 2.5d,e**).
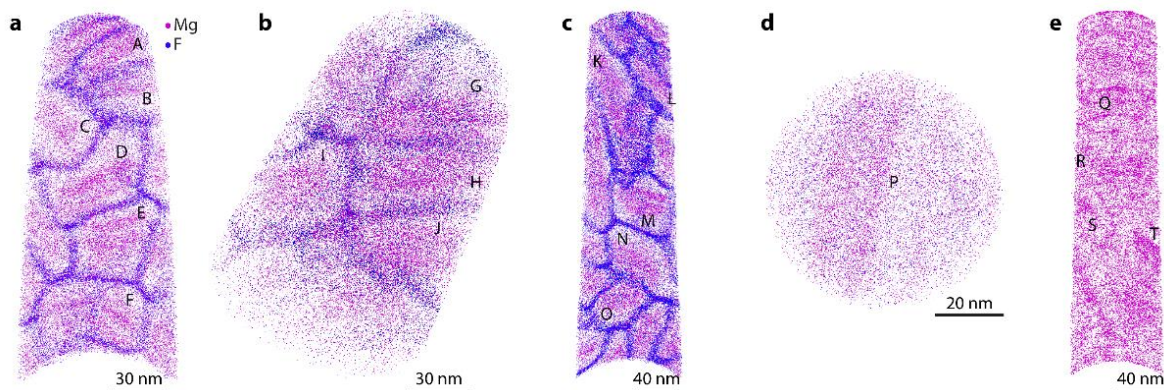
Figure 2.5. APT reconstructions of treated and untreated human enamel.
3D reconstruction of treated (**a-c**) and un-treated (**d,e**) human enamel oriented such that the view direction is approximately parallel to the long axis of the crystallites. For tips **a-d**, Mg ions ($m/z =$ 12, 12.5, 13 Da) and CaF ions ($m/z = 59$ Da) and rendered. There was no CaF present in the mass spectrum for tip **e**, so only Mg ions are rendered.

APT spectra of human enamel closely resemble those of rodent enamel (**Figure 2.6**, **Table 2.3**), with ions derived from OHAp as major features.[25,57] Minor constituents include Mg, Na, F, organic carbon, and inorganic carbon. In addition, trace amounts of Cl$^-$ (<0.1at%), Al (<0.004 at%), and implanted Ga (0.002-0.022 at%) were detected.
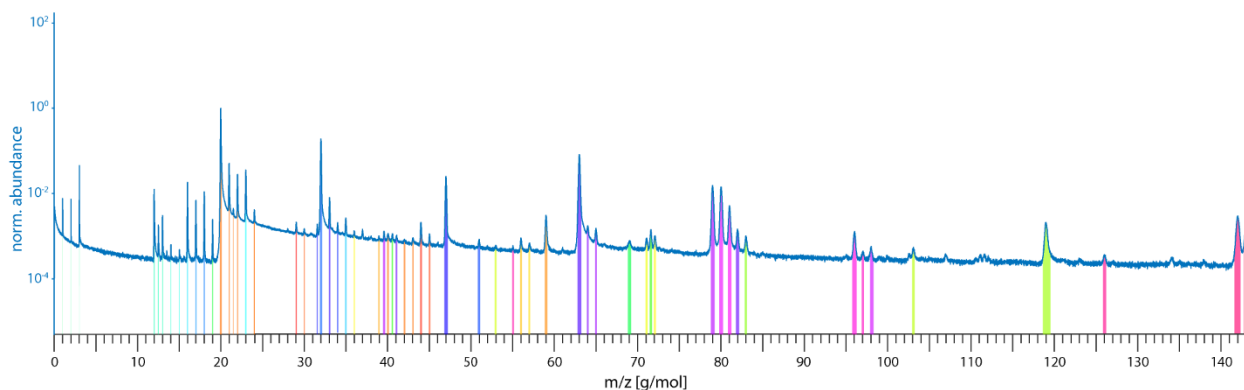
Figure 2.6. Representative ranged mass spectrum of fluoridated human enamel.

Table 2.3. Ions identified in representative APT spectrum of enamel.

Formula	Charge State	m/z (calc'd) [Da]	m/z (expt) [Da]	integration lower limit [Da]	integration upper limit [Da]	integral
^1H	+	1.01	1.01	1.00	1.02	108.01
$^1H_2$	+	2.01	2.02	2.00	2.02	118.99
$^1H_3$	+	3.02	3.02	3.00	3.03	597.32
^{24}Mg	2+	11.99	12.00	11.95	12.06	631.58
^{25}Mg	2+	12.49	12.50	12.45	12.55	98.19
^{26}Mg	2+	12.99	13.00	12.97	13.04	137.67
^{27}Al	2+	13.50	13.51	13.47	13.53	23.05
$^{12}C^1H_2$	+	14.00	14.01	13.98	14.03	27.68
$^{12}C^1H_3$	+	15.01	15.03	14.99	15.06	27.30
^{16}O	+	15.99	16.00	15.94	16.05	856.86
$^{16}O^1H$	+	17.00	17.01	16.95	17.07	365.15
$^{16}O^1H_2$	+	18.00	18.01	17.95	18.07	566.05
^{19}F	+	19.00	19.01	18.96	19.06	138.43
^{40}Ca	2+	19.98	19.99	19.88	20.11	65061.59
^{42}Ca	2+	20.98	21.00	20.94	21.06	3275.86
^{43}Ca	2+	21.48	21.50	21.46	21.53	283.41
^{44}Ca	2+	21.98	22.00	21.95	22.06	1922.22
^{23}Na	+	22.99	22.99	22.92	23.06	2590.61
^{48}Ca	2+	23.98	24.01	23.96	24.07	346.51
$^{12}C^{16}O$	+	28.00	28.03	27.96	28.07	148.70
$^{12}C^{16}O^1H$	+	29.00	29.03	28.97	29.10	221.07
$^{12}C^{16}O_3$	2+	29.99	30.02	29.95	30.06	145.48
$^{31}P^{16}O_2$	2+	31.50	31.56	31.50	31.63	203.38
$^{16}O_2$	+	31.99	32.00	31.87	32.14	17962.49
$^{31}P^{16}O^{19}F$	2+	32.98	33.03	32.95	33.12	825.72
$^1H_2^{16}O_2$	+	34.01	34.01	33.93	34.08	244.92
^{35}Cl	+	35.00	35.00	34.91	35.08	321.77
$^{40}Ca^{16}O_2$	2+	35.98	35.99	35.95	36.06	130.77
^{37}Cl	+	37.00	36.99	36.91	37.08	198.06
$^{40}Ca^{16}O_2$	2+	38.00	38.03	37.93	38.11	157.13
$^{40}Ca^{19}F_2$	2+	38.98	38.94	38.89	39.05	139.07
$^{31}P^{16}O_3$	2+	39.48	39.57	39.44	39.71	261.90
^{40}Ca	+	39.96	40.05	39.95	40.15	200.09
$^{31}P^{16}O_2^{19}F$	2+	40.98	41.10	40.97	41.17	180.17
^{42}Ca	+	41.96	42.02	41.93	42.12	141.60
^{43}Ca	+	42.96	43.06	42.96	43.12	126.97
$^{12}C^{16}O_2$	+	43.99	44.01	43.91	44.12	306.48
$^{12}C^{16}O_2^1H$	+	45.00	45.03	44.95	45.12	145.07
$^{31}P^{16}O$	+	48.97	47.00	46.82	47.23	3492.76
$^{16}O_2^{19}F$	+	50.99	51.01	50.83	51.11	182.28
$^{20}Ca^{31}P^{16}O^{19}F$	2+	52.96	52.98	52.85	53.07	118.59
$^{31}P_2^{16}O_3$	2+	54.97	55.05	54.95	55.15	96.93
$^{40}Ca^{16}O$	+	55.96	56.00	55.90	56.12	156.21
$^{40}Ca^{16}O^1H$	+	56.97	57.06	56.91	57.11	117.92
$^{40}Ca^{19}F$	+	58.96	59.00	58.86	59.18	581.11
$^{31}P^{16}O_2$	+	62.96	63.00	62.79	63.24	14432.94
$^{31}P^{16}O_2^1H$	+	63.97	64.02	63.91	64.11	292.00
$^{31}P^{16}O_2^1H_2$	+	64.98	65.00	64.90	65.10	248.61
^{69}Ga	+	68.93	69.03	68.83	69.23	265.84
$^{40}Ca^{31}P$	+	70.94	71.09	70.95	71.20	181.78
$^{40}Ca_2^{31}P^{16}O_2$	2+	71.44	71.60	71.44	71.73	295.03
$^{40}Ca^{16}O_2$	+	71.95	72.11	71.96	72.20	205.27
$^{31}P^{16}O_3$	+	78.96	79.00	78.78	79.24	3321.49
$^{31}P^{16}O_3^1H$	+	79.97	80.03	79.78	80.24	3243.06
$^{31}P^{16}O_3^1H_2$	+	80.97	81.03	80.83	81.25	1182.78

$^{31}P^{16}O_2^{19}F$	+	81.96	81.99	81.80	82.18	374.21
$^{40}Ca^{31}P_2^{16}O_4$	2+	82.94	82.98	82.86	83.11	199.15
$^{31}P^{16}O_4^{1}H$	+	95.96	96.04	95.74	96.29	402.34
$^{31}P_2^{16}O^{19}F$	+	96.94	97.05	96.89	97.16	101.10
$^{31}P^{16}O_3^{19}F$	+	97.96	98.03	97.89	98.30	167.81
$^{40}Ca^{31}P^{16}O_2$	+	102.93	103.09	102.94	103.24	134.20
$^{40}Ca^{31}P^{16}O_3$	+	118.92	118.97	118.62	119.54	879.29
$^{31}P_2^{16}O_4$	+	125.93	126.00	125.84	126.23	120.21
$^{31}P_2^{16}O_5$	+	141.92	142.02	141.60	142.35	1169.66
$^{31}P_2^{16}O_5^{1}H$	+	142.93	143.06	142.75	143.36	650.81
$^{31}P_3^{16}O_4^{1}H$	+	157.91	157.99	157.65	158.38	328.09
$^{31}P_3^{16}O_4^{1}H_2$	+	158.92	158.99	158.76	159.30	196.50
$^{40}Ca_2^{16}O_5$	+	159.90	160.06	159.79	160.34	208.25
$^{40}Ca_2^{16}O_5^{1}H$	+	160.91	161.02	160.74	161.23	138.63
$^{40}Ca_2^{31}P_3^{16}O_2$	+	204.84	205.17	204.15	206.13	430.09

Table 2.4. Comparison of ion fraction in NaF-treated and untreated samples. X_i^T indicates the fraction of all ions for a given ionic species in the i-th treated sample, X_j^U indicates the fraction in the j-th untreated sample.

species	NaF treated			untreated		$\bar{X}^T$	$\bar{X}^U$	$\bar{X}^T - \bar{X}^U$	$p*$
	X_1^T	X_2^T	X_3^T	X_1^U	X_2^U				
Al	4.76E-05	7.42E-05	5.64E-05	0.00E+0	0.00E+0	5.94E-05	0.00E+0	5.94E-05	0.01[†]
Cl	1.58E-03	1.57E-03	1.26E-03	2.25E-03	2.36E-03	1.47E-03	2.31E-03	-8.35E-04	0.01[†]
H_2	8.90E-04	1.33E-03	1.11E-03	2.31E-04	8.85E-05	1.11E-03	1.60E-04	9.50E-04	0.01[†]
$PO_2F^§$	1.70E-03	1.51E-03	1.16E-03	9.67E-05	4.52E-04	1.46E-03	2.74E-04	1.18E-03	0.02[†]
CH_2	1.03E-04	1.67E-04	1.82E-04	3.80E-06	0.00E+0	1.51E-04	1.90E-06	1.49E-04	0.02[†]
CH_3	7.86E-05	8.39E-05	7.98E-05	3.60E-05	0.00E+0	8.08E-05	1.80E-05	6.28E-05	0.02[†]
P_2O_4	2.14E-04	2.28E-04	1.16E-04	3.68E-04	3.64E-04	1.86E-04	3.66E-04	-1.80E-04	0.03[†]
$CaF^§$	3.44E-03	1.65E-03	2.85E-03	0.00E+0	2.33E-04	2.65E-03	1.17E-04	2.53E-03	0.03[†]
CaP_2O_4	6.89E-04	6.05E-04	3.38E-04	0.00E+0	9.11E-05	5.44E-04	4.56E-05	4.99E-04	0.04[†]
H_3	4.75E-03	9.34E-03	6.96E-03	1.90E-03	1.49E-03	7.02E-03	1.70E-03	5.32E-03	0.05[‡]
$Na^§$	1.85E-02	1.40E-02	1.73E-02	7.52E-03	1.18E-02	1.66E-02	9.67E-03	6.92E-03	0.06[‡]
PO_2H_2	7.49E-04	1.04E-03	5.51E-04	5.42E-05	4.00E-04	7.78E-04	2.27E-04	5.51E-04	0.09[‡]
O_2F	2.87E-04	3.20E-04	1.94E-04	3.63E-04	4.83E-04	2.67E-04	4.23E-04	-1.56E-04	0.10
H	7.59E-04	6.55E-04	5.91E-04	3.07E-04	5.36E-04	6.68E-04	4.21E-04	2.47E-04	0.10
Mg	6.42E-03	5.15E-03	6.69E-03	4.92E-03	4.42E-03	6.09E-03	4.67E-03	1.42E-03	0.11
$CaPO_2$	3.04E-04	3.49E-04	1.29E-04	5.66E-04	3.72E-04	2.61E-04	4.69E-04	-2.08E-04	0.16
CO_2H	3.74E-04	3.12E-04	1.90E-04	6.88E-05	2.29E-04	2.92E-04	1.49E-04	1.43E-04	0.22
O_2	1.44E-01	1.48E-01	1.53E-01	1.96E-01	1.51E-01	1.48E-01	1.73E-01	-2.48E-02	0.24
PO_2H	5.12E-04	6.06E-04	1.24E-04	4.99E-04	8.87E-04	4.14E-04	6.93E-04	-2.79E-04	0.33
CO_2	1.34E-03	1.40E-03	1.03E-03	4.51E-04	1.29E-03	1.26E-03	8.72E-04	3.87E-04	0.35
$CaPO_3$	5.27E-03	6.01E-03	5.08E-03	4.27E-03	5.41E-03	5.45E-03	4.84E-03	6.18E-04	0.35
PO_2	1.15E-01	1.24E-01	1.14E-01	9.55E-02	1.19E-01	1.18E-01	1.07E-01	1.04E-02	0.36
CaP	5.07E-04	4.21E-04	3.03E-04	2.74E-04	3.73E-04	4.10E-04	3.23E-04	8.71E-05	0.38
CaO	4.59E-04	4.11E-04	2.84E-04	1.25E-04	4.16E-04	3.85E-04	2.71E-04	1.14E-04	0.44
P	0.00E+0	4.79E-04	0.00E+0	0.00E+0	0.00E+0	1.60E-04	0.00E+0	1.60E-04	0.50
CO	1.05E-04	2.47E-04	7.16E-05	1.43E-05	1.49E-04	1.41E-04	8.15E-05	5.96E-05	0.54
Ca_2O_5	6.24E-04	8.22E-04	2.09E-04	2.70E-04	1.52E-03	5.52E-04	8.95E-04	-3.43E-04	0.56
PO_3	2.50E-02	2.27E-02	2.04E-02	2.35E-02	2.42E-02	2.27E-02	2.38E-02	-1.11E-03	0.57
PO	2.64E-02	2.75E-02	2.71E-02	2.93E-02	2.60E-02	2.70E-02	2.76E-02	-6.50E-04	0.65
F	9.09E-04	7.89E-04	8.11E-04	3.77E-04	1.07E-03	8.36E-04	7.21E-04	1.15E-04	0.69
Ca	5.69E-01	5.47E-01	5.82E-01	5.92E-01	5.56E-01	5.66E-01	5.74E-01	-8.04E-03	0.70
CaOH	2.42E-04	1.74E-04	9.95E-05	2.35E-05	2.39E-04	1.72E-04	1.31E-04	4.07E-05	0.70
P_3O_4H	1.29E-03	1.52E-03	9.89E-04	7.35E-04	1.51E-03	1.27E-03	1.12E-03	1.46E-04	0.71
PO_3H_2	7.26E-03	8.38E-03	4.44E-03	3.37E-04	1.03E-02	6.69E-03	5.34E-03	1.36E-03	0.76
PO_3H	2.35E-02	2.90E-02	1.81E-02	1.01E-02	3.13E-02	2.35E-02	2.07E-02	2.82E-03	0.77
O_2H_2	5.69E-04	5.58E-04	4.02E-04	2.42E-04	6.69E-04	5.10E-04	4.55E-04	5.46E-05	0.77
OH_2	4.35E-03	4.59E-03	3.72E-03	2.37E-03	5.45E-03	4.22E-03	3.91E-03	3.07E-04	0.81
P_2O_3	7.09E-05	6.38E-05	5.92E-05	4.90E-05	7.50E-05	6.46E-05	6.20E-05	2.65E-06	0.82
P_2O_5	7.79E-03	8.83E-03	6.69E-03	7.33E-03	8.67E-03	7.77E-03	8.00E-03	-2.29E-04	0.82
Ca_2PO_2	1.20E-03	1.34E-03	6.22E-04	1.30E-04	1.68E-03	1.06E-03	9.04E-04	1.51E-04	0.83
Ga	3.98E-04	4.14E-05	6.12E-05	0.00E+0	4.32E-04	1.67E-04	2.16E-04	-4.88E-05	0.84
O	6.76E-03	8.46E-03	8.47E-03	9.15E-03	6.07E-03	7.90E-03	7.61E-03	2.88E-04	0.85
PO_3F	2.59E-04	3.33E-04	1.48E-04	6.93E-05	3.73E-04	2.47E-04	2.21E-04	2.53E-05	0.86
P_2O_5H	2.92E-03	3.40E-03	1.18E-03	4.98E-04	5.24E-03	2.50E-03	2.87E-03	-3.71E-04	0.86
$CaO2$	8.95E-04	1.13E-03	4.09E-04	1.96E-04	1.28E-03	8.12E-04	7.38E-04	7.36E-05	0.89
$P_3O_4H_2$	6.09E-04	6.09E-04	1.75E-04	1.46E-04	8.73E-04	4.64E-04	5.09E-04	-4.49E-05	0.90
OH	2.71E-03	2.81E-03	2.39E-03	2.05E-03	3.14E-03	2.64E-03	2.59E-03	4.56E-05	0.92
CaPOF	8.91E-05	1.32E-04	6.92E-05	4.23E-05	1.60E-04	9.68E-05	1.01E-04	-4.29E-06	0.94
P_2OF	1.71E-04	1.53E-04	5.51E-05	5.44E-05	2.11E-04	1.26E-04	1.33E-04	-6.30E-06	0.94
Ca_2O_5H	3.07E-04	3.50E-04	7.01E-05	1.15E-04	3.92E-04	2.42E-04	2.53E-04	-1.10E-05	0.95
PO_4H	1.93E-03	1.91E-03	1.26E-03	9.72E-04	2.37E-03	1.70E-03	1.67E-03	2.84E-05	0.96

COH	5.94E-04	4.47E-04	4.85E-04	2.65E-04	7.69E-04	5.09E-04	5.17E-04	-8.17E-06	0.97
POF	4.63E-03	4.40E-03	3.79E-03	2.39E-03	6.24E-03	4.27E-03	4.32E-03	-4.52E-05	0.98
$Ca_2P_3O_2$	1.34E-03	1.48E-03	1.50E-03	1.65E-03	1.23E-03	1.44E-03	1.44E-03	-3.19E-06	0.99
CO_3	2.36E-04	2.55E-04	1.18E-04	5.80E-05	3.51E-04	2.03E-04	2.05E-04	-1.85E-06	0.99
CaF_2	1.80E-04	1.06E-04	7.05E-05	6.67E-05	1.70E-04	1.19E-04	1.18E-04	5.92E-07	0.99
sum	**1**	**1**	**1**	**1**	**1**	**1**	-	-	-

* The p-value determined by 1-way analysis of variance (ANOVA) is the probability that the difference of the means $\bar{x}^T - \bar{x}^U$ is observed if the null hypothesis (that there is no difference in means) is true. The null hypothesis is rejected if $p < \alpha$, where α is the significance level. †p-values smaller than $\alpha = 0.05$. ‡p-values between 0.05 and 0.1. §Rows corresponding to ions singled out in the discussion.

Samples that were treated with NaF show a statistically significant increase in the fraction of PO_2F^+ and CaF^+ ions detected ($p<0.05$, **Table 2.4**). While the former increases more than five-fold, the latter increases by a factor of more than 22. CaF^+ makes up about 26% of all fluoride-containing ions in the treated samples, but less than 2% in the untreated ones. The difference is less pronounced for PO_2F^+ (14.3% vs. 4.2%). CaF^+ therefore is an excellent indicator of fluoride introduced to the sample during topical fluoridation. The increase in Na^+ narrowly misses the $p<0.05$ significance level; however, the magnitude of its change appears about 2-fold greater than that of the fluoride-containing ions. Other ions are also affected, but the difference in their concentrations is 1-2 orders of magnitude less than for the fluoride-containing ions and Na^+. The only exception is Cl^-, of which about 0.8at% is lost on treatment with NaF, likely as part of an ion-exchange mechanism.

While the effect of NaF treatment on the fraction of PO_2F^+ and CaF^+ detected is significant, several other ions contribute to the overall fluorine content (**Table 2.4**). The most abundant ones are POF^+ (42% of all fluoride-containing ions in treated samples vs. 66% in untreated samples) and F^+ (8% vs. 11%), neither of which shows a significant change between treated and untreated samples. This likely explains why, after decomposition into atoms, the difference in the fluorine content of treated and untreated samples is no longer significant (**Table 2.5**). In fact, of the

minority elements Mg, Na, F, and C, only Na^+ shows significant difference, and then only at the $p<0.1$ level.

We therefore conclude that there is an increase in fluoride and sodium content with NaF treatment. However, comparison of additional data sets will be required to increase confidence in absolute numbers (F: +0.21at%, +58% relative increase; Na: +0.39at%, +71% relative increase). Further, we anticipate that CaF^+ ions in the reconstructions of treated samples will reveal regions in enamel that are accessible to topically supplied fluoride. This observation combined with the knowledge that fluoride makes the intergranular phase less soluble likely explains why topical fluoride treatments make teeth more resistant to caries.[58]

Table 2.5. Bulk composition of enamel according to APT analysis

Sample	human premolar, fluoridated					human premolar, native				1-way ANOVA
	1	**2**	**3**	$\overline{X}$	$\frac{\sigma}{\overline{X}}$ [%]†	**1**	**2**	$\overline{X}$	$\frac{\sigma}{\overline{X}}$ [%]	$p^‡$
#detector events [10^6]	27.8	28	60			35	9.1			
#ranged atoms [10^6]	21.9	15.4	40.4			16.9	6.07			
X_{Cl} [at%]	0.09	0.08	0.07	0.08	9	0.14	0.13	0.13	06	0.01§
¶X_{Na} [at%]	1.03	0.75	1.01	0.93	17	0.46	0.63	0.54	22	0.06‖
X_O [at%]	46.91	48.17	46.11	47.06	2	48.79	48.94	48.87	0.2	0.10
X_F [at%]	0.66	0.52	0.55	0.58	13	0.22	0.51	0.36	56	0.18
X_{Mg} [at%]	0.36	0.28	0.39	0.34	17	0.30	0.23	0.27	17	0.24
X_C [at%]	0.16	0.16	0.13	0.15	12	0.05	0.15	0.10	65	0.31
X_H [at%]	4.37	5.49	3.95	4.60	17	1.72	4.60	3.16	65	0.32
X_{Ga} [at%]	0.02	0.00	0.00	0.01	120	0	0.02	0.02		0.40
X_P [at%]	13.75	14.32	12.96	13.67	5	11.70	14.31	13.01	14	0.58
X_{Ca} [at%]	32.66	30.23	34.84	32.58	7	36.62	30.48	33.55	13	0.76

†Relative uncertainty calculated as the ratio of the standard deviation over the mean. ‡The p-value determined by 1-way analysis of variance (ANOVA) is the probability that the difference of the mean of mole fractions of the fluoridated and the native sample is observed if the null hypothesis (that there is no difference in means) is true. The null hypothesis is rejected if $\boldsymbol{p} < \boldsymbol{\alpha}$, where $\boldsymbol{\alpha}$ is the significance level. §p-Values smaller than $\boldsymbol{\alpha} = 0.05$. ‖p-values between 0.05 and 0.1. ¶Rows corresponding to elements singled out in the discussion.

In 3D reconstructions of APT data, recognizing the faceted cross sections of enamel crystallites is challenging (**Figure 2.5**, **Figure 2.7**). The NaF treatment resulted in diffusion of Na^+ and F^- ions into the intergranular phase, highlighting the boundaries of the crystallites, thus greatly

facilitating analysis of reconstructions (**Figure 2.7**). As in rodent enamel, Mg is enriched in this intergranular space (mean 0.35at%; range 0.15-0.51at%); in fluoridated samples levels of Na (1.27at%, 0.69-1.76at%) and F (1.36at%, 1.10-1.59at%) are also elevated in this region (**Figure 2.7e** vs. **f**). In combination with the disordered local structure around Mg observed by Mg-*K*-edge XAS, this enrichment is robust evidence for the presence of Mg-ACP in the intergranular phase; the thickness of this region is consistent with previous observations of an Mg-rich region between crystallites in human enamel.[29]
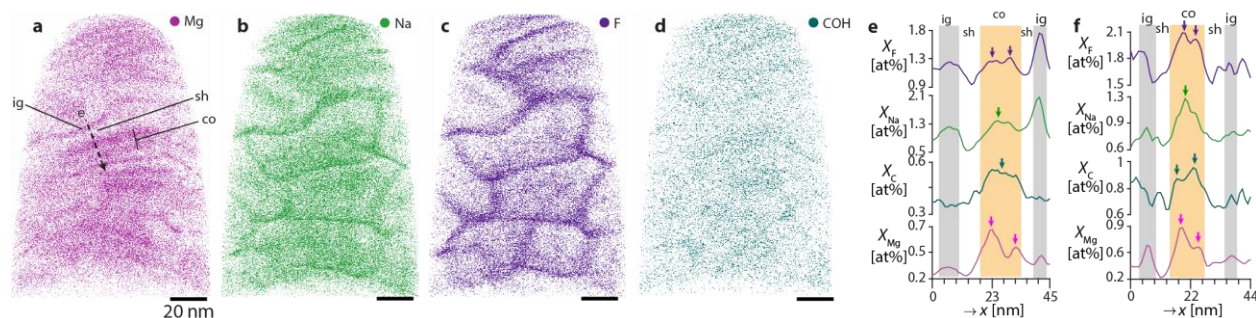
Figure 2.7. Chemical gradients in human enamel crystallites and the amorphous intergranular phase.
Rendering of Mg (**a**), Na (**b**), F (**c**), and COH (**d**) positions in a 3D reconstruction of fluoridated human enamel, viewed along the long axis of crystallites. Scale bars represent 20 nm. **e**. Concentration profiles of F (purple), Na (green), C (teal), and Mg (magenta) along the dashed line in (**a**). **f**. Concentration profiles in a crystallite from a sample without fluoridation. Note that fluoridation increases the concentration of Na and F in the intergranular phase (ig, gray highlights) vs. the core (co, orange highlights), due to short circuit diffusion, whereas the concentration in the shell (sh) is not affected.[25]

In striking contrast to rodent enamel, Mg levels in human enamel are elevated not only in the intergranular Mg-ACP, but also in two distinct layers in the core (**Figure 2.5**, **Figure 2.7a**). The core is further enriched in sodium, likely as Na$^+$, and fluorine, likely as F$^-$ (**Figure 2.7b,c**). In addition, the carbon concentration is elevated (**Figure 2.7d**), most likely due to the presence of carbonate (CO$_3^{2-}$). APT data thus supports the hypothesis that there exist a Mg- and CO$_3^{2-}$-rich core in human enamel crystallites.[59-60]

Line profiles taken approximately normal to the midplane in 20 crystallites identified in 5 reconstructions (3 NaF-treated, 2 untreated, **Figure 2.7e,f, Figure 2.8**) reveal that, on average, the two Mg-rich layers (mean 0.5at%; range 0.33-0.72at%) are also enriched in Na. However, Na levels usually peak closer to the midplane (1.2at%; 0.87-1.55at%), where F (1.4at%; 1.13-2.44at%) and C (~0.6at%; 0.45-1.01at%) are also elevated, and Mg goes through a minimum (0.4at%). The distributions of Na, F and C are more variable than that of Mg and can be asymmetric or show additional local maxima. While a form of shot noise may responsible for the latter effect, contrast in STEM-ADF shows similar variation. It is therefore possible that substituents cluster to some degree. Regardless, mole fractions are consistently significantly lower in the shell (on average, 0.22at% Mg, 0.81at% F, 0.52at% Na, and 0.32at% C). APT therefore not only confirms the core-shell structure observed in many crystallites and over large areas by STEM, but also clearly indicates that the core itself has a sandwich structure.
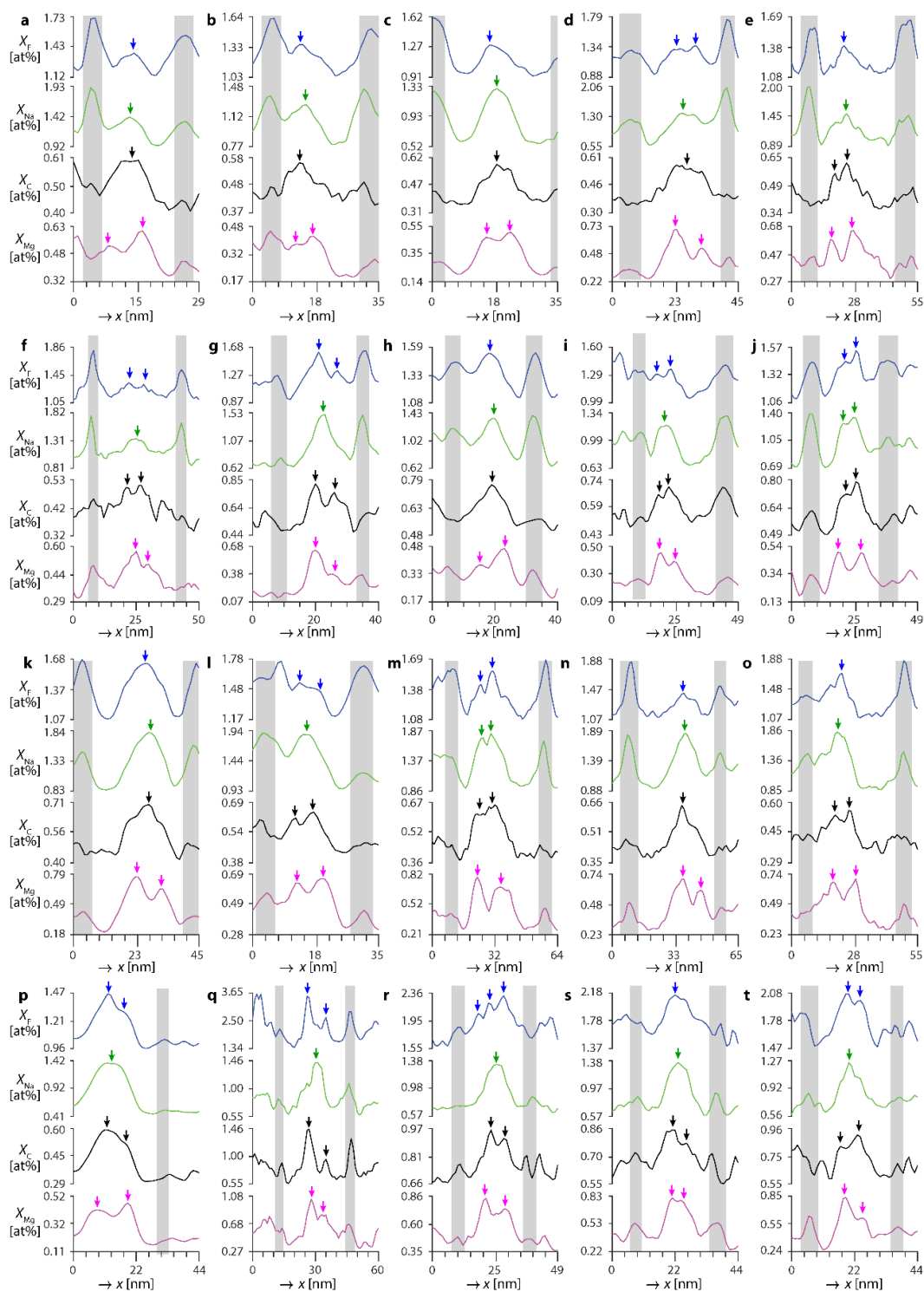
Figure 2.8. 1D concentration profiles from APT analysis.
1D concentration profiles of fluoride treated (**a-o**) and untreated (**p-t**) crystallites. Panel numbers refer to crystallites indicated in **Figure 2.5**. Regions highlighted in gray correspond to the amorphous intergranular phase

2.2.4   FINITE ELEMENT MODELING

Atomic-scale imaging unambiguously confirms the single crystalline nature of crystallites in human outer enamel (**Figure 2.2**, **Figure 2.3**). Mg, Na, and F in the core therefore must occur as substitutional defects. While the large size mismatch between Mg and Ca ($\Delta r/r_{Ca}$ = -28%) increases apatite solubility, incorporation of fluoride, which is slightly smaller than OH$^-$ ($\Delta r/r_{OH}$ = -3%), decreases solubility mildly.[61-62] The effect is more complex for sodium ($\Delta r/r_{Ca}$ = +2-6%) because its introduction on calcium sites is coupled to creation of vacancies on channel sites, or substitution of CO_3^{2-} for PO_4^{3-}. The latter is known to increase solubility.[63] Taking into account the effect of each substitution, we expect that the core is more soluble than the shell of the crystallite.

We furthermore expect a significant contraction of the apatite lattice in the Mg-rich layers.[64-67] Lattice parameters determined by DFT calculations and X-ray diffraction experiments, after correction for thermal expansion, agree within 1%, and indicate a contraction in both the a- and c-directions with increasing level of Mg substitution (**Table 2.6**, **Table 2.7**, **Figure 2.9**, **Figure 2.10a-d**.)[68]
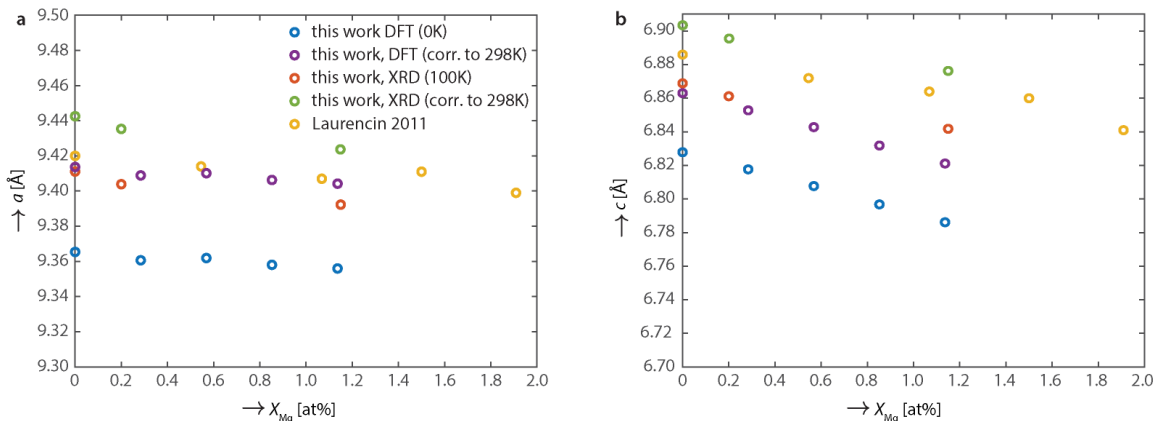
Figure 2.9. Apatite lattice parameters as a function of magnesium concentration.
Plot lattice parameters a (**a**) and c (**b**) as a function of the magnesium mole fraction X_{Mg} in Mg-substituted OHAp, including values determined by XRD collected by Linus Stegbauer (100K, orange; corrected to 298K using linear coefficient of thermal expansion (CTE) reported by Babushkin and coworkers, green)[69], DFT calculated by Prasanna Balachandran (0K, blue; corrected to 298K using linear CTE, purple)[69], and experimental values obtained by Laurencin and coworkers (yellow).[64]

Carbonate substitution also results in a contraction of the lattice in the *a*-directions.[70]

However, there is a mild expansion of the lattice in the *c*-direction that partially offsets the effect

of Mg (**Figure 2.10e-h**).

Table 2.6. Composition and lattice parameters for Mg-substituted and pure OHAp samples

	OHAp*	Mg-OHAp†	Mg-OHAp†
X_{Mg} [at%]	0.004 ± 0.00003	0.22 ± 0.007	1.15 ± 0.05
Empirical formula	$Ca_5O_{13}P_3H$	$Ca_{4.9}Mg_{0.04}O_{12.96}P_3H_{0.96}$	$Ca_{4.7}Mg_{0.25}O_{12.95}P_3H_{0.95}$
Temperature/K	100(2)	100(2)	100(2)
Crystal system	hexagonal	hexagonal	hexagonal
Space group	$P6_3/m$	$P6_3/m$	$P6_3/m$
a [Å]	9.4111(10)	9.4039(15)	9.3923(19)
b [Å]	9.4111(10)	9.4039(15)	9.3923(19)
c [Å]	6.8689(10)	6.8612(13)	6.8419(13)
α [°]	90	90	90
β [°]	90	90	90
γ [°]	120	120	120
Volume [Å³]	526.9(1)	525.5(2)	522.7(2)

*determined by PXRD, †determined by single crystal XRD
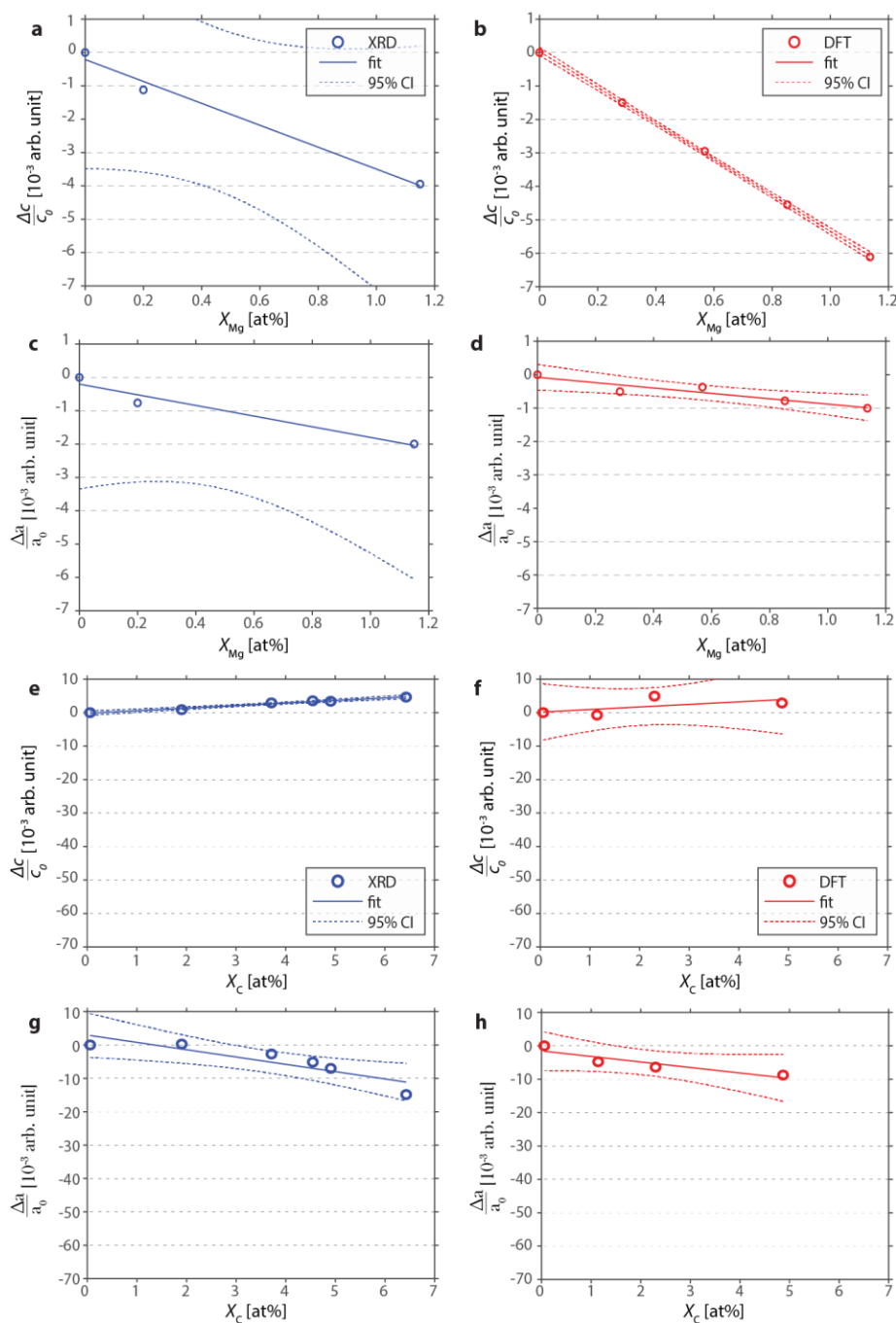
Figure 2.10. Relative change in lattice parameters with increasing magnesium or carbonate concentration.
Plot of relative change in the lattice parameter in the *c-* (**a,b,e,f**) and *a*-direction (**c,d,g,h**) in synthetic Mg-substituted OHAp, as calculated by Prasanna Balachandran (**a-d**) and carbonate substituted OHAp[70] (**e-h**) as a function of impurity concentration. Values were calculated using lattice parameters determined by XRD (**a,c,e,g**; blue) or DFT (**b,d,f,h**; red). Also given are predicted values for a linear model ($\Delta c/c_0$, $\Delta a/a_0 \sim \eta \cdot X_C + b$) fit to the data (solid line), and confidence intervals at the 95% probability level (dashed lines).

Table 2.7. Linear fit parameters for lattice relative change in lattice parameters.

independent variable	method	dependent variable	η	CI of η	b	CI of b	R^2
X_{Mg}	XRD	η_c	-0.33	±0.04	-2.1E-04	±2.6E-04	0.99
		η_a	-0.16	±0.04	-2.0E-04	±2.5E-04	0.95
	DFT	η_c	-0.54*	±0.01	3.4E-05	±3.7E-05	0.9997
		η_a	-0.08*	±0.02	-7.6E-05	±1.2E-04	0.88
X_C	XRD	η_c	0.08*	±0.04	-1.2E-03	±1.6E-03	0.98
		η_a	-0.22*	±0.54	2.8E-02	±2.2E-02	0.78
	DFT	η_c	0.08	±0.50	1.2E-03	±1.4E-02	0.36
		η_a	-0.17	±0.47	-1.5E-02	±1.3E-02	0.85

***Values used in finite element model. Confidence intervals were determined at the 95% probability level. Note that slope and intercept were calculated with X_{Mg} in arbitrary units (range 0-1), and are therefore given in arbitrary units, *not* in units of (at%)$^{-1}$.

Because enamel crystallites are coherent, lattice parameter changes that result from Mg^{2+}- and CO_3^{2-}-gradients are in effect residual (eigen) strains and may therefore cause a net residual stress. Residual stresses in turn can affect the overall mechanical performance of a material, and also impact the local chemical potential and therefore solubility. To explore these possibilities, we predicted residual stresses in an idealized crystallite (**Figure 2.11**) using finite element (FE) modeling. In mechanical equilibrium, the core experiences a net tensile stress, with distinct maxima in the Mg-rich layers (**Figure 2.11a-c**). The highest compressive stress (-46.4 MPa) is found on the free surface parallel to the (001) plane (**Figure 2.11b**), again in the Mg-rich layers. The shell of the crystallite experiences compressive residual stresses (**Figure 2.11c**). On the majority of the surface, these stresses are near -39 MPa. Although absolute values of the stresses reported here will vary, as real crystallites differ in shape and composition from the highly idealized model we employ here, we believe that the model captures trends quite well and provides insights on how we can expect crystallites to behave on average.
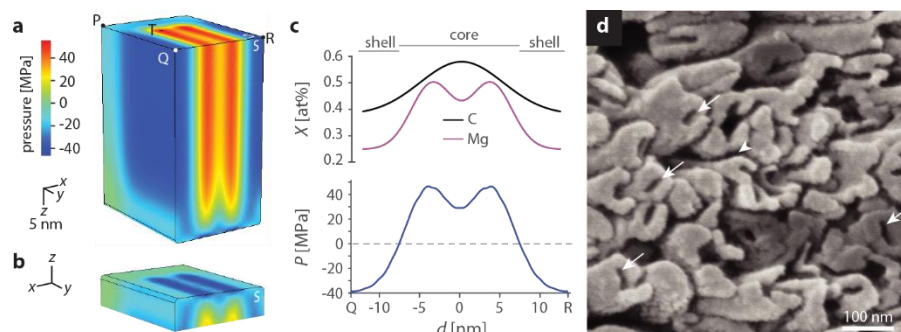
Figure 2.11. Impact of substitution on mechanical and chemical properties of human enamel crystallites.
a. Rendering of the scalar pressure, calculated as one third of the trace of the stress tensor, as a measure of residual stress in an FE model of an enamel crystallite. Note that symmetric boundary conditions were applied to two faces (white "S"); values on these represent internal rather than surface stresses. **b**. View of (**a**) showing the free surface parallel to the (001) plane. **c**. Plot of the mole fractions of C (black) and Mg (magenta), and of the residual pressure (blue), against the distance from Q to R. **d**. SEM image of an acid-etched enamel section in which crystallites emerge end-on, displaying intergranular corrosion (arrowhead) and preferential dissolution of the core (white arrows). Data presented in panel **d** was recorded by Paul Smeets.

For instance, at the water-accessible endcap (**Figure 2.11b**), stresses in the core are between 4 and 40 times higher than in the shell. This is expected to increase the solubility of the core relative to the shell. Indeed, the core of outer enamel crystallites is preferentially etched, similar to the intergranular Mg-ACP (**Figure 2.11d**), and consistent with reports for crystallites with a dissolved core extracted from human caries lesions.[71-72] The core shell-architecture and associated residual stresses are thus an important aspect of disease progression and may be used for the modeling of dissolution and re-precipitation during the progression of caries lesions.

Compressive stresses in the shell may further impede crack initiation, extend the size range at which crystallites perform at their theoretical strength,[73] and deflect cracks, thereby increasing the tolerance of enamel.[37,74] The strong modulation of stresses and the resulting strain just beneath the surface of the endcaps may also be responsible for the CDL feature observed in electron

microscopy. While the Mg-rich layers appear to be parallel to the CDL, confirmation that the CDL runs in between these layers would require correlative imaging of the same crystallite by STEM and APT. Although correlative imaging of this kind is not unprecedented, it is a very significant challenge, especially for beam sensitive materials such as enamel.[28,75] Such imaging would, however, be particularly rewarding, as it could also address the spatial correlation between contrast in STEM-ADF and local concentration maxima reported by APT.

While this model takes into account the gradients in Mg and CO_3, a more comprehensive model could be built to include the presence of F and Na as well. Previous work suggests increasing F concentration causes a contraction in the *a*-directions (**Figure 2.12, middle**), and almost no effect on the lattice parameter in the *c*-direction (**Figure 2.13, middle**).[76-77]
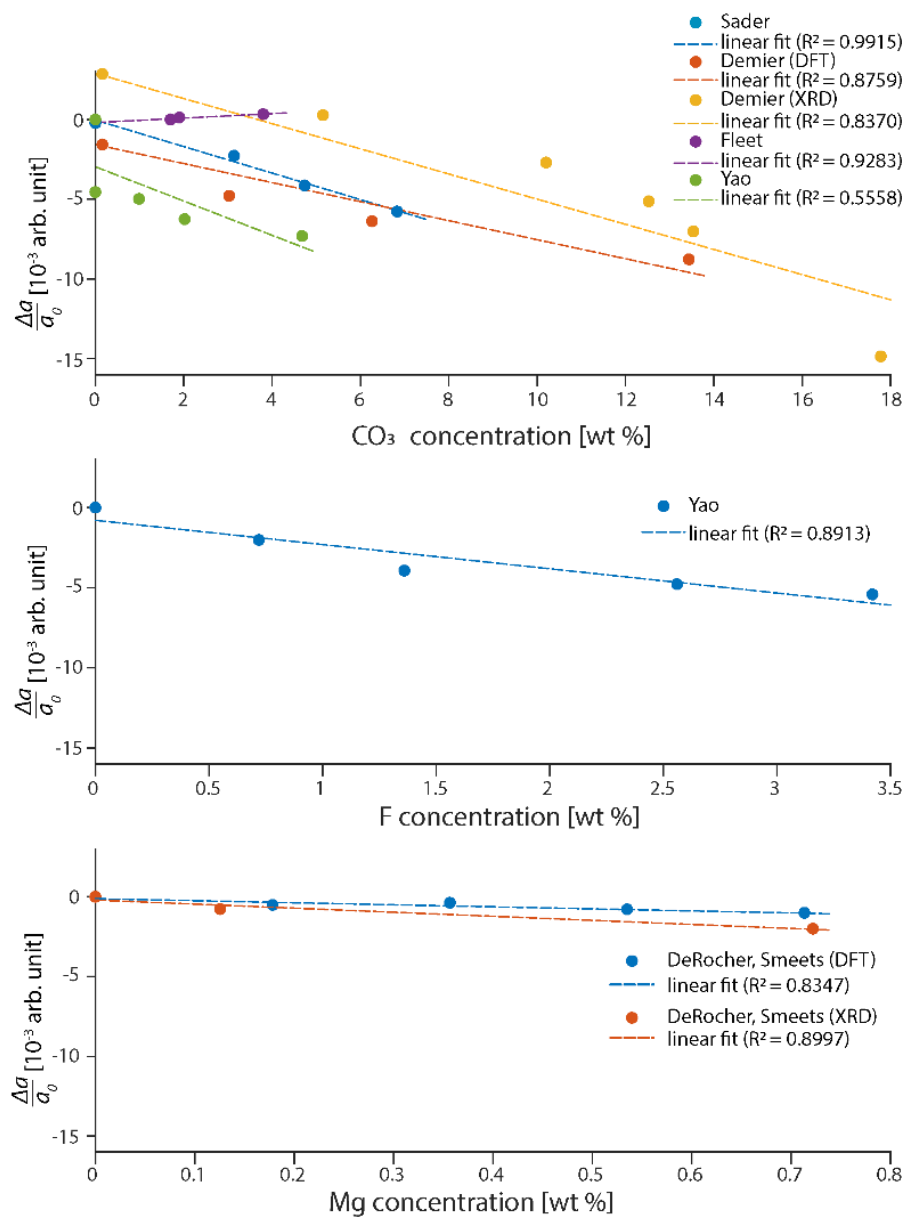
Figure 2.12. Relative change of the apatite *a*-axis lattice parameter with increasing mass fraction of carbonate, fluoride, and magnesium.
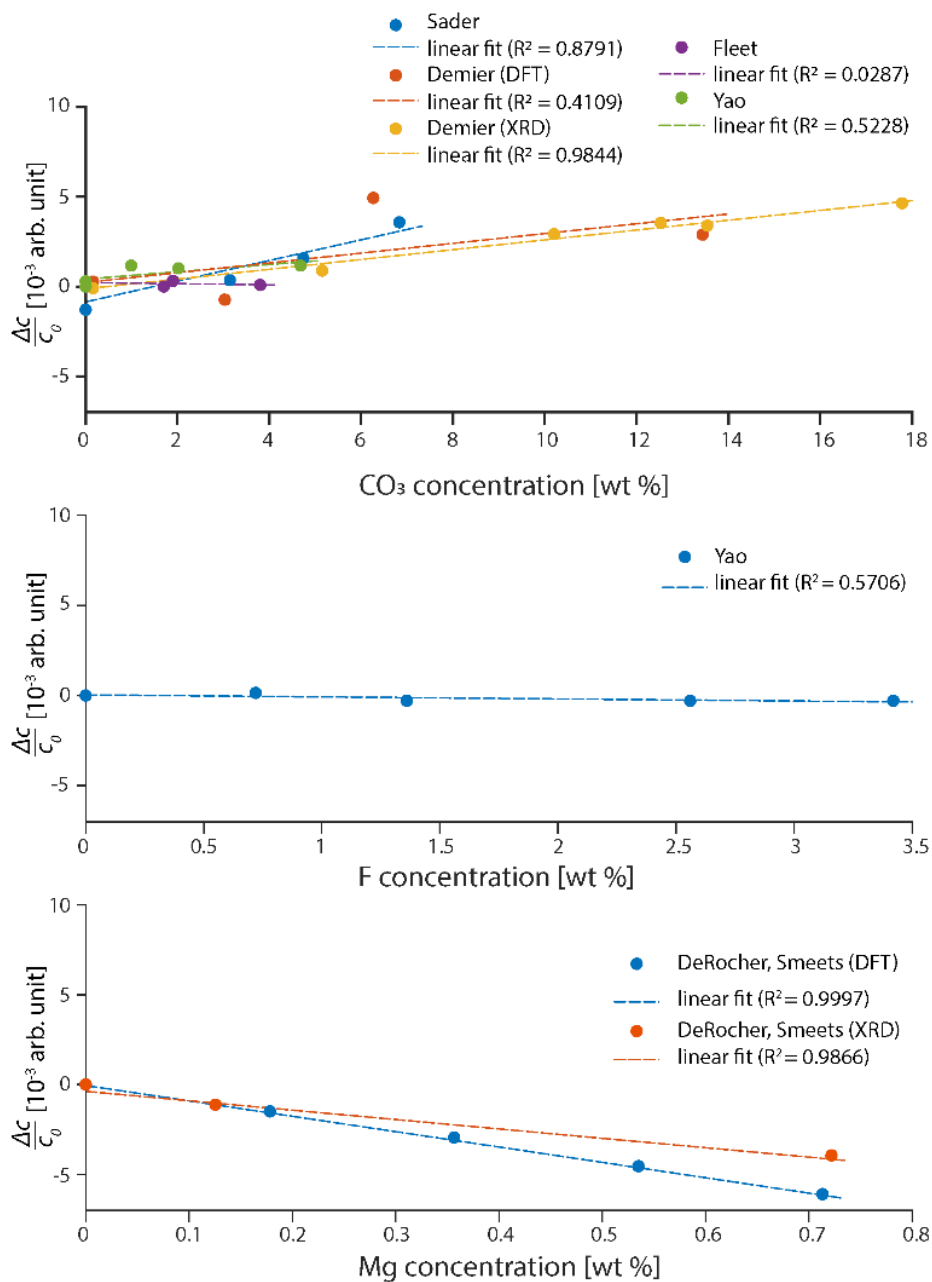
Figure 2.13. Relative change of the apatite *c*-axis lattice parameter with increasing mass fraction of carbonate, fluoride, and magnesium.

However, in order to fully capture the stress state of the crystallites, we would need to also know the combined effect of all these substitutions on the lattice parameters. Sader and co-workers characterized synthetic OHAp containing Mg, Na, and CO_3 and found that, with Mg concentration held constant, increasing CO_3 (and Na to charge balance) concentration lead to a decrease in the *a*-axis lattice parameters but an increase in the *c*-axis lattice parameter relative to unsubstituted OHAp.[78] Other groups have investigated the effect of F, Na, CO_3 co-substitution, and found once again that this led to a decrease in the *a*-directions and an increase in the *c*-directions.[79-80] Taken together, it appears that all of these impurities together very likely result in a contraction of the *a*-axis lattice parameters. The effect on the *c*-axis lattice parameter is less clear and requires further analysis to determine the net effect of all these substitutions together.

In order properly compare the effects of substitutions on the OHAp lattice, it is also necessary to have detailed compositional information. As the literature data cited here is reported in weight percent, an exact composition or empirical formula for the material characterized must be available so one can ascertain the fraction of atomic sites that have been substituted. Without that information, it is impossible to ascertain if nominally identical weight fractions of an impurity represent the same level of substitution. It is also important to note that the trends described in literature are from analysis of samples with higher impurity concentrations than are present in crystallite cores. While instructive, it is also necessary to investigate the effect of substitutions at concentrations consistent with those found in crystallite cores in order to verify that the trends are also valid at low concentrations. Additionally, it would be beneficial to characterize these synthesized apatites in a way that establishes the distribution of impurity elements within the

particles, to insure that they are homogeneously distributed rather than segregated to surfaces or grain boundaries.

In summary, we find strong evidence that the core-shell architecture and resulting residual stresses impact the dissolution behavior of human enamel crystallites and provide a plausible avenue for extrinsic toughening of enamel. This leads us to the question of how the gradients are created. During amelogenesis, mineral first precipitates in the organic enamel matrix as ribbons of amorphous calcium phosphate (ACP).[81-83] ACP is tolerant of impurities, and it is conceivable that the ribbons retain Na^+ and CO_3^{2-} as they crystallize by an unknown mechanism. Crystallites initially grow much slower in thickness than in width. In human primary teeth for instance, ribbons are 3 nm thick and 29 nm wide at a distance of 25 µm from the ameloblasts, and grow to 10-by-58 nm by the time the ameloblasts have moved an additional 175 µm (**Figure 2.14**).[81]
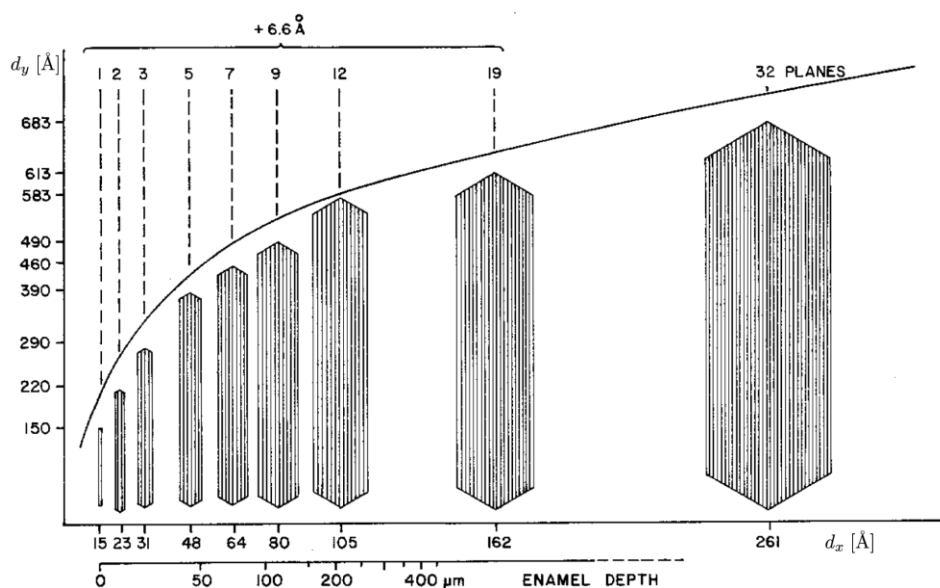
Figure 2.14. Plot of crystallite dimensions in the intermediate (d_y; width) and short direction (d_x; thickness) in primary human enamel.
Note that variables were re-named for consistency with the notation used in this manuscript. Also provided is the distance from the surface of ameloblasts to areas in which crystals with the observed thickness are found. Adapted from Daculsi and Kerebel.[81]

In this first phase, the faster growth direction is thus parallel to the Mg rich layers (**Figure 2.15**; for relative growth velocities, see **Table 2.8**), suggesting that Mg substitution breaks the crystal symmetry. Mg likely acts on its own, or in concert with organic matrix molecules, by blocking active sites for growth in the direction normal to the layer direction, through anisotropic stresses generated as it incorporates into the crystal, or through a combination of these effects. These mechanisms would require that ameloblasts or other organic matrix molecules introduce Mg into the system after the ribbon has formed, and indeed the Mg concentration in porcine peaks at approximately 0.329 wt% in the late secretory/early maturation stage.[84] Consistent with a regulatory role, perturbation of putative Mg transporters is known to impact amelogenesis, even though the impact on crystallite shape is not known.[85-87]
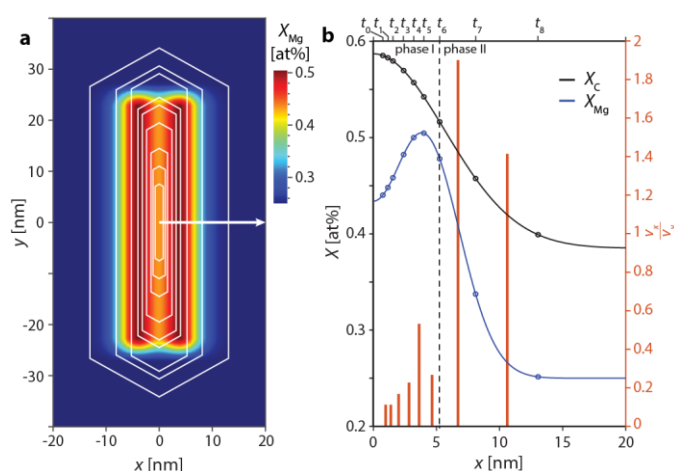
Figure 2.15. A model for human enamel crystallite growth during amelogenesis.
a. Schematic drawing of growth stages (timepoints t_0-t_8) of human primary enamel crystallites (white hexagons, after Daculsi and Kerebel, Ref. [81]) superimposed on an idealized map of the Mg concentration based on observation of human permanent enamel crystallites reported herein. **b**. On the left y-axis, plot of the mole fraction of Mg (blue) and carbon(ate) (black) against distance along the white arrow in (**a**). The open circles indicate the mole fractions at the interface of the growing crystallite at t_0-t_8. On the right y-axis, plot of the ratio of the average growth velocities in the x- and y-directions in successive time intervals (**Table 2.8**). Note that scaling of the time axis is unknown, and likely non-linear. As a consequence, absolute speeds cannot be determined and may vary.

Table 2.8. Data from Daculsi and Kerebel.[40] Note that d_x is commonly referred to as the thickness, and d_y is referred to as the width. While times t_0-t_8 are not known in absolute terms, the ratio of growth velocities, v_x/v_y, for the intervals between successive time points can be determined.

	d_x [Å]	d_y [Å]	Δd_x [Å]	Δd_y [Å]	$\dfrac{v_x}{y} = \dfrac{\Delta d_x}{\Delta d_y}$	$\dfrac{d_y}{d_x}$
t_0	15	150	0	0	N/A	0.1
t_1	23	220	8	70	0.11	0.1
t_2	31	290	8	70	0.11	0.11
t_3	48	390	17	100	0.17	0.12
t_4	64	460	16	70	0.23	0.17
t_5	80	490	16	30	0.53	0.16
t_6	105	583	25	93	0.27	0.18
t_7	162	613	57	30	7.9	0.26
t_8	261	683	99	70	1.41	0.38

During the second phase of crystal growth, which likely occurs during the maturation stage of amelogenesis, growth slows down significantly. At the same time, the ratio of the growth velocities changes, with crystals growing thicker rather than wider. In human primary enamel, this results in mature crystallites with a thickness of 26 nm and a width of 80 nm.[81] The Mg-poor shell is likely formed during this period. Slow growth at low supersaturation, which may be combined with a significant drop in Mg (0.184 wt%) and Na (0.68 wt%) concentration in the enamel matrix,[84,88] is expected to result in low rates of incorporation of impurities on the apatite lattice. Any Mg still present would accumulate ahead of the interface of the growing crystallite. In the final stage of maturation, as crystals start to impinge on each other, the Mg/Ca ratio in the matrix would rise rapidly, and trigger precipitation of the amorphous intergranular phase as it exceeds the threshold for Mg-ACP.[67] While this mechanism is consistent with and provides an explanation for a number of independent observations, we note that the data on which we base our hypothesis come from both primary and permanent human enamel and include observations in other species. A thorough compositional analysis of immature enamel ribbons and crystallites in one species would greatly aid in confirming the proposed sequence of events. Additionally, it is important to

note that this proposed mechanism does not account for how other crystallites growing in the vicinity may affect the morphology. While the chemical environment will strongly affect the resulting crystallite size and shape, the space into which these crystallites are growing is another important factor to consider in future mechanistic models.

Independent of the accuracy of this proposed mechanism, it is evident that the concentration of Mg and other minor ions at the surface of the crystallite varies systematically during amelogenesis of human permanent teeth. These changes, in turn, imply variations in the medium surrounding the crystallites, which begins as enamel matrix which is then degraded and removed as crystallites thicken. This may impact how enamel matrix proteins and their degradation products, thought to be involved in controlling enamel crystallite formation, interact with the mineral phase and each other.

The idea that ions that are not required for amelogenesis, such as fluoride, are incorporated into the crystallite core has an important corollary. Enamel forms over very specific times during the development of different teeth (in humans starting as early as second trimester in utero until the late teens), is not significantly remodeled, and is very well preserved in remains and fossils. Crystallite cores might thus encapsulate spatially resolved biomarkers for environmental exposure, disease, or medical intervention, over an extended period of time. With APT and correlative imaging and spectroscopy, this record is now accessible and might help decipher for instance genetic pre-disposition to caries or the mechanism behind molar-incisor hypomineralization (MIH), a dental developmental defect of unclear etiology that affects as many as 20% of all school children.[89-90]

2.3   CONCLUSIONS

In this work, we both confirmed the presence of an amorphous intergranular film surrounding human enamel crystallites, and showed that human enamel crystallites are chemically more complex than those found in rodent enamel (often used as a model system for human enamel). Specifically, we discovered that human crystallites have a core-shell structure. Compared to the shell, the core is enriched in magnesium, sodium, fluoride, and carbonate ions that are present as impurities. Additionally, Mg ions form two layers on either side of the core. While the concentration of these impurity ions is relatively low, FEM indicates that they may cause distortions in the OHAp lattice that result in residual stresses in the crystallites. The residual compressive stress on the crystallite surface may toughen the material, improving its hardness and wear resistance. At the same time, the stress likely makes the crystallite more soluble when exposed to acid.

Improved understanding of the chemical gradients present in human enamel crystallites now enables efforts to simulate degradation processes, and may lead to breakthrough treatments for diseases like caries. This information also elucidates the chemical environment present in the oral cavity during amelogenesis and allows us to propose a new model for amelogenesis. Finally, future analysis of crystallite cores may shed light on environmental impact on human health or ecological systems and allow for the study of epigenetic mechanisms of conditions, such as MIH.

2.4   MATERIALS AND METHODS

2.4.1   CONSUMABLES

Unless otherwise specified, all solutions were prepared using ultra-pure water (18.2 MΩ·cm) dispensed from a Barnstead Nanopure UF+UV unit (Thermo-Fisher Scientific, Waltham,

MA). Lactic acid ($C_3H_6O_3$) (Mallinckrodt Chemicals, Center Valley, PA); propionamide (98%), NaF (Sigma-Aldrich, St. Louis, MO); NaH_2PO_4, Na_2HPO_4, HNO_3 (65wt%), $Mg(NO_3)_2 \times 6\ H_2O$ (99%), $Ca(NO_3)_2 \times 4\ H_2O$ (99%, Lot No. 86432), ethanol (VWR, Radnor, PA); $Ca(NO_3)_2 \times 4\ H2O$ (99.98%, Lot No. 61600281), formaldehyde (CH_2O) (Alfa Aesar, Tewksbury, MA); $(NH_4)2HPO_4$ (99%, Lot A0059707, Merck KGaA, Darmstadt, Germany); PELCO® liquid silver paint, graphite tape (Ted Pella, Redding, CA); EPO-TEK 301 (Epoxy Technology, Billerica, MA); CarbiMet SiC grinding paper, Metadi supreme polycrystalline aqueous diamond polishing suspension, Microcloth polishing cloth (Buehler, Lake Bluff, IL). MM22 microtip coupons for FIB liftout (CAMECA Instruments, Madison, WI).

2.4.2   PREPARAITON OF ENAMEL SECTIONS

Deidentified human premolars extracted for orthodontic reasons by Drs. Akers, Stohle, and Borden of The Center for Oral, Maxillofacial, and Implant Surgery (Evanston, IL) and Professor Ana Bedran-Russo (University of Illinois at Chicag) were kept in 10% buffered formalin at room temperature for 10 days, and at 4˚C thereafter. Before use, samples were rinsed with water and dried under a gentle stream of nitrogen gas ("rinsed and dried"). Samples were embedded in Epo-Tek 301 epoxy, sectioned along the buccal-lingual line, ground with SiC paper (600, 800, 1200 grit), and polished on a Buehler Trident polishing cloth with polycrystalline diamond suspensions (3 μm, 1 μm), rinsed and dried. Some sections were treated with fluoride by immersion in 50 mL of aqueous NaF (250 mM, pH 8.4) under gentle agitation using an orbital shaker, at 37°C for 24 hours, then rinsed and dried. Some sections were exposed to lactic acid (250 mM, pH 4, for ~20 seconds), and subsequently rinsed and dried. Some sections, oriented such that rods (and crystallites) emerge approximately perpendicular to the surface, were positioned under an angle of

roughly 45 degrees with respect to the underlying lab bench surface. The sample was etched using a steady stream of droplets of lactic acid (250 mM, pH 4) flown across the surface for a total of 30 seconds. Thereafter, the tooth sections were quenched immediately in ethanol, rinsed and dried.

Unless otherwise noted, samples were affixed to an aluminum stub using carbon tape, coated with AuPd (~25 nm) using a Denton Desk IV sputter coating system (Denton Vacuum, Moorestown, NJ). The surface of the sample was then grounded to the stub using colloidal silver paint.

2.4.3   SCANNING ELECTRON MICROSCOPY (SEM)

SEM was performed using a Hitachi S4800-II or a Hitachi SU8030 (Hitachi High-Tech, Schaumburg, IL), both equipped with a cold cathode field emission electron gun, operated at an accelerating voltage of 5kV and an emission current of 8600 nA. Images were acquired using secondary electron contrast.

2.4.4   (SCANNING) TRANSMISSION ELECTRON MICROSCOPY (TEM, STEM)

Lamellae were prepared from ground and polished, transverse sections of outer, buccal human enamel. A dual-beam FIB/SEM (FEI Helios NanoLab or FEI Strata 400) with a gallium liquid metal ion source (LMIS) operating at an accelerating voltage of 2–30 kV was used to prepare FIB samples for TEM. A ~200 nm thick layer of protective carbon was deposited on a 2 μm x 15 μm area of interest, either by using the electron beam (5 kV, 1.4 nA) through decomposition of a phenanthrene precursor gas (FEI Helios Nanolab), or by selecting a similar area of interest using a permanent marker deposition method[91] (FEI Strata 400). On top of the carbon, a ~1 µm thick protective platinum layer was deposited using the ion beam (30 kV, 93 pA) through decomposition of a (methylcyclopentadienyl)-trimethyl platinum precursor gas. Subsequently, two trenches were

cut to allow for a roughly 2 µm thick lamella of enamel. Next, the micromanipulator was welded onto the lamellae, and the sample was cut loose from the bulk material. An in situ liftout of the sample was performed, and the lamellae was welded onto a TEM half-grid. After thinning to about 80 nm in a sub-region of the lamellae (5 kV, 81 pA), the thin section was cleaned at low voltage and current (2 kV, 28 pA).

STEM images were acquired on a JEOL JEM-2100F (JEOL USA, Peabody, MA), a JEOL GrandARM 300F, or an aberration-corrected FEI Titan Themis (FEI Company) equipped with a monochromator, a side-entry double tilt liquid nitrogen-cooled sample holder (Gatan 636; Gatan, Pleasanton, CA), and a cryogenically cooled anti-contamination device (for typical conditions please see **Table 2.1**).

2.4.5   STEM-EDS

EDS spectrum images of regions of interest chosen in STEM HAADF images were acquired on a windowless 100 mm2 XMaxN 100TLE Silicon Drift Detector (SDD) with a solid angle of ~0.98 sr (Oxford Instruments NanoAnalysis, Concord, MA) with a dwell time of 5 µs/pixel.

2.4.6   CRYO-STEM-EELS

EELS 2D spectrum images were acquired on a Titan Themis (FEI Company) using a K2 Summit direct electron detector in counting mode (Gatan Inc, Pleasanton, CA). This direct electron detector with high quantum efficiency (DQE up to 80%) allowed simultaneous acquisition of all relevant inner shell ionization (core loss) edges at high energy resolution and low background levels despite the low dose required to minimize beam damage.[52] The entrance aperture was 5 mm, the energy dispersion 0.5 eV/channel. The beam current was 4.0-8.5 pA, the dwell time 2.5

μs/pixel. STEM-ADF images were recorded in parallel. Concentration maps were extracted by fitting and subtracting the pre-edge background with a linear combination of power laws and integrating the intensity under the EELS edge of interest. MCR analysis of the Mg-$L_{2,3}$ edge region was performed as described previously.[92]

2.4.7   X-RAY ABSORPTION SPECTROSCOPY (XAS)

XAS measurements were performed at the Spherical Grating Monochromator (SGM, 11ID-1) at the Canadian Light Source (Saskatoon, SK), following a literature protocol.[58] Briefly, enamel from de-identified human third molars was ground into a powder using an agate mortar pestle and spread on graphite tape. Samples were scanned relative to the edge Mg K-edge (1303 eV) from -60 to -12 eV in steps of 2 eV, -12 to -8 eV in steps of 0.5 eV, -8 to 30 eV in steps of 0.1 eV, 30 to 190 eV in steps of 0.2 eV, 190 to 300 eV in steps of 0.3 eV and 300 to 400 eV in steps of 0.5 eV, with a constant dwell time of 2 seconds/step. Monochromator energy calibration was performed by setting the first absorbance maxima of the MgO reference sample spectra to 1309.5 eV. X-ray fluorescence intensity was measured simultaneously with four solid state silicon drift energy dispersive X-ray detectors (Amptek, Bedford, MA). Incident flux was measured by recording the current from a gold mesh upstream. The exit slit was adjusted and the undulator detuned to reduce flux to prevent saturation of X-ray fluorescence detectors when measuring concentrated reference samples. Between 1 and 7 scans were collected for each sample and averaged. No beam-induced changes were observed when comparing sequential spectra. The Mg X-ray fluorescence intensity was isolated from the total fluorescence intensity containing contributions from X-ray fluorescence from other elements and the scattered incident beam using

custom written code in Mathematica (Wolfram Research, Champaign, IL). For XANES spectra, please see **Figure 2.4**.

Absorption data were normalized, background subtracted using AUTOBK, and converted to k-space using Athena.[93] Edge energy (E_0) was set to the maximum of the first derivative of the absorption spectra. $\chi(k)$ data were weighted by k^2 and Fourier transformed over a k-range of 2-9.5 Å^{-1}, applying a Hanning window with a sill width of 1 Å^{-1}. Theoretical photoelectron scattering amplitudes and phase shifts based on the crystal structures of dolomite[94], huntite[95], whitlockite[96], and hydroxyapatite[66] were calculated using FEFF6[97]. Shell-by-shell fitting of the EXAFS data was performed in R-space using Artemis[93]. An energy shift parameter (E_0) was maintained constant for the scattering paths but allowed to vary between samples. The amplitude reduction factor ($S_0{}^2 = 0.8$) was determined based on a fit to the dolomite, huntite and whitlockite spectra with coordination numbers constrained based on their respective crystal structures. Multiple scattering in the carbonate reference samples was accounted for following Reeder and coworkers.[98] Enamel and ACP EXAFS spectra were fit using a model based on the Ca[II] site of OHAp, consisting of a single Mg-O and two Mg-P scattering paths.[99-100] To minimize the number of fitting parameters, the coordination number and σ^2 for the two Mg-P paths were constrained for each sample but allowed to vary between samples. For EXAFS spectra, please see **Figure 2.4**. For fitted parameters, see **Table 2.9**.

Table 2.9. Mg K-edge EXAFS fit parameters.

Sample	Path	R (Å)	CN	σ^2	ΔE (eV)	R-factor
Dolomite	$Mg-O_1$	2.07(1)	6*	0.0038(9)	4.4	0.7%
	Mg-C	2.99(3)	6*	0.001(3)		
	Mg-O-C	3.14(6)	12*	0.005		
	$Mg-O_2$	3.48(4)	6*	0.010(8)		
Huntite	$Mg-O_1$	2.06(1)	6*	0.006(1)	3.5	1.2%
	Mg-C	3.08(8)	6*	0.01(2)		
	Mg-O-C	3.4(2)	12*	0.02		
	$Mg-O_2$	3.38(4)	6*	0.01(1)		
Whitlockite	Mg-O	2.08(2)	6*	0.006(2)	5.3	5.5%
	Mg-P	3.37(6)	6*	0.006(7)		
	Mg-Ca	3.50(4)	6*	0.004(4)		
Mg-ACP	Mg-O	2.02(2)	3.8(8)	0.005(3)	1.8	1.3%
	$Mg-P_1$	3.17(6)	3(3)	0.005(9)		
	$Mg-P_2$	3.39(8)	3(3)	0.005(9)		
Mouse Enamel	Mg-O	2.03(2)	4(1)	0.00899	0.9	1.0%
	$Mg-P_1$	3.18(6)	3(3)	0.003(9)		
	$Mg-P_2$	3.40(9)	3(3)	0.003(9)		
Human Enamel	Mg-O	2.09(2)	4[†]	0.006(3)	-10.9	3.3%
	$Mg-P_1$	3.08(8)	3[†]	0.003(8)		
	$Mg-P_2$	3.28(7)	3[†]	0.003(8)		

Data for reference compounds was taken from Ref [25]. ΔE was fixed for each individual paths but varied between samples. Bold coordination values were held constant. Uncertainty given in parenthesis for last digit. *designates a CN from crystal structures. [†]designates CN fixed based on previous work with mouse enamel to improve fit.

2.4.8   ATOM PROBE TOMOGRAPHY (APT)

Samples for APT were extracted ca. 10 μm below the external enamel surface on mid-coronal cervical sections of human premolars, using a Dual Beam SEM/FIB (Helios NanoLab; FEI Company), and following standard protocols [21,56]. Briefly, a 200 nm thick layer of protective platinum was deposited using the electron beam (5 kV, 1.4 nA) on a 2 μm x 25 μm area of interest through decomposition of a (methylcyclopentadienyl) trimethyl platinum precursor gas. A thicker coating of FIB platinum (~400 nm) was then deposited using the ion beam (30 kV, 93 pA). An angled cut was then made on either side of the Pt strap, and one end was cut free and attached to an in-situ manipulator (Omniprobe, Dallas, TX) using FIB-Pt. After cutting the final side free, 1-

2 μm segments were attached to the top of silicon posts on the APT array with FIB-Pt. Tips were sharpened in the ion beam using annular mill patters with progressively smaller inner and outer diameters (16-30kV, 0.28−0.47 nA). The majority of contamination/gallium implantation was removed by a final cleaning step (2 kV, 0.25 nA).

APT analysis was performed using a LEAP 5000 XS (CAMECA Instruments) with a laser operating at a wavelength of 355 nm and a pulse frequency of 250 kHz, at a power of 40 pJ. The temperature in the analysis chamber was kept 25 K, the pressure $<10^{-8}$ Pa. The DC potential on the microtip was adjusted to maintain an evaporation rate of 0.005 ions per laser pulse. 3D reconstructions of the sample tips were made using the IVAS software package (CAMECA Instruments). Standard parameters were used for all reconstructions.

For representative APT spectra, please see **Figure 2.6**. For peak identities and integration limits, see **Table 2.3**, and for a comparison of the composition of treated and untreated samples see **Table 2.5**. In this manuscript, we analyze data from three reconstructions of fluoridated enamel, and two reconstructions of enamel that were not fluoridated by us. Inspection revealed that the cross sections of 8 crystallites (8 fluoridated, 0 non-fluoridated) were fully contained in the reconstructions, and that of 14 crystallites (7/5) were partially contained. For 20 crystallites (15/5) we were able to extract 1D concentration profiles approximately normal to the midplane of the crystallite, using ROIs that were defined manually in IVAS (CAMECA Instruments). For the remaining, too little of the crystallite was contained in the reconstruction, or it was not possible to deduce the orientation. As a consequence, 1D profiles could not be extracted. 1D profiles were corrected for homogeneous background.

2.4.9 HYDROTHERMAL SYNTHESIS OF OHAp AND Mg-SUBSTITUTED OHAp SAMPLES

Hydroxylapatite (OHAp, 0 at% Mg) was synthesized following a literature protocol.[101] Briefly, 5 mL of an aq. solution of 99.98% $Ca(NO_3)_2 \times 4\ H_2O$ (0.1M, 0.5 mmol) was mixed with 5 mL aq. solution of $(NH_4)_2HPO_4$ (0.06M, 0.3 mmol). To the resulting suspension, 5 mL of an aqueous solution of propionamide (1M, 5 mmol) was added. The pH was adjusted to 3 by addition of approx. 45 µL aq. HNO_3 (5 M), to give a clear, transparent solution. The solution was transferred to a PTFE-lined microwave digestion vessel and treated hydrothermally (heating ramp: 30°C/min, final temperature 180°C for 30 min), using a Milestone EthosEZ Microwave Digestion System (Milestone, Shelton, CT). The resulting precipitate was centrifuged and washed with deionized water (3×15mL) and ethanol (3×15mL), and dried in vacuo.

OHAp (0.22 at% Mg) was synthesized as described above, but using 99% $Ca(NO_3)_2 \times 4\ H_2O$ instead of 99.98% $Ca(NO_3)_2 \times 4\ H_2O$.

OHAp (1.15 at% Mg): To 475 µL of an aq. solution of 99.98% $Ca(NO_3)_2 \times 4\ H_2O$ (1M, 0.475 mmol, was added 25 µL of an aq. solution of $Mg(NO_3)_2 \times 6\ H_2O$ (1M, 0.025mmol). The solution was diluted to 5 mL overall volume with DI water. A 5 mL aq. solution of $(NH_4)_2HPO_4$ (0.06M, 0.3 mmol) solution and 5 mL of an aqueous solution of propionamide (1M, 5 mmol) were added to give a suspension. The pH was adjusted to 3 by addition of approx. 45 µL aq. HNO_3 (5 M) to give a clear, transparent solution. The solution was transferred to a PTFE-lined microwave digestion vessel and treated hydrothermally as described above. The resulting precipitate was centrifuged and washed with deionized water (3×15mL) and ethanol (3×15mL), and dried *in*

vacuo to give OHAp (approx. 20 wt% by PXRD) and whitlockite (approx. 80 wt% by PXRD). Needle-shaped OHAp crystals could easily be differentiated from whitlockite platelets.

Phase identify and purity for all samples was confirmed by PXRD. The magnesium mole fraction was determined using ICP-MS.

2.4.10 POWDER X-RAY DIFFRACTION (PXRD)

PXRD patterns of OHAp were collected at 100 K on a STOE-STADI-P powder diffractometer (STOE Corporation, Chicago, IL) equipped with an asymmetric curved Germanium monochromator (CuKα1 radiation, $\lambda = 1.54056$ Å) and one-dimensional silicon strip detector (MYTHEN2 1K, DECTRIS Ltd., Philadelphia, PA). The line-focused Cu X-ray tube was operated at 40 kV and 40 mA. Powder was packed in a polyimide capillary (0.5 mm inner diameter) and intensity data were collected over an angular range of $2\theta = 10 - 70°$, over a period of 10 mins. Instrument was calibrated against a NIST Silicon standard (640d). Data was processed and Rietveld refinement was performed using MDI Jade 2010 (Materials Data, Inc., Livermore, CA). Lattice parameters are reported in **Table 2.6**.

2.4.11 SINGLE CRYSTAL X-RAY DIFFRACTION

Diffraction data for OHAp (0.22 at% Mg) and OHAp (1.15 at% Mg) were collected at a set temperature of 100 K using a Bruker Kappa APEX2 diffractometer (Bruker AXS, Madison, WI) equipped with a Mo Kα (λ = 0.71073 Å) source. Single crystals (50 µm×5 µm×5 µm) were picked from powders and mounted with Paratone N on a cryo-loop. Diffraction patterns were indexed, refined, and integrated using SAINT of the APEX2 package (Bruker AXS). Using

Olex2,[102] the structure was solved with XT and refined with the ShelXL package using least squares minimization.[103] Lattice parameters are reported in **Table 2.6** and **Figure 2.9**.

2.4.12 INDUCTIVELY COUPLED PLASMA MASS SPECTROMETRY (ICP-MS)

ICP-MS was carried out on a Thermo iCAP Q ICP-MS (Thermo Fisher Scientific, Inc.; Waltham, MA). For phase-pure samples, powders were used as is. For the sample containing whitlockite, the single crystal that was analyzed by X-ray diffraction was used. Samples were dissolved in trace metal-grade HNO_3 solution (0.1 M) in a metal-free tube. Trace metal-grade HCl solution was used as a blank.

2.4.13 DENSITY FUNCTIONAL THEORY (DFT) CALCULATIONS

DFT calculations were performed within the generalized gradient approximation using the Perdew-Burke-Ernzerhof revised for solids (GGA-PBEsol) exchange-correlation functional[104] with the planewave pseudopotential code, Quantum ESPRESSO[105]. We used the ultrasoft pseudopotentials[106] taken from the PSLibrary[107]. A plane-wave cutoff of 60 Rydberg was used during the ionic and electronic relaxation steps. For the simulation of Mg-doped OHAp solid solutions, we employed a $2\times2\times1$ supercell (with 352 atoms) in the monoclinic crystal structure ($P2_1/c$ symmetry). Our initial simulation performed on a pristine $Ca_{10}(PO_4)_6(OH)_2$ supercell serves as the reference. Additional simulations were performed, whereby 1, 2, 3, and 4 Ca atoms were substituted with Mg atoms. The atomic positions and the cell volume were relaxed until the Hellmann-Feynman forces were less than 2 meV Å^{-1} and components of the stress tensor were less than 0.1 kbar. The Brillouin zone integration was performed using a $1\times1\times1$ Monkhorst-Pack k-point mesh (Γ-point calculation). Lattice parameters as calculated (at 0 K) and corrected to 298

K using the coefficient of thermal expansion reported by Babushkin and coworkers[69] are reported in **Figure 2.9**.

2.4.14 LATTICE STRAIN AS A FUNCTION OF COMPOSITION

Lattice parameters as a function of magnesium mole fraction were determined by XRD and DFT as outlined above (**Figure 2.9**). Lattice parameters as a function of carbonate weight fraction were obtained from Demier and coworkers.[70] using WebPlotDigitizer.[108] Carbonate weight fractions were converted to mole fractions (X_C) using the stoichiometric models postulated by Deymier and coworkers.[70] The concentration dependent lattice strain in the a- and c-direction was calculated from the lattice parameters and fitted with a linear model,

$$\varepsilon_i{}^j = n_i{}^j X_j + b_i{}^j$$

, where $\varepsilon_i{}^j$ denotes the strain in the i-direction due to substitution with species j, X_j is the mole fraction of species j, $n_i{}^j$ is the slope, and $b_i{}^j$ is the intercept (Error! Reference source not found.). Fit parameters are reported in **Table 2.7**.

2.4.15 FINITE ELEMENT MODELING

Enamel crystallites were idealized as slabs with rectangular cross section, oriented with the [001] direction parallel to the z-axis and the [100] parallel to the x-axis. Mg and carbonate concentrations were modeled as continuous, 2-dimensional distributions, chosen to represent experimental 1D concentrations profiles in the x-direction (**Figure 2.8**). For simplicity, the contributions of fluoride and of sodium ions in excess of those needed to charge balance carbonate ions were ignored, as were contributions from surface free energies. All modelling was performed using COMSOL Multiphysics® (COMSOL, Burlington, MA).

3.   MULTI-HIT ANALYSIS

The work from this chapter, including figures, has been reproduced, with or without modifications, from the following publication in preparation: K. A. DeRocher, L. M. Gordon, D. Joester, "Analysis of molecular ions in atom probe tomography of apatites." *in preparation*

3.1   INTRODUCTION

Recent advances in atom probe instrumentation, specifically the implementation of the UV laser, have allowed for the characterization of non-metallic specimens. However, little is known about the physical mechanisms of field evaporation for dielectrics. Most field evaporation theories for metals assume that only the atoms on or near the tip surface are affected by the electric field. In semiconducting and insulating materials, however, the effects of a high electric field extend many atomic layers into the bulk of the material, so the electronic structure of these materials is significantly different from those of metals, adding complexity to the process of field evaporation.[22] Preliminary work investigating field evaporation of insulating materials suggests that placing an insulator in a high electric field reduces the electric field to almost zero inside the tip itself.[6] In this way, the tip is thought to behave like a metal in the presence of a high electric field.

An area of recent interest in materials science and biomedical fields is the analysis of the structure and phase composition of bone, dentin, and enamel, and of implants interfacing with these materials.[10,25,28-30] These biomaterials contain a high fraction of hydroxylapatite (OHAp). OHAp is one of the endmembers of the apatite group of minerals that have the general chemical formula $Ca_5(PO_4)_3(X)$, where X = OH, Cl, or F, among others (**Figure 1.4**).

Atom probe tomography spectra of apatites show that field evaporation results in a significant number of molecular ions. Such molecular ions can be difficult to identify unambiguously, and the presence of molecular ions reduces the spatial resolution of APT reconstructions. There is a need to understand the formation and behavior of such molecular ions better. An elegant way to gain some insight into the identity and stability of molecular ions makes use of the analysis of 'multi-hit detector events'.

Multi-hit events are events in which several ions arrive at the detector within a very short amount of time. A small fraction of multi-hits results from the decay of molecular ions into two or more fragments. If both fragments are charged, they are termed daughter ions, but it is also possible for one of the fragments to be charge neutral (shown schematically in **Figure 3.1**). In our experience, multi-hits can account for the majority of detector events, e.g. 66% in calcium carbonate or 55% in geological cuprite. In synthetic apatites, the fraction of total events that are multi-hits is lower, but still substantial (~20%).
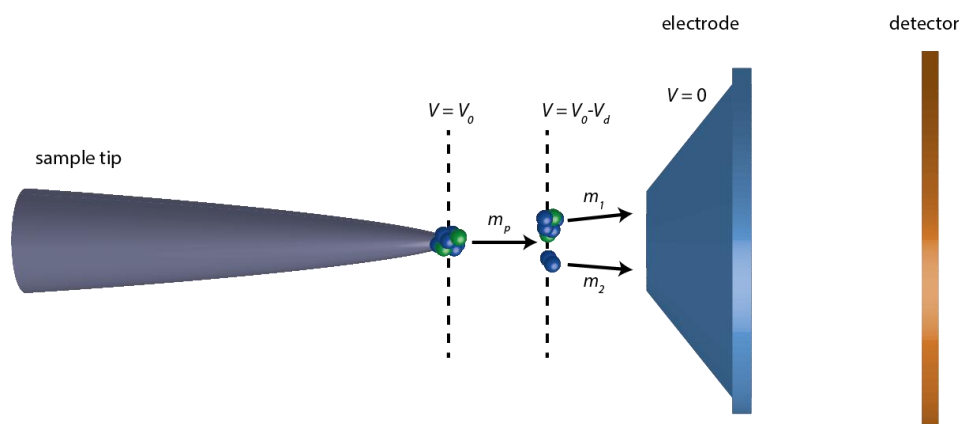
Figure 3.1. Schematic of a multihit.
A relatively large ion cluster evaporates from the sample tip, but then breaks apart into two smaller daughter ions before hitting the detector.

We present herein an analysis of molecular ions and dissociation events that result in two daughter fragments in apatites. We hope that this analysis will help others interpret spectra of apatite-containing biological, geological, and synthetic samples, and will contribute to the understanding of field evaporation events in such materials. Ultimately, this data may be used to benchmark simulations of field evaporation processes.

3.2   RESULTS AND DISCUSSION

3.2.1   CORRELATION HISTOGRAM

We analyzed detector events with multiplicity 2 (dual hits) by constructing 2D correlation histograms.[109] Such histograms record the frequency of dual hit events as a function of the apparent mass-to-charge-state ratio (m/z) of the two particles detected. When a parent ion decays into two daughter fragments with unequal m/z during the acceleration period, the time of flight of the daughter ions, and by extension their apparent m/z is affected. This affect can be described by a simple model (**Eq. 3.1**),

$$m_i' = m_i \left[1 - \frac{V_d}{V_o} \left(1 - \frac{m_i}{m_p} \right) \right]^{-1} \quad (\textbf{Eq. 3. 1})$$

where m_i' is the apparent m/z of the ith daughter ion, m_i is its actual m/z, m_p is the m/z of the parent ion, and the potential drop $\frac{V_d}{V_o}$ is the ratio of the electric potential at which dissociation occurs over the total accelerating potential difference.[109]

Over the course of an APT experiment, many parent ions are generated. Depending on the potential drop at which the parent ion dissociates, **Eq. 3.1** predicts that for each pair of daughter

ions, the point (m'_1, m'_2) lies along a dissociation track. When dissociation happens near the tip, $\frac{V_d}{V_o}$

approaches 0, m'_1 approaches m_1 and m'_2 approaches m_2, meaning that the daughter ions behave

as if they had evaporated independent of each other. When dissociation happens late, $\frac{V_d}{V_o}$ approaches

1, both m'_1 and m'_2 approach m_p. The dissociation track is therefore an arc between the point

$(m_\mathrm{p}, m_\mathrm{p})$ on the diagonal, and the point (m_1, m_2). If the parent ion dissociates into an ion and a

neutral fragment, m'_1 of the charged fragment is described by **Eq. 3.1**. For the neutral fragment, it

can be shown that

$$m'_2 = m_\mathrm{p} \left(\frac{V_d}{V_o}\right)^{-1} \qquad (\textbf{Eq. 3.2})$$

In this case, late dissociation again results in the apparent m/z of both fragments

approaching m_p. However, in case of early dissociation, only the daughter ion will accelerate

beyond the velocity of the parent ion at the time of dissociation. As a consequence, the apparent

m/z of the neutral fragment will approach infinity. The dissociation track therefore intersects the

diagonal at $(m_\mathrm{p}, m_\mathrm{p})$ and, within the limits of the experimental TOF window, has an asymptote

at m_1 .[3]

We chose to perform an analysis of dual hits on three different apatite endmembers,

hydroxylapatite (OHAp), chlorapatite (ClAp), and fluorapatite (FAp), and compare the results to

those found in human enamel. In an earlier comparison of spectra (**Figure 3.2**), it emerged that

while the majority of ions generated in field evaporation are identical between the four samples,

there are a number of atomic and molecular ions that are specific to each apatite.[10] Briefly, clusters

in the form $P_xO_y(OH)_z^+$ were detected in OHAp, but not ClAp or FAp indicating they are specific

to OH⁻ being the channel ion. In the case of ClAp, Cl appears in the spectrum as Cl^+ and ClO^+, but does not appear to form ion clusters with phosphorous. In comparison, F in FAp appears most commonly as CaF^+, but also frequently evaporates off the sample tip as $P_xO_yF_z^+$ clusters. The spectrum for human enamel, nominally composed of OHAp, also contains peaks specific to fluorapatite and chlorapatite, indicating that these elements are present as impurities in enamel.
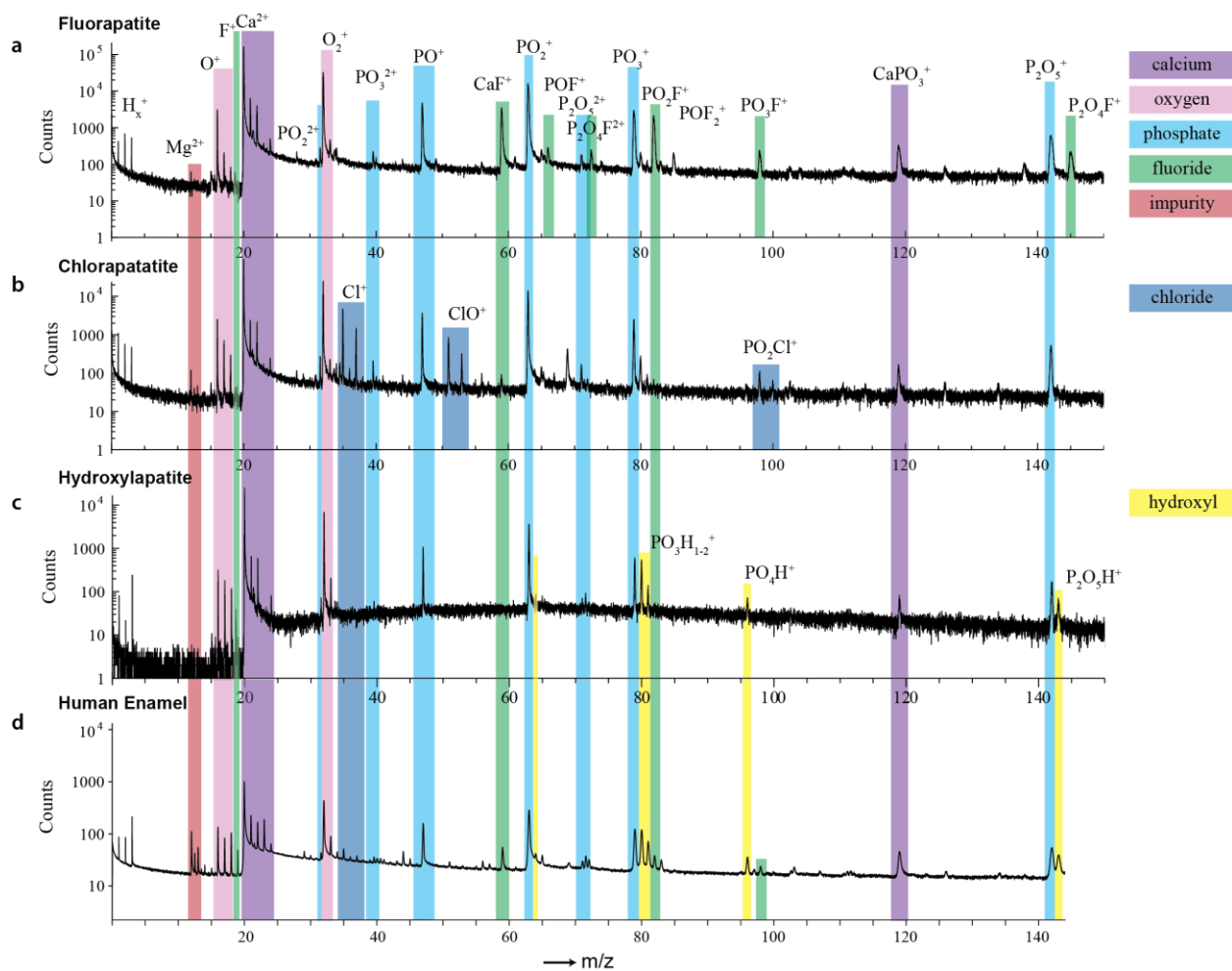
Figure 3.2. APT spectra of apitites.
Synthetic (**a**) fluorapatite, (**b**) chlorapatite, and (**c**) hydroxyapatite (adapted from [10]) and human enamel (adapted from [30]). Data presented in **a-c** collected and plotted by Lyle Gordon.

In order to better understand differences in the ionic clusters generated by these materials, correlation histograms for OHAp, ClAp, FAp, and human enamel (**Figure 3.3a-d**) were constructed. Note that histograms were constructed by calculating the frequency of the couples (m_1, m_2), where $m_1 \leq m_2$, and then mirroring across the diagonal. A total of 38 dissociation tracks were identified by their characteristic arc shape. Based on the endpoints of the tracks, we identified m_p, m_1, and m_2, and thereby the associated dissociation reactions (**Table *3.1***). We find that there are only 32 unique parent ions, meaning that several of these parent ions have several decay pathways. While many of the dissociation reactions are common to all the analyzed apatites, there were two specific to OHAp (tracks 9c and 10), two specific to ClAp (tracks 14 and 15), eight specific to FAp (tracks 16-23), and five specific to human enamel (tracks 28-31). Most parent ions conform to the general formula $P_nO_mX^{2+}$, where n=1...6 and m/n = 1.5 … 3.
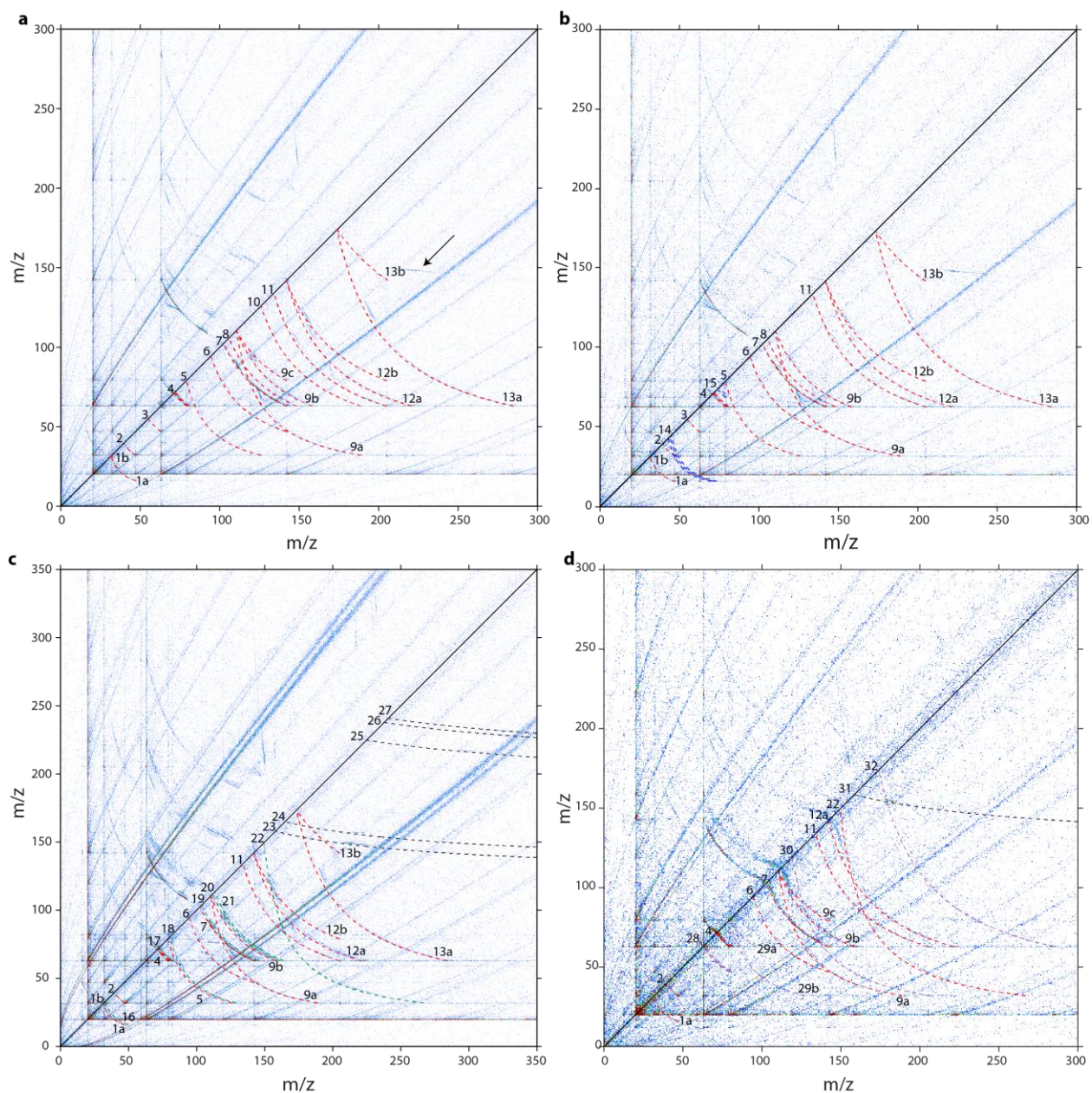
Figure 3.3. Correlation histograms.
OHAp (**a**), ClAp (**b**), FAp (**c**), and human enamel (**d**) with identified tracks found in multiple apatites shown with a red dashed line and tracks specific to each apatite shown with a different color dashed line (ClAp – blue, FAp - green, human enamel – purple), and tracks with a neutral daughter cluster shown with a black dashed line.

Table 3.1. Parent ions and dissociation products observed in hydroxylapatite, chlorapatite, fluorapatite, and human enamel.

track	parent ion	m/z	daughter 1	m/z	daughter 2	m/z
1a	PO_2^{2+}	31.5	PO^+	47	O^+	16
1b	PO_2^{2+}	31.5	$*P^+$	31	O_2^+	32
2	PO_3^{2+}	39.5	PO^+	47	O_2^+	32
3	$*P_2O_3^{2+}$	55	PO_2^+	63	PO^+	47
4	$P_2O_5H_x^{2+}$	71+(x/2)	$PO_3H_x^+$	79+x	PO_2^+	63
5	$**P_2O_6^{2+}$	79	$P_2O_4^+$	126	O_2^+	32
6	$P_3O_6^{2+}$	64.5	$P_2O_5^+$	142	PO^+	47
7	$P_3O_7^{2+}$	102.5	$P_2O_5^+$	142	PO_2^+	63
8	$P_3O_7H_6^{2+}$	105.5	$P_2O_5H_6^+$	148	PO_2^+	63
9a	$P_3O_8^{2+}$	110.5	$*P_3O_6^+$	189	O_2^+	32
9b	$P_3O_8^{2+}$	110.5	$P_2O_6^+$	158	PO_2^+	63
$^\alpha$9c	$P_3O_8^{2+}$	110.5	$P_2O_5^+$	142	PO_3^+	79
$^\alpha$10	$P_4O_8^{2+}$	126	$P_3O_6^+$	189	PO_2^+	63
11	$P_4O_9^{2+}$	134	$P_3O_7^+$	205	PO_2^+	63
12a	$**P_4O_{10}^{2+}$	142	$P_3O_8^+$	221	PO_2^+	63
12b	$**P_4O_{10}^{2+}$	142	$P_3O_7^+$	205	PO_3^+	79
13a	$P_5O_{12}^{2+}$	174	$P_4O_{10}^+$	285	PO_2^+	63
13b	$P_5O_{12}^{2+}$	174	$P_3O_7^+$	205	$P_2O_5^+$	142
$^\beta$14	$*Cl_2O^{2+}$	43	$*Cl_2^+$	70	O^+	16
$^\beta$15	$*PO_5H_2Cl^{2+}$	74	PO_3^+	79	$*H_2O_2Cl^+$	69
$^\gamma$16	POF^{2+}	33	$*PF^+$	50	O^+	16
$^\gamma$17	$P_2O_4F^{2+}$	72.5	PO_2F^+	82	PO_2^+	63
$^\gamma$18	$P_2O_5F^{2+}$	80.5	$*P_2O_3F^+$	129	O_2^+	32
$^\gamma$19	$P_3O_6F^{2+}$	104	$P_2O_4F^+$	145	PO_2^+	63
$^\gamma$20	$P_3O_7F^{2+}$	112	$P_2O_5F^+$	161	PO_2^+	63
$^\gamma$21	$P_3O_6F_2^{2+}$	113.5	$P_2O_4F_2^+$	164	PO_2^+	63
$^{\gamma,\varepsilon}$22	$P_5O_9^{2+}$	149.5	$P_5O_7^+$	267	O_2^+	32
$^\delta$23	$P_4O_{12}^{2+}$	158	$P_4O_{10}^{2+}$	142	O_2	∞
$^\delta$24	$P_6O_9^{2+}$	165	$P_6O_7^{2+}$	149	O_2	∞
$^\delta$25	$CaP_6O_{14}^{2+}$	225	$CaP_6O_{12}^{2+}$	209	O_2	∞
$^\delta$26	$Ca_2P_2O_6^{2+}$	238	$Ca_2P_2O_4^{2+}$	222	O_2	∞
$^\delta$27	$CaP_6O_{16}^{2+}$	241	$CaP_6O_{14}^{2+}$	225	O_2	∞
$^\varepsilon$28	$P_2O_4H_x^{2+}$	63+(x/2)	$PO_3H_x^+$	79+x	PO^+	47
$^\varepsilon$29a	$P_2O_6H^{2+}$	79.5	PO_4H^+	96	PO_2^+	63
$^\varepsilon$29b	$P_2O_6H^{2+}$	79.5	$P_2O_4H^+$	127	O_2^+	32
$^\varepsilon$30	$P_3O_9H_2^{2+}$	119.5	$P_3O_7H_2^+$	207	O_2^+	32
$^\delta$31	$P_4O_{12}H^{2+}$	127.5	$P_4O_{10}H^{2+}$	143	O_2	∞
$^\varepsilon$32	$P_4O_{14}^{2+}$	174	$P_3O_{12}^+$	285	PO_2^+	63

*not seen in single hit spectrum; **may overlap with other peaks; $^\alpha$OHAp specific; $^\beta$ClAp specific; $^\gamma$FAp specific; $^\varepsilon$Enamel specific; $^\delta$contains neutral daughter ion

Three parent ions, $P_2O_3^{2+}$, Cl_2O^{2+}, and $PO_5H_2Cl^{2+}$, did not appear in single hit spectra, indicating that their lifetime is shorter than the duration of the acceleration phase. Possible explanations for this instability will be discussed in subsequent sections. For two other ions, $P_2O_6^{2+}$ and $P_4O_{10}^{2+}$, the original peak assignment postulated the formation of the singly charged 'monomers', i.e. PO_3^+ and $P_2O_5^+$, rather than the doubly charged dimers $(PO_3)_2^{2+}$ and $(P_2O_5)_2^{2+}$.

However, we are unable to decompose the original peak in order to determine relative amounts of monomers and dimers. This limitation arises because there is no way to tell which hits at a particular *m/z* come from a cluster with a particular mass and a charge, and which hits come from a cluster with exactly twice the mass and twice the charge.

The majority of dissociation reactions results in the loss of O^+, O_2^+, or PO_n^+, where n = 1-3, from larger clusters (**Figure 3.4**). The dissociations specific to human enamel and FAp appear to be P_nO_m clusters found (either as parents or daughters) in all the analyzed apatites, with additional channel ion groups (OH in enamel and F in FAp). ClAp, on the other hand, did not have nearly as many unique dissociations. While one dissociation was consistent with Cl added to a P_nO_m cluster found in the other apatites, the other was Cl_2O^{2+} decomposing into its (singly charged) constituent elements.
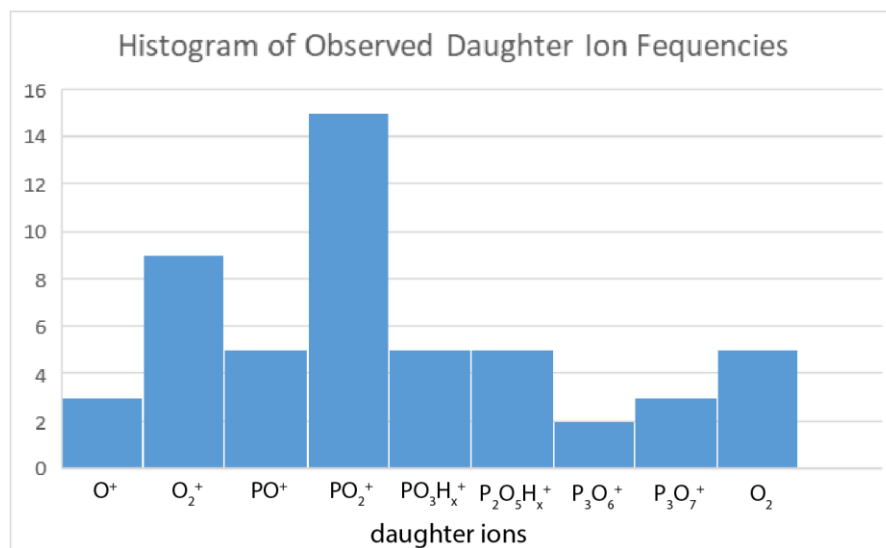
Figure 3.4. Histogram of observed daughter ion.
Those that only occurred once were not plotted.

Loss of P^+ is only observed in one case. Loss of O^+ and P^+ from $P_nO_m^{2+}$ ions simply involves breaking a P-O bond. Loss of O_2^+ could occur by breaking two PO bonds and reforming an O-O bond at the same time. Alternatively, if the parent ion contains a linear P-O-O chain, O^+ could form by breaking an O-O bond, and O_2^+ could form by breaking a PO bond. If we also consider the possibility of parent ions with small ring structures, concerted or step wise reactions may lead to the observed fragments as well. Note that any parent ions that contain O-O bonds, P-O-P bonds, or rings cannot form simply by breaking bonds in the apatite lattice. They must therefore form on the surface of the tip, or by rearrangement of the parent ion after field evaporation. Formation of parent ions with a given number of phosphorous atoms at the surface of the tip would require forming as many P-O (or, less likely, P-P) bonds as there are phosphorous atoms.

3.2.2   FORMATION OF NEUTRAL FRAGMENTS

We identified 6 tracks that are consistent with the dissociation of a parent ion into a charged daughter and a neutral daughter. In all cases, the neutral daughter was O_2. Tracks 23-27, as well as Track 31 (**Figure 3.3c,d**), show the behavior described in the previous section, with the track asymptotically approaching the m/z of the charged daughter. Evidence that neutral fragments can form in the atom probe has been shown in other materials like GaN ($GaN_3^{2+} \rightarrow Ga^+ + N^+ + N_2$) and LiFePO$_4$ ($PO_4^+ \rightarrow PO_2^+ + O_2$), and may explain some slight compositional inaccuracies.[109-110]

3.2.3   TIME-DEPENDENCY OF DISSOCIATIONS

Inspection of dissociation tracks further reveals that the frequency of fragmentation is not uniform along the arc (see arrow in **Figure 3.3a**). This variation leads us to question why molecular ions decay. One might assume that field evaporation results in highly energetic "hot" ions that decay over time as some energy is lost by the ions rotating in the field. We would then expect that ions would preferentially dissociate early in the flight, as they have the most energy at that point, and that the likelihood of dissociation would decrease exponentially from there. However, this trend is not observed; for many tracks, the dissociation behavior appeared to be dependent on the fractional potential drop (related to position on the atom probe chamber).

Using the method described previously, we plotted the deviation of the experimental track from the simulated track (calculated using **Eq. 3.1**) as a function of the fractional potential drop. With the simulated track appearing horizontal in this type of plot, any deviation of the experimental data from horizontal indicates that the daughter ions hit the detector with a different *m/z* than

predicted by **Eq 3.1**. **Figure 3.5** shows "straightened" Track 1A, and after looking at all of the tracks, the following observations were made. First, dissociation events are not distributed evenly throughout the flight time, with an apparent preferential dissociation window occurring at $V_d/V_o \cong$ 0.75. Second, it was generally observed that dissociations occurring further from the sample tip $(V_d/V_o \rightarrow 1)$ deviated more drastically from the simulated track. Generally, the deviation was in the positive direction (upward on the graph), meaning that daughter ions in the experimental data had higher *m/z* than **Eq. 3.1** suggests. Differences between the experimental and theoretical results may arise from the fact that **Eq. 3.1** was derived under the assumption that all of the energy imparted by the electrical field is used to accelerate the ions from the tip to the detector. However, it has been suggested that some of the field energy may also contribute to rotation of the ions, which would mean that they would be detected as a species with slightly higher m/z (as their flight takes longer than if they were not rotating).
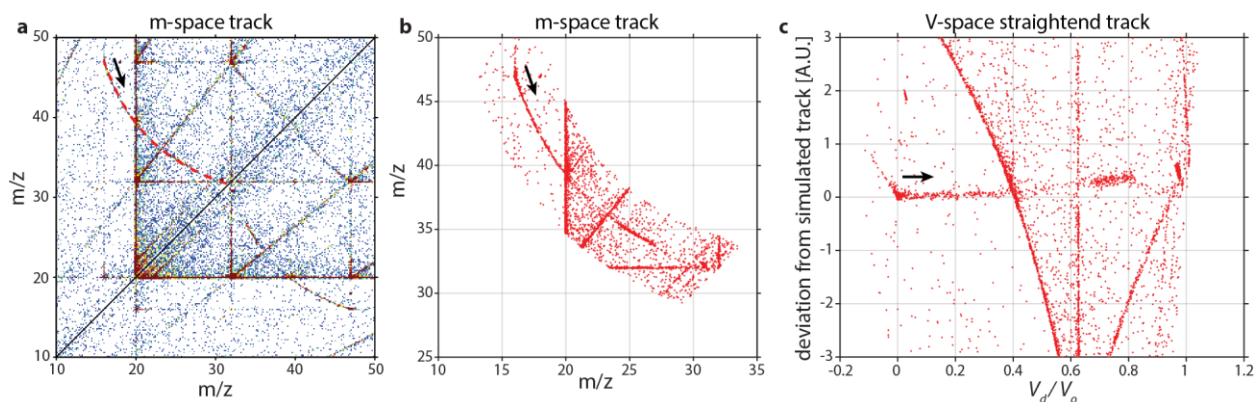
Figure 3.5. Example of straightened track.

(**a**) Track 1a from correlation histogram ($PO_2^{2+} \rightarrow PO^+ + O^+$). Points near the simulated track (**b**) selected and plotted as a function of fractional potential drop (V_d/V_0) (**c**). Arrow indicates direction of increasing fractional potential drop.

In order to probe the seemingly preferred dissociation at $V_d/V_o \cong 0.75$, we used the Comsol software package to perform an electrostatic simulation of the sample tip and the ring electrode. By setting the electric bias difference between the sample tip and the electrodes to 5 kV, we could then visualize the field strength as a function of position in the simulated atom probe chamber. A contour plot of the field strength was then plotted, and compared to the range of fractional potential drops where we saw preferred dissociation (around $V_d/V_o = 0.67$ to 0.82) This range over which parent ions tend to dissociate (outlined in black in **Figure 3.6**), is consistent with the location where the cluster of atoms would pass through the electrode. Therefor there may be some sort of perturbation in the electric field, or other effects associated with the electrode that increases the likelihood of large ion clusters breaking apart.
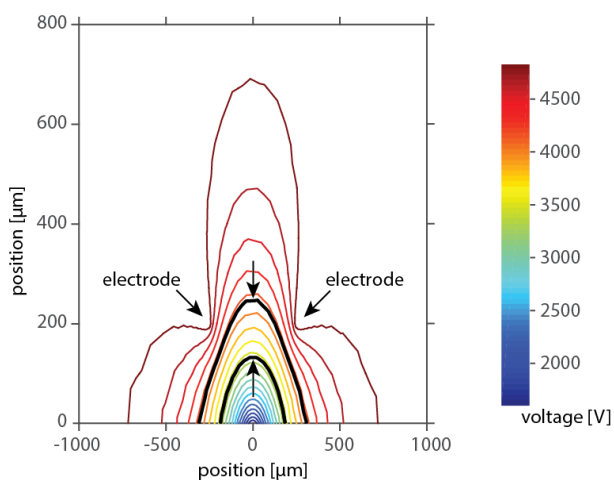
Figure 3.6. **Contour plot of voltage in a 2D simulation of the atom probe chamber.**

3.3 CONCLUSIONS

Our analysis of multihits in APT analysis of different apatites reveals that there is evidence for ion mobility on the sample tip. The generation of large P_nO_m clusters with no bridging calcium clusters suggests these ions diffuse over the surface and bond before evaporating off the tip. Additionally, we see a preferential dissociation window around $V_d/V_o \cong 75$. This trend may be due to a feature in the atom probe chamber (possibly the electrode) or it may represent an energy barrier that must be overcome in order for dissociation to occur. Another important observation is the presence of parent clusters like $P_2O_6^{2+}$ and $P_4O_{10}^{2+}$ that may contribute to peaks assigned as PO_3^+ and $P_2O_5^+$ in the mass spectrum. This phenomenon may lead to inaccuracies in the reported composition as larger, doubly charged clusters are given the identity of a cluster half the size.

3.4 MATERIALS AND METHODS

Synthetic hydroxylapatite (OHAp), chlorapatite (ClAp), and fluorapatite (FAp) were analyzed using a CAMECA local-electrode atom probe (LEAP 4000XSi) under the run conditions described in **Table 3.2**. Human enamel sample was analyzed using the LEAP 5000XS (CAMECA Instruments).

Table 3.2. Details about the hits collected and run parameters for data sets.

	RHIT	#single	#multi	#partial	Total	T (K)	Frequency (kHz)	Laser Power (pJ)
OHAp	R06_14495	8,292,794	1,741011	58,209	10,092,014	66	250	150
ClAp	R06_15232	2,094,130	565,091	11,640	2,670,861	41	200	150
FAp	R06_15617	6,312,641	1,680,988	31,461	8,025,090	35	200	150
Human Enamel	R5079_165799	21,266,637	6,191,730	352,510	28,810,877	25	333	40

After obtaining the APT data, a 2D correlation histogram was constructed, and tracks in the experimental data were compared to theoretical tracks calculated using **Eq. 3.1**. The possible dissociations were narrowed down using knowledge of the apatite structure. For example, in a

P_nO_m cluster, $n - 1 \leq m \leq 3n + 1$. Clusters that had a n:m ratio outside this range were therefore not considered. The existence of enough available Ca and H sites also allowed us to narrow the possible parent and daughter cluster identities to a more manageable number.

Ideally each track is complete, making identification relatively straightforward. However, in many cases, only a portion of the track is visible, making identification more difficult. In such instances, depending on what portion of the track could be seen, the approximate m/z of the parent or daughters could be estimated. After comparison with simulated tracks, and elimination of ion clusters not chemically allowed, typically only one or two possibilities remained, so an assignment could be made.

In order to investigate the dissociation behavior relative to position in the atom probe chamber, as well as the difference between experimental and simulated results, we also plotted the data with fractional potential drop on the x-axis and distance from the simulated track on the y-axis. First, the shortest distance between each data point and the simulated track was calculated. The fractional potential drop of that point could then be found in the original data file and plotted versus that point's distance from the simulated track. In order to save computational time, only points relatively near the theoretical dissociation track were considered (**Figure 3.5b**). Tracks plotted using **Eq. 3.1** will appear horizontal in this plot, so when the experimental data deviates from horizontal, that is indicative of daughter ion pairs arriving at the detector with different mass to charge state ratios than **Eq. 3.1** suggests.

4. MAPPING HUMAN ENAMEL CRYSTALLITE ORIENTATION WITH SYNCHROTRON X-RAY DIFFRACTION

The work from this chapter, including figures, has been reproduced from the following publication: R. Free, K. A. DeRocher, R. Xu, D. Joester, S. R. Stock, "Mapping Sub-micron Scale Crystallographic Variation in Human Tooth Enamel via Synchrotron X-ray Diffraction, *in preparation.*

4.1 INTRODUCTION

As described in detail in Chapter 2, human enamel has a multi-scale hierarchical structure that makes it both hard and tough enough to endure the mechanically and chemically demanding environment of the oral cavity. Compositionally, mature enamel consists of 95% hydroxyapatite (OHAp), ~1% water, and 4% residual biomacromolecules by weight. The mineral phase exists primarily as high aspect ratio crystallites extended along their crystallographic c-axis with approximately 20 nm x 40 nm rhombohedral cross-sections in the basal plane. At the micrometer scale, a tessellating pattern of parallel 'enamel rods' with keyhole-shaped cross-sections runs from the dentino-enamel junction (DEJ) to the external enamel surface (EES) of the tooth (**Figure 4.1**).[8] Each enamel rod contains ~10^4 roughly aligned OHAp crystallites. At the center of the rod ('head'), the crystallites' c-axes are parallel to the long axis of the rod (**Figure 4.1b, white**

arrows); toward the rod boundaries and in the rod 'tail,' the c-axes rotate significantly and take a wider range of orientations.[111-112] These boundary regions are termed 'interrod' enamel, and while they are also primarily composed of OHAp crystallites, their density and crystallographic order is comparatively lower than in the rod centers.[8]

Many aspects of this structure have been extensively characterized by a combination of optical microscopy, electron microscopy, and x-ray diffraction. The general dimensions of the rod cross-sections and packing have been observed optically in enamel sections in which the interrod regions have been preferentially etched.[113] Furthermore, polarized light microscopy of thin enamel sections has revealed the divergence of the c-axes towards the rod boundaries.[112] The approximate dimensions of both the rod and crystallite cross-sections can be determined through scanning electron microscopy (SEM) [113-115] and transmission electron microscopy (TEM).[116-117] X-ray diffraction has been used to establish the crystalline phase of enamel, extract lattice parameters, map bulk crystallographic orientation and approximate crystalline domain size.[118-123] These and many other studies establish the current model of human enamel (**Figure 4.1**).

While the literature characterizing enamel's ultrastructure is vast, existing studies face limitations that have prevented a definitive characterization of crystallite populations at the sub-rod length scale. Individual crystallite dimensions can be measured with great accuracy using TEM, and crystallographic orientation can be determined on the same crystallites, but TEM studies suffer from a limited field of view that makes the extraction of population-level statistics impractical. Lower resolution techniques, such as optical microscopy and SEM, can image a large area containing numerous enamel rods, but generally require acid etching that disturbs the natural state of the enamel and introduces topography that confounds precise measurements of crystallite

dimensions and orientations. X-ray diffraction has the potential to provide population-scale sampling without significantly disturbing enamel's natural state, but in all existing studies, the scale of the X-ray probe has resulted in measurements that average over multiple enamel rods and include interrod regions, eliminating the ability to resolve differences across or between individual rods. Because of these challenges, there is currently no clear picture of sub-rod length-scale variation of crystallite populations' dimensions and crystallographic characteristics, i.e. lattice parameters, crystallographic orientations distribution, coherent domain size, micro-strain, etc.

Here, we introduce a synchrotron microdiffraction approach through which these challenges can be overcome, taking advantage of the strengths of X-ray diffraction (high sampling in a near native state) while still achieving the spatial resolution necessary to independently sample different crystallite populations across individual rods. By isolating a 1 µm thick plate of enamel and performing diffraction with a focused (~500 nm wide) monochromatic X-ray probe, crystallites from only a single rod are sampled at any one position. With lateral specimen dimensions of 18 µm x 8 µm and expected rod dimensions of approximately 5 µm x 9 µm (**Figure 4.1**), at least one whole rod cross-section is expected in the sample as well as portions from approximately six others. With lateral translational step sizes of 500 nm in both dimensions, each enamel rod can be sampled by 100-200 non-overlapping volumes each of which contains on the order of 300 crystallites.

In order to compare measured quantities from rod and interrod populations of crystallites, it is first necessary to identify the boundaries between rods. We chose to do this directly from the X-ray diffraction patterns themselves. Prior work has shown that the crystallographic *c*-axes of rods in the interrod volumes are much less parallel than in the rod centers.[111] This would be

reflected in transmission X-ray diffraction patterns recorded on an area detector positioned normal to the incident beam, specifically in the azimuthal distribution of intensity around diffraction rings. We herein report the development of a computational method that quantifies the azimuthal autocorrelation of diffracted intensity in specific reflections to compute a metric for crystallographic order/disorder. The use of azimuthal autocorrelation to determine regions of order and disorder in the enamel structure was previously described in detail by Free *et al.,* and is also discussed in Section 4.4.4.[124] Briefly, the crystallite orientation distribution within the irradiated volume is related to the azimuthal distribution of the intensity in the *hkl* diffraction rings. When the diffraction spots are clustered together and not uniformly distributed around the ring, this indicates crystallographic texture, or a higher degree of order. Azimuthal autocorrelation assigns a number to this degree of order, with higher values being more ordered and lower values being less ordered. The addition of these autocorrelation values for multiple reflections within a single diffraction pattern results in a value we call the combined local azimuthal autocorrelation or CLAA. When applied to a diffraction map taken through a tooth enamel specimen (18 µm x 8 µm x 1 µm dimensions), the method allows for the correlation of crystallographic quantities extracted from each pattern within the enamel microstructure, providing, for the first time, population-specific characterization of rod vs. interrod enamel.
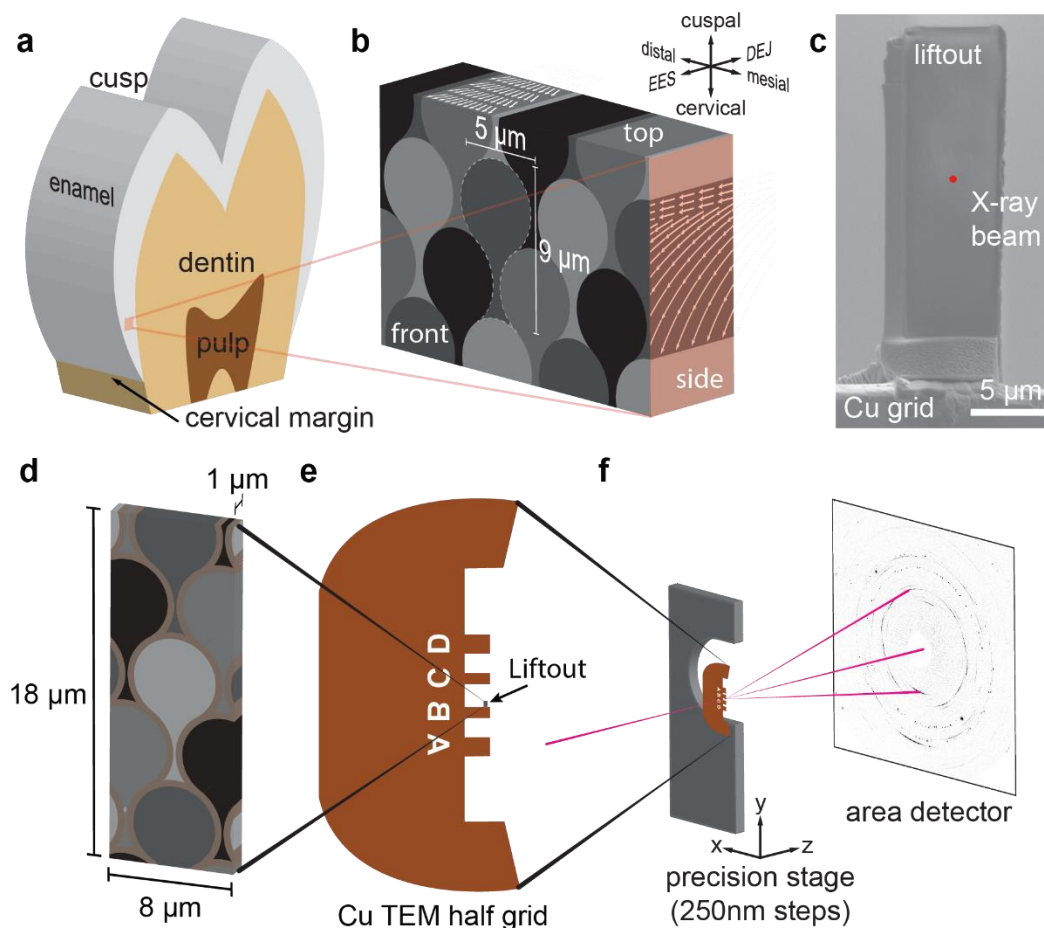
Figure 4.1. Structural schemas of human tooth enamel and experimental geometry
(**a**) Mesial-distal cross section of human pre-molar. (**b**) Isometric view of enamel microstructure adapted from [111]. Key-hole-shaped enamel rods run from DEJ to EES. Overlaid white arrows indicate the putative c-axis orientation of OHAp crystallites comprising each rod. Red highlight in panel **a** corresponds to the red face of panel **b** (orientation conserved). The 'front', 'top', and 'side' views shown on each edge of this schema correspond to the targeted orientation of the similarly named enamel sections. Interrod regions are not represented. (**c**) SEM image of enamel section after liftout and thinning. The copper TEM grid is visible (labeled) in the lower portion of the field of view, and the X-ray probe is illustrated to scale in the center of the enamel section. (**d**) Schematic of an enamel section after liftout and thinning. Keyhole pattern of enamel rods (greyscale) and interrod regions (brown) rendered approximately to scale. (**e**) Schematic of copper TEM half grid with enamel section mounted to post B. (**f**) Enamel sample positioned at the focal point of the 17 keV X-ray probe to collect 2D diffraction patterns in transmission.

4.2   RESULTS AND DISCUSSION

4.2.1   AZIMUTHAL AUTOCORRELATION

Combined local azimuthal autocorrelation (CLAA) maps for each section orientation are generated by plotting the computed CLAA value for each pattern in 2D (**Figure 4.2**). For a detailed description of this analysis, see Section 4.4.4. Examining the front section (**Figure 4.2**, **front**), key-hole shaped regions of higher CLAA values (crystallographically ordered "rod" enamel) are bordered by thinner regions of lower CLAA values (crystallographically disordered "interrod" enamel). Each pixel has a side length of 500 nm; thus, the tessellating contrast pattern has dimensions roughly 5-7µm across and 8-10µm tall. As discussed in a previous publication by this group, this contrast pattern reveals the enamel microstructure: rod head regions correspond to CLAA values greater than 5, interrod regions correspond to values less than 3, and rod tail regions show intermediate values.[124]

The top and side view section maps also show patterns of CLAA contrast (**Figure 4.2, top and side**). In the side view map, linear bands of higher and lower CLAA can be observed alternating in the cervical-cuspal direction (vertical) and inclined relative to the DEJ-EES direction (horizontal in **Figure 4.2, side**) by ~45°. The linear bands run across the entirety of the section, and the two most prominent bands of higher CLAA values are spaced by ~10µm vertically. The band of high CLAA on the left edge of the section is a result of the protective platinum layer left over from the FIB lift-out procedure and is not representative of the enamel structure. In the top view map, irregularly shaped regions of higher CLAA are surrounded by regions of lower CLAA, but the boundary contrast between high CLAA regions is much less distinct than in the front section.
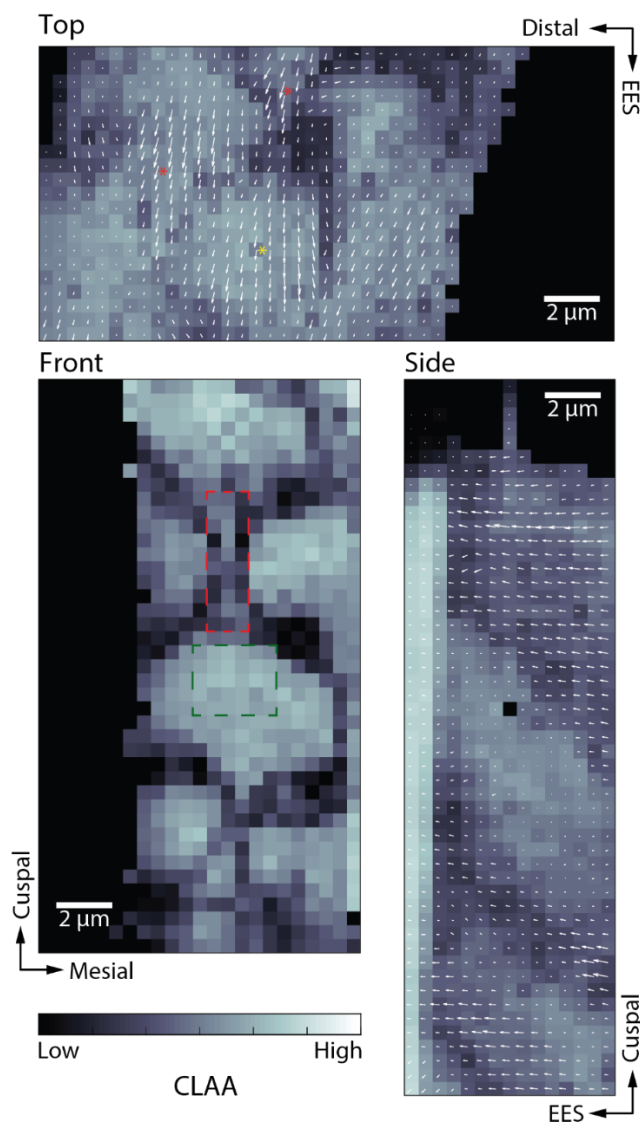
Figure 4.2. Combined local azimuthal autocorrelation (CLAA) maps for the front, top, and side views of enamel thin sections.
Higher CLAA values (lighter gray) correspond to ordered enamel (rod), while lower CLAA values (darker gray) correspond to disordered regions (interrod). The **front** section is oriented such that the X-ray beam is roughly parallel to the rod axes (and thus roughly parallel to the crystallite c-axes). The **top** view is oriented such that the rod axis runs roughly vertically in the plane of the page, while the **side** view is oriented such that the rod axis runs roughly horizontally. Overlaid on the front view are the subsampled regions for rod (green) and interrod (red) enamel. Overlaid on the **top** and **side** views are white vectors indicating the azimuthal orientation and relative intensity of the maximum of the 002 (c-axis) diffraction ring in each pattern, while the **front** section patterns display no 002 diffraction. **Top** section also has asterisks overlaid to indicate putative rod tail regions (red) where 002 intensity is high and a rod head region (yellow) where lateral precession of the 002 orientation can be seen across the rod. Axes for each section denote the approximate anatomical directions relative to the maps. Data in this image plotted by Robert Free.

4.2.2   *c*-AXIS ORIENTATION

For the side and top views, the azimuthal orientation of the maximum 002 arc intensity can also be mapped over the enamel sections (**Figure 4.2**, **top and side**). For the top view section, the c-axis orientations point generally towards the EES, but they precess slightly as one moves across regions of higher CLAA (rods), diverging away from the putative rod axis as one moves towards the interrod regions on either side. In the side view section, the *c*-axis orientation is consistent within individual bands of similar CLAA values, with slight systematic deviations as one moves across the bands. Therefore, orientational domains exist that correlate with the CLAA domains. These domains generally point in the direction of the EES, but regions of higher CLAA tend not to exhibit strong 002 diffraction (short overlaid vectors in **Figure 4.2**, **side**)

The contrast patterns observed in the CLAA maps for each of the 3 enamel views and the predominant 002 orientations in the side and top views can be interpreted relative to the current microstructural schemas for enamel (compare **Figure 4.1b** to **Figure 4.2**). The front view section displays a keyhole-shaped pattern strongly resembling enamel rods in cross-section (see schema in **Figure 4.1b**).[111] Furthermore, the cross-sectional dimensions (5-7 µm across and 8-10 µm tall) are consistent with previously reported dimensions for enamel rods in humans.[8] The absence of significant 002 diffraction in any of the patterns collected in the front view also suggests that the c-axes of the crystallites are oriented out of the plane of the pattern (i.e. closer to parallel to the incident X-ray beam), as, under the model, one would expect that the crystallite *c*-axes run mostly parallel to the enamel rod axis. Combining these observations with the fact that CLAA is a proxy metric for crystallographic order/disorder leads us to conclude that regions with higher CLAA

values (lighter gray) correspond to the more ordered rod enamel, while lower CLAA values (darker gray) correspond to the disordered interrod regions.

The CLAA maps of the top and side sections do not agree as well with expectations based on the schema for enamel microstructure (**Figure 4.1b**). For the top section, the schema suggests there should be alternating vertical bands of high (rod) and low (interrod) CLAA values; in the measured section, however, a more irregular distribution of high CLAA regions bounded by thin regions of slightly lower CLAA is observed. In the side section, the schema suggests horizontal bands of contrast that vary smoothly from rod head to rod tail in the vertical direction and discontinuously between rods. In the measured side section, the CLAA contrast variation observed is consistent with this expectation, but the bands of contrast are inclined from the horizontal by nearly 45°. Taken together, these results suggest that the true orientations of the top and side sections are rotated about the mesial-distal axis from the ideal section shown in the microstructural schema (**Figure 4.1b**) by ~45°. Because the top and side lift-outs were taken from a separate tooth, their orientation relative to the front section is less well-controlled than their orientation to one another, so this misorientation is not inexplicable.

Under this assumption, the top view section cuts obliquely across the enamel rods, and the CLAA contrast observed results from imaging across a collection of rod heads and tails. This interpretation is further supported by comparing the intensity of the predominant 002 diffraction seen in the top section (**Figure 4.2 top, vectors**) with the expected variation in c-axis orientation moving from the rod head to tail. Current models suggest that the crystallite c-axes diverge cervically from the rod axis as one moves from the head to the tail in each rod and precess slightly about the cuspal-cervical axis moving laterally across the rod cross section (**Figure 4.1b**).[111] The

002 orientations in the top section generally point towards the EES (downward in **Figure 4.2 top**), but the intensity varies across the enamel rods in the vertical direction, appearing highest in the putative tail regions of the rods (**Figure 4.2 top, red asterisks**). This is the same pattern one would expect for a section that cuts obliquely across the enamel rods: the c-axes in the rod head are oriented mostly out of the plane of the section and display weak 002 diffraction, but as they diverge cervically moving towards the tail region, they fall more readily into an orientation to diffract. There is also evidence to support the lateral precession of the c-axes in the head regions where 002 diffraction is observable (**Figure 4.2 top, yellow asterisk**).

In the side section, the rod heads do not appear oriented to diffract, as the 002 signal is not oriented along the putative rod access based on the CLAA contrast bands. On the other hand, the tail region, characterized by low CLAA values, has relatively strong 002 diffraction in an orientation that makes sense relative to the expected microstructure. One possible explanation for this phenomenon is that the head region contained within the sample was at the edge of the head, near the interrod region, with crystallite orientations rotating distally. This positioning may be significant enough to move the 002 plane out the diffracting condition. However, more analysis will need to be performed to determine if there is a section orientation that allows for this pattern, while still cutting through a tail region with crystallite orientations consistent with **Figure 4.2 side.**

4.2.3   CRYSTALLOGRAPHIC PARAMETERS

Crystallographic parameters (e.g. lattice parameters and crystallite dimensions) extracted from each pattern can be compared to reveal how these values correlate with crystallographic order/disorder (CLAA) in the 2D map of the front section (**Figure 4.3**). Crystallite size (as characterized by Scherrer analysis of the 030 and 121 diffraction peaks) tends to be slightly larger

in regions of low CLAA (compare **Figure 4.3a,b,c**). The *a* lattice parameter tends to be slightly

larger in low CLAA regions, while the *c* lattice parameter is smaller (**Figure 4.3e,f**). This

combination results in a smaller unit cell volume within low CLAA regions (**Figure 4.3d**).
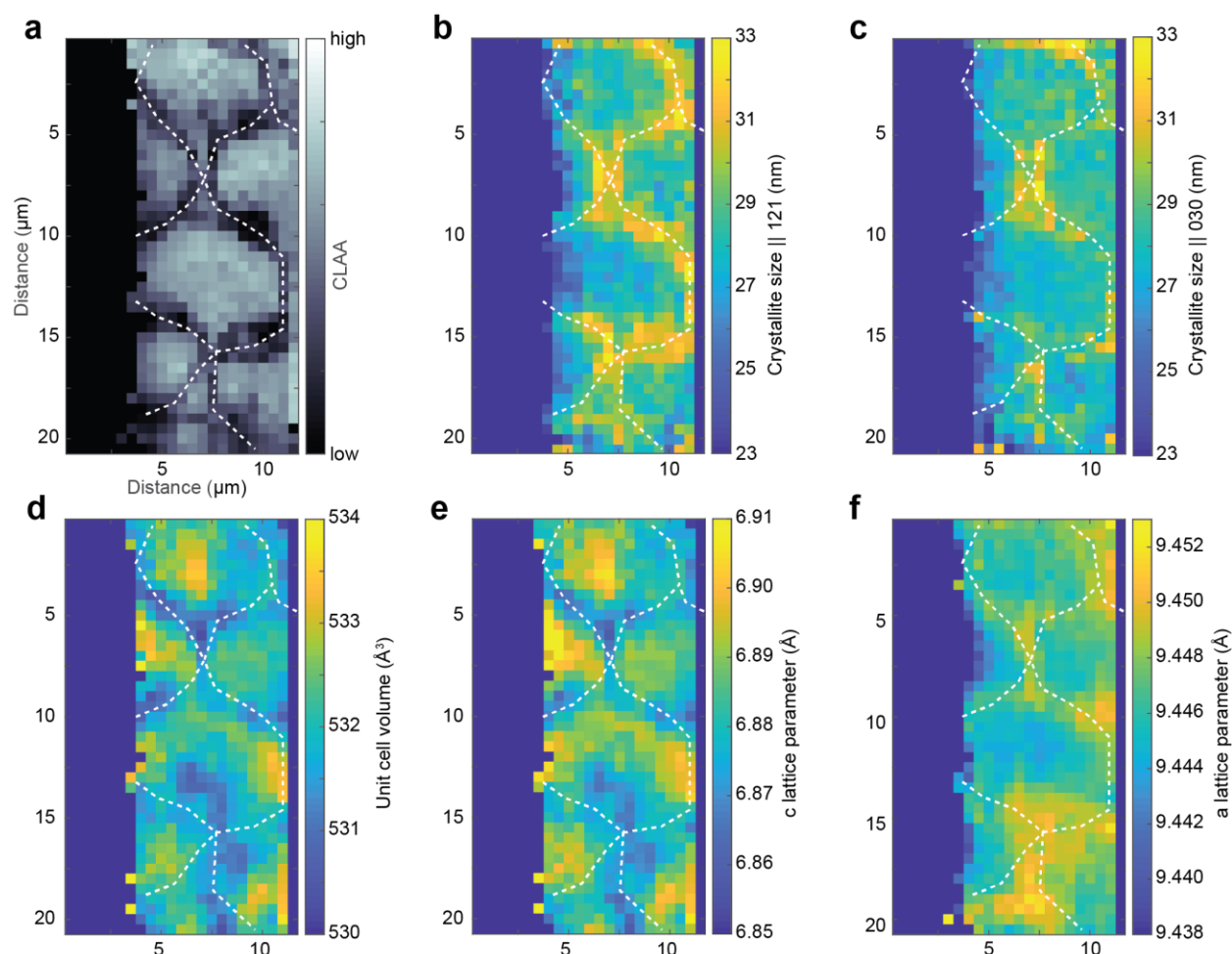
Figure 4.3. Crystallographic variation with microstructure for enamel front section.
(**a**) CLAA map reproduced from the front section of **Figure 4.2** for reference and overlaid with
hand-drawn skeleton (dotted white line) to help orient viewer to approximate distribution of low
CLAA regions. This skeleton is reproduced in all other panels. (**b**) Map of crystallite size (nm)
parallel to the 121 crystallographic direction. (**c**) Map of crystallite size (nm) parallel to the 030
crystallographic direction. (**d**) Map of unit cell volume ($Å^3$). (**e**) Map of c lattice parameter (Å). (**f**)
Map of a lattice parameter (Å). Reported values were computed as described in Section 4.4.6. Data
in this image plotted with MATLAB code created by Robert Free.

The computed crystallographic parameters within each pattern are averaged to yield values for the entire front section (**Table 4.1**). Across the 621 patterns comprising the front section, an average CLAA of 4.18 is observed, roughly half the maximum theoretical value of 8 for perfect autocorrelation. Williamson-Hall analysis of the combined diffraction profile of all 621 patterns suggests an average crystallite dimension of 42 nm and an intrinsic microstrain of $5x10^{-4}$, while Scherrer analysis suggests that the crystallite size parallel to the 030 direction is 24.8 nm. The average lattice parameters, $a = 9.447 \pm 0.002$ Å, c $= 6.883 \pm 0.013$ Å, result in a unit cell volume $V = 532.0 \pm 0.77$ Å^3.

To better evaluate the apparent correlations of crystallographic parameter variation with the enamel microstructure, subsamples from the putative rod head (30 patterns), rod tail (30 patterns), and interrod enamel (130 patterns) were selected based on the apparent key-hole microstructure observed in the CLAA map of the front section (**Figure 4.2, front**), or by thresholds in the CLAA values; all patterns with CLAA < 3 were taken to be interrod enamel. Comparing average CLAA value for each subsampled region to the whole section illustrates that regions of higher CLAA values are associated with enamel in the rod head (5.6 ± 0.3) while lower values are observed in rod tail (3.4 ± 0.9) and interrod (2.2 ± 0.5) enamel (**Table 4.1**). Crystallite sizes computed both via Scherrer and Williamson-Hall analysis are slightly larger in the tail subsample (30 nm) compared to the rod subsample (28 nm). The average Scherrer value for the crystallite dimension in the interrod matches the rod head value (28 nm), but appears to vary more widely (st. dev. = 3 nm versus 1 nm). The intrinsic microstrain is relatively consistent across all subsamples ($\sim6x10^{-4}$). The a lattice parameter within the tail and interrod is ~0.003 Å larger than in the head, while the c lattice parameter is ~0.011 Å smaller. These variations yield a slightly

smaller unit cell volume in tail and interrod enamel (531.7 $Å^3$) versus in rod head enamel (532.2 $Å^3$). In general, the standard deviation is larger in the interrod subsample than either the rod head or rod tail.

The average lattice parameters observed across the front section (a = 9.447(2) Å, c = 6.883(13) Å) fall within the ranges of values previously reported via Rietveld refinement of powdered enamel samples: a = 9.441(2) Å and c = 6.878(1) [125]; a = 9.4555(76) Å and c = 6.8809(47).[126]

Scherrer analysis of the 030 diffraction peak yields an average lateral crystallite dimension of 28 nm across the entire front section. TEM studies of mature human enamel crystallites reveal an irregular, flattened hexagonal cross-section when viewed down the 001 zone axis. The short dimension is parallel to one of the 010 directions of the hydroxylapatite lattice, and the long dimension runs perpendicular to this, bisecting the other 2 symmetry related directions in the 010 family.[116-117] Thus, Scherrer analysis of the 030 peak yields an average over this anisotropic shape, and should fall somewhere between the short dimension, thickness (t), and long dimension, width (w) usually reported for enamel. The 28 nm average observed herein falls on the lower end of previously reported values for lateral dimensions in sound mature human enamel: t = 26.3 nm and w = 68.3 nm determined by lattice plane counting in a large number of crystallites in TEM,[117] ranges of 14.0 < t < 46 nm and 27.5 < w < 78.0 nm determined by TEM,[116] and an average lateral dimension (over all $hk0$ directions) of 43.86(3) nm determined through Rietveld refinement in X-ray microdiffraction.[118]

Leveraging the ability of CLAA maps to elucidate the rod/interrod microstructure in the front view, all other crystallographic parameters extracted per pattern were correlated to their

location within the enamel microstructure (**Figure 4.3**). A qualitative consideration of the maps of CLAA, lattice parameter, and crystallite size suggests that systematic differences in these parameters exist when comparing the rod head, rod tail, and interrod regions of human enamel. The crystallite size parallel to both the 030 and 121 directions appears slightly larger (**Figure 4.3b,c**), the *a* lattice parameter is slightly larger (**Figure 4.3e**), the *c* lattice parameter is moderately smaller (**Figure 4.3f**), and the unit cell volume is slightly smaller (**Figure 4.3d**) in the tail and interrod relative to rod head enamel. Averaging crystallographic parameters within subsamples for the rod head, rod tail, and interrod regions (**Figure 4.3 front, overlays**) enables quantitative comparisons (**Table 4.1**): the average CLAA value decreases from 5.6 (head) to 3.4 (tail) and 2.2 (interrod), the lateral crystallite size is ~10% bigger in the tail than the rod head or interrod, the *a* lattice parameter is 0.003Å larger and *c* lattice parameter is 0.01 Å smaller in the tail and interrod than rod head, and the observed number of diffracting domains varies from 471 (head) up to 520 (tail) and down to 429 (interrod).

The differences in lattice parameter and crystallite lateral dimensions may be indicative of compositional differences between the crystallite populations within the rod head and the tail and interrod regions. While nominally hydroxylapatite ($Ca_5(PO_4)_3OH$), bulk enamel is known to include many impurities, including carbonate (2.7-5 wt%), magnesium (0.2-0.6 wt%), sodium (0.2-0.9 wt%), and fluorine (0.01 wt%).[127-129] Impurity substitutions in OHAp are known to affect lattice parameters.[130] Increasing substitution of CO_3^{2-} for PO_4^{3-} (B-type substitution) between 0 wt% and 5 wt % CO_3^{2-} in synthetic OHAp results in a contraction in the *a* lattice parameter from 9.44 Å to 9.41 Å while the *c* parameter increases from 6.887 Å to 6.893 Å.[70,131] Meanwhile, increasing Mg^{2+} substitution for Ca^{2+} from 0 wt% to 1.25 wt% results in a contraction of the *a*

parameter from 9.443 Å to 9.424 Å and a contraction of the c parameter from 6.904 Å to 6.877 Å.[30] Similar trends were observed in synthetic apatites containing combinations of CO_3^{2-}, Mg^{2+}, and Na^+ substitutions between 2-6 wt%, 0-0.4 wt%, and 0.2-0.7 wt%, respectively.[132] While it is difficult to predict the effect of many simultaneous substitutions like those present in enamel crystallites, applying these trends to the present study suggests that interrod and tail enamel contain a lower substitutional impurity content than the rod head; the relative differences in lattice parameters observed in the rod head versus the tail/interrod (**Table 4.1**) follow the trends for increased CO_3^{2-} and Mg^{2+} substitution. This hypothesis is also consistent with the slightly smaller lateral crystallite sizes observed in rod head enamel (**Table 4.1**): hydroxylapatite crystallite size has been observed to shrink with increasing substitutional impurity content.[133]

Table 4.1. Crystallographic parameters computed for front section and selected regions

	Whole Section	Rod Head	Rod Tail	Interrod
CLAA	4.2 ± 1.3	5.6 ± 0.3	3.4 ± 0.9	2.2 ± 0.5
# of patterns	621	30	30	130
Crystallite Size (nm)				
W-H β	33 (29 – 39)	32 (28 – 38)	35 (30 – 41)	35 (30 – 41)
W-H FWHM	42 (37 – 50)	42 (38 – 46)	44 (36 – 54)	44 (37 – 54)
|| to 030	28 ± 3	28 ± 1	30 ± 1	28 ± 3
|| to 121	28 ± 3	28 ± 1	31 ± 1	29 ± 3
Strain (x10^{-4})				
W-H β	5 (1– 10)	6 (1 – 10)	6 (1 – 10)	6 (1 – 10)
W-H FWHM	6 (2 – 10)	7 (4 – 10)	7 (2 – 11)	6 (1 – 11)
a lattice parameter (Å)	9.447 ± 0.003	9.445 ± 0.001	9.448 ± 0.001	9.448 ± 0.004
c lattice parameter (Å)	6.883 ± 0.013	6.889 ± 0.004	6.878 ± 0.009	6.879 ± 0.018
Unit cell volume (Å^3)	532.0 ± 0.77	532.2 ± 0.28	531.7 ± 0.60	531.7 ± 1.0
# of diffracting domains*	386 ± 126	471 ± 76	520 ± 89	429 ± 153

Values are provided as mean ± standard deviation except for those parameters determined by Williamson-Hall "W-H" analysis (see Section 4.4.6), via either the integral breadth (β) or full-width at half-maximum (FWHM) of distributed peaks. In these cases, the 95% confidence intervals from a linear least squares fit of the Williamson-Hall plot are provided in parentheses. *see Section 4.2.4 and **Figure 4.4**.

4.2.4 COHERENT DOMAIN COUNTING
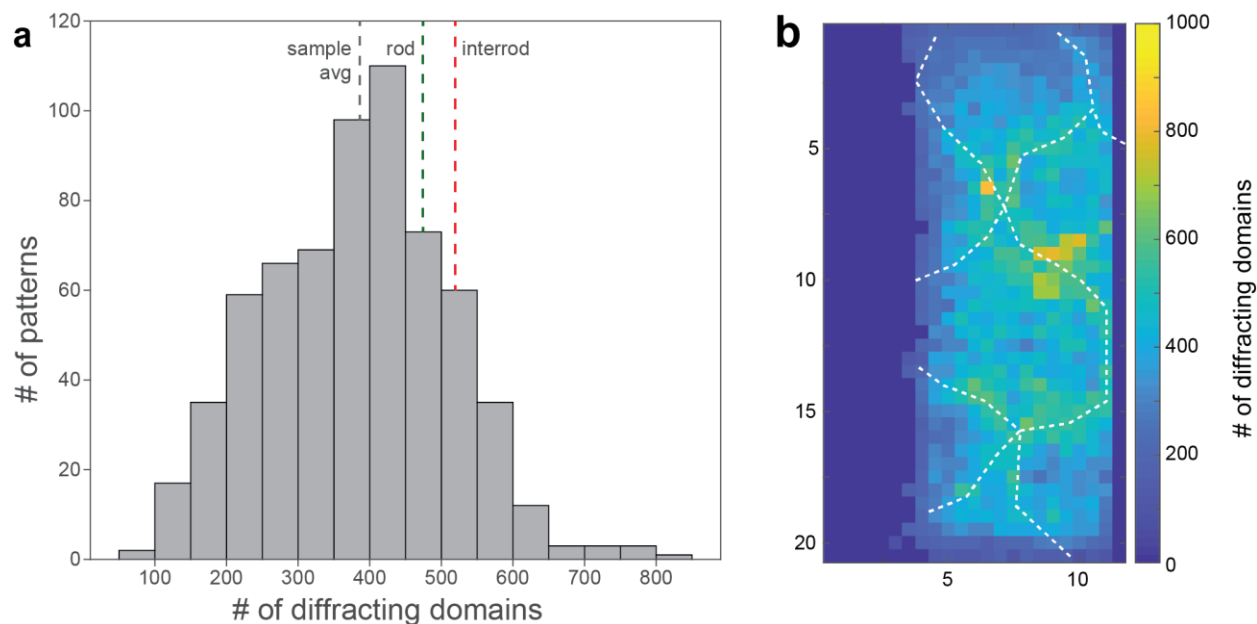
Figure 4.4. Estimating coherent domains within illuminated volumes in front section.
(**a**) Histogram of number of diffracting domains per pattern. Bins span 50 counts of diffracting domains. The positions of the average number of diffracting domains for the entire sample (grey), a subset of patterns taken from rod regions (green), and a subset of patterns taken from interrod regions (red) (see **Table 4.1**) are shown via labeled dotted lines. (**b**) Map of the number of diffracting domains in each pattern across front section. Same skeleton overlaid as in **Figure 4.3**. Data in this image recorded by Robert Free.

By conservatively counting the number of prominent spots within known *hkl* rings for enamel, an estimate for the number of diffracting domains within the illuminated volume was generated from each pattern as described in Section 4.4.7. Briefly, in order to be counted, peaks had to have an intensity greater than twice the intensity of the maximum background intensity. Additionally, there was no attempt to account for domains that are not oriented to diffract, meaning that our estimate favors undercounting diffracting domains. An average of 386 domains per pattern was measured for the entire front section (**Table 4.1** and **Figure 4.4a**). Comparing the average

number of diffracting domains between the rod and interrod subsamples reveals that there are ~10% more observed in the interrod (**Table 4.1** and **Figure 4.4b**).

4.2.5   CRYSTALLOGRAPHIC *c*-AXIS DISTRIBUTION

By comparing the 002 and 004 reflections at multiple sample rotations (about the *y*-axis) within a similar illuminated volume, more of reciprocal space can be observed to map out the orientational distribution of the crystallographic c-axes. A rotation series spanning 40° (from -16° to 24° in 8° increments) was collected in the 'side' section, and the observed c-axis diffraction is summarized on a stereographic projection (**Figure 4.5**). The collection of 002 and 004 diffraction bands are clustered near the EES direction, spanning ~60° in the cuspal-buccal plane and at least 30° in the mesial-buccal plane. The long-axis of the entire cluster appears slightly skewed from the approximate anatomical axes. It appears that there are 2 distinct orientation clouds: a smaller cloud with approximately a 3:1 aspect ratio just beneath axis 3 and a larger cloud spanning with approximately a 2:3 aspect ratio above. These regions are separated in the cuspal-buccal plane (vertically) by a ~10° region with no diffracted intensity greater than 25% of the maximum observed on any pattern. Because of the limited number of sample rotations measured, the left and right sides of these clusters may extend further than observed, but the vertical extent is well constrained.
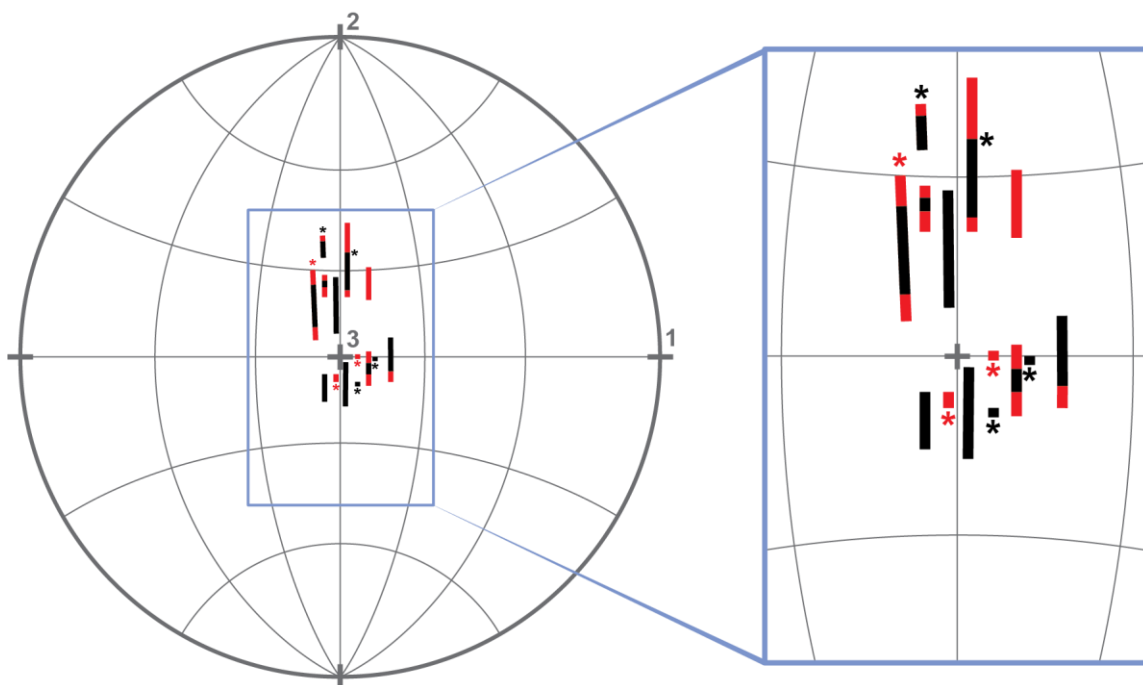
Figure 4.5. Stereographic projection showing crystallite *c*-axis orientations observed in the diffraction patterns of the rotation series; central region (blue box) enlarged on right.
For clarity, the plots show only those orientations producing intensities greater than 25% of the maximum observed on any pattern and does not differentiate between intensities greater than 25%. The black loci (bands) show orientations based on 002 diffraction rings; the red loci show additional orientations observed in 00.4 diffraction rings but not 00.2 rings. Axis 1 is the approximate distal direction, axis 2 is the approximate cuspal direction and axis 3 (the center of the stereographic projection) is the approximate buccal (EES) direction. The arcs mark orientations every 30° (on the Wulff net). The asterisks identify orientations of –c axis direction reflected into the same coordinate system as +c axis direction for the 00.2 (black) and 00.4 (red) rings. For basic information on stereographic projections, see *Elements of X-ray Diffraction*.[134] Data in this image recorded by Robert Free and Stuart Stock

This distribution of *c*-axis orientations may help explain the discrepancy between the enamel microstructure schema (**Figure 4.1b**) and the CLAA results for the "top" and "side" sections (**Figure 4.2**) discussed in Section 4.2.2. The lack of clearly defined rod and interrod regions may be due not only to the orientation of the liftout, as discussed in that section, but also the natural variations in the *c*-axis direction as determined using stereographic projection. As the *c*-axis orientation varies as much as 60° in the cuspal-buccal plane and 30° in the buccal-distal

plane it is likely that this spread in crystallite orientations effectively "washes out" the rod boundaries, making it difficult to clearly distinguish rod from interrod regions.

4.2.6 CRYSTALLITE LENGTH

Reported crystallite lengths along the *c*-axis in human enamel have a well-documented inconsistency when measured via TEM versus X-ray diffraction. Little summarized these differences in early investigations, and the disagreements have persisted even as technique resolution has improved.[135] Characterizations via SEM and TEM support the view that crystallites extend multiple microns along the *c*-axis, leading some authors to hypothesize that single crystals might run continuously from the DEJ to the EES.[111,117,136] Under this view, a crystallite density of 558 crystallites/μm^2 is reported in mature enamel.[117] Meanwhile, coherent domain lengths along the *c*-axis computed from Rietveld analysis of X-ray diffraction are much smaller, including values ranging from 24.97 nm to 109.16(7) nm.[118,121] A possible explanation for this discrepancy is that, within each crystallite, there exist crystalline subdomains with small angle grain boundaries. Another possibility is that the crystallites have continuous, but strained lattices that allow for the crystallites to curve or bend.

In order to further investigate this discrepancy, we used our own data to determine the number of diffracting domains within the illuminated volume (Section 4.4.7). By comparing this number to the average cross-sectional area of crystallites (under the assumption that they are a coherent single crystal along the entire length), we can see if this assumption is reasonable. Our analysis found 386 ± 126 diffracting domains per pattern. With a probe size of 500 nm x 500 nm, this comes to 1544 ± 504 diffracting domains per square micron. If each enamel crystallite extends

for microns along the *c*-axis, this would mean that each diffracting domain corresponds to an enamel crystallite that extends through the thickness of the sample.[111,136] If this were the case, we can approximate the cross sectional area of an enamel rod by adding the area of the head (approximated as a circle with 5 μm diameter) to the area of the tail (approximated as a trapezoid) (**Figure 4.6**).
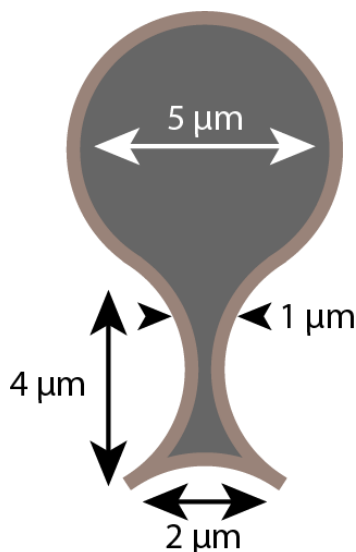
Figure 4.6. Approximated enamel rod dimensions for calculation of cross-sectional area

Using this method, we obtain an approximate cross-sectional area of 25.6 μm^2. Each crystallite would therefore have to have a cross-sectional area of ~647.7 nm^2 in order for all of them to fit inside a rod (not accounting for the amorphous phase between crystallites). The crystallite cross sectional dimensions are known to be on the order of 20-50 nm in the short dimension and 70-170 nm in the longer dimension, meaning the actual cross-sectional area is somewhat larger than 647.7 nm^2. With the well characterized crystallite dimensions, we would expect to see between 30 and 178 diffracting domains per pattern, which is well below the number

we actually see. Taking into account both the electron microscopy observations indicating that crystallites are morphologically continuous over large distances, and the diffraction data suggesting there are more diffracting domains per pattern than we'd expect to see if each crystallite is a single diffracting domain, the most likely scenario is that each crystallite has multiple domains with incoherent boundaries every ~100 nm. This is supported by a study that used dark-field electron microcopy to study human enamel crystallites. Using this technique on non-002 reflections, these researchers found that the relatively long crystallites seen in bright field imaging condition were actually composed of sub-domains that were around 32.1 ± 3.5 nm long and 33.6 ± 1.7 nm wide.[137] While this is a bit smaller than we suggest, this may be due to the fact that we likely undercounted the number of diffracting domains in our analysis to keep the estimate conservative.

4.3   CONCLUSIONS

In summary, we were able to use autocorrelation values as a measure of order, and so differentiate between head, tail, and interrod enamel in the sample volume. We could then do analysis on each of these regions to compare a and c-axis lattice parameters, crystallite size, and crystallite volume. The systematic changes in crystallite lattice parameters and volume across the rod suggests there may be compositional differences between crystallites in these domains. Additionally, by counting the diffracting domains, we showed that crystallites are not made of up a single coherent domain that is microns long in the c dimension, but likely many small domains with incoherent boundaries ever ~100 nm

4.4 MATERIALS AND METHODS

4.4.1 SAMPLE PREPARATION

Two de-identified healthy human premolars extracted for orthodontic reasons were obtained from Drs. Akers, Stohle, and Borden of The Center for Oral, Maxillofacial, and Implant Surgery (Evanston, IL) and disinfected in 10% buffered formalin for 10 days. To generate 1 µm thick sections of oriented enamel, a previously described preparation sequence was followed.[124] Briefly, whole teeth were embedded, coarsely sectioned with a diamond saw, and progressively ground and polished to a 50nm roughness using SiC grit paper (Buehler) and diamond slurries (Buehler). Next, an established focused ion beam (FIB) liftout procedure was used to extract and clean a thin plate (20 µm x 8 µm x 1 µm) of outer enamel.[25] Three roughly orthogonal enamel sections were generated from the buccal regions (**Figure 4.1a**) of the two premolars, targeting the orientations illustrated by the block faces of the schema in **Figure 4.1b** Tooth 1 was sectioned normal to the mesial-distal direction along the midline (illustrated in **Figure 4.1a**), and a liftout oriented roughly parallel to the DEJ and EES was taken such that the long axis of the enamel rods runs normal to the large plane of the section (**Figure 4.1b,d**) and thus parallel to the x-ray beam direction during measurement (**Figure 4.1f**). This section is termed the 'front' view. Tooth 2 was sectioned normal to the buccal-lingual direction and just into the outer enamel, and two orthogonal liftout were extracted from this surface, producing the 'top' and 'side' view sections. While the mutual orthogonality of all 3 sections was the goal, it is important to note that while the top and side sections are orthogonal to one another, their relative orientation to the front section is less controlled since they come from a different tooth and slightly displaced region of the tooth.

4.4.2 SYNCHROTRON X-RAY MICRODIFFRACTION

Synchrotron X-ray microdiffraction was performed at beamline 34 ID-E of the Advanced Photon Source (APS) at Argonne National Laboratory (Argonne, IL, USA). Monochromatic X-rays (17 keV) were focused to a probe size of 500 nm x 500 nm and 2D diffraction patterns were collected in transmission on a MAR165 area detector positioned with its face perpendicular to the incident X-ray beam (**Figure 4.1F**). Samples were mounted on a translational stage with 250 nm precision in x, y, and z motions (perpendicular to the beam and in the horizontal plane; perpendicular to the beam and vertical; along the beam direction; respectively) and positioned at the focal point of the beam. Diffraction patterns were collected with two 30 second integrations and correlated to remove spurious counts from gamma rays or electronic noise, yielding an effective exposure time of 60 seconds per pattern. 2D maps with 500 nm isotropic steps were collected across the enamel sections in a raster sequence, including patterns through air, the FIB platinum used for sample mounting, and the copper grid. Standard patterns were also collected using a NIST powdered ceria standard (for calibration) and single-crystalline silicon (for instrumental broadening).

Samples could also be manually rotated about the y axis with 0.5° accuracy. On the side view section, horizontal 1D line scans spanning the sample were collected at 6 rotation angles in 8° increments, yielding 23 diffraction patterns of the same line at -24°, -16°, -8°, 0°, 8°, and 16° relative to the rotation angle of the large 2D map. These linescans spanned the horizontal extent of the sample in 500 nm steps (complete sampling), allowing horizontal registration of the sample edges and center between rotation angles with ~250 nm accuracy.

4.4.3 DATA CALIBRATION AND BACKGROUND CORRECTION

Raw 2D diffraction patterns (2048x2048 16-bit TIFFs) were pre-processed following procedures described elsewhere.[124] In brief, ImageJ and Fit2D were used to perform background subtraction, calibration, and transformation from polar to Cartesian coordinates (azimuthal angle χ vs. d-spacing and 2θ) for each pattern (see example in **Figure 4.7**).[138-139] All further analysis (described below) and plotting was performed using a MATLAB (MathWorks 2018b) script developed by the authors.

4.4.4 MAPPING ORDER/DISORDER IN ENAMEL VIA AZIMUTHAL AUTOCORRELATION

The authors recently developed a novel computational approach to distinguish between the rod and interrod regions of thin enamel sections using only microdiffraction patterns, and these are briefly summarized here.[124] The distribution of crystallite orientations within the irradiated volume is reflected in the azimuthal distribution of measured intensity in any individual hkl diffraction ring. If the diffraction spots within a ring are clustered together (azimuthally correlated), there is greater crystallographic order (texture) within the sampled volume than if the spots are more widely spread around the diffraction ring. The azimuthal autocorrelation measures this clustering, and, for each position (x,y) within the specimen, analysis of the azimuthal autocorrelation of diffracted intensity within each of multiple hkl rings would then allow the sampled area to be partitioned into more ordered and less ordered regions.

The intensity within each diffraction ring is averaged within L=256 bins of ~1.4° azimthual width. Within diffraction ring hkl, the azimuthal autocorrelation r_j of proximity j relates the

intensity $I_{hkl}(\chi)$ within each azimuthal bin to those that are j azimuthal bins away over the entire profile via:

$$r_j = \frac{c_j}{c_0},$$

where

$$c_j = \frac{1}{L}\sum_{i=1}^{L-j}(I_i - \bar{I})(I_{i+j} - \bar{I}),$$

L is the total number of azimuthal bins, $\bar{I}$ is the mean intensity, and c_0 reduces to the sample variance. The value of r_j can vary between -1 and 1. The average autocorrelation of the first 8 proximities is defined as the 'local azimuthal autocorrelation,' $\bar{r}$ (LAA), and this captures the autocorrelation in highly localized neighborhoods and insulates against artifacts introduced by the selection of azimuthal bin size. Pure powder patterns with a uniform azimuthal intensity distribution have a low LAA, and patterns with high crystallographic texture have regions of localized high intensity and an increased LAA. Inspection of 2D diffraction patterns of enamel suggested that the 022, 030, 112, and 121 quadruplet reflections hold texture information (**Figure 4.7c**), so a final quantity, termed the 'combined local azimuthal autocorrelation' (CLAA), was defined as the sum of LAA values for each reflection weighted by their total intensity. Values of LLA and CLAA were calculated for each x,y of the maps using a custom MATLAB (MathWorks) code. More details appear elsewhere.[124]
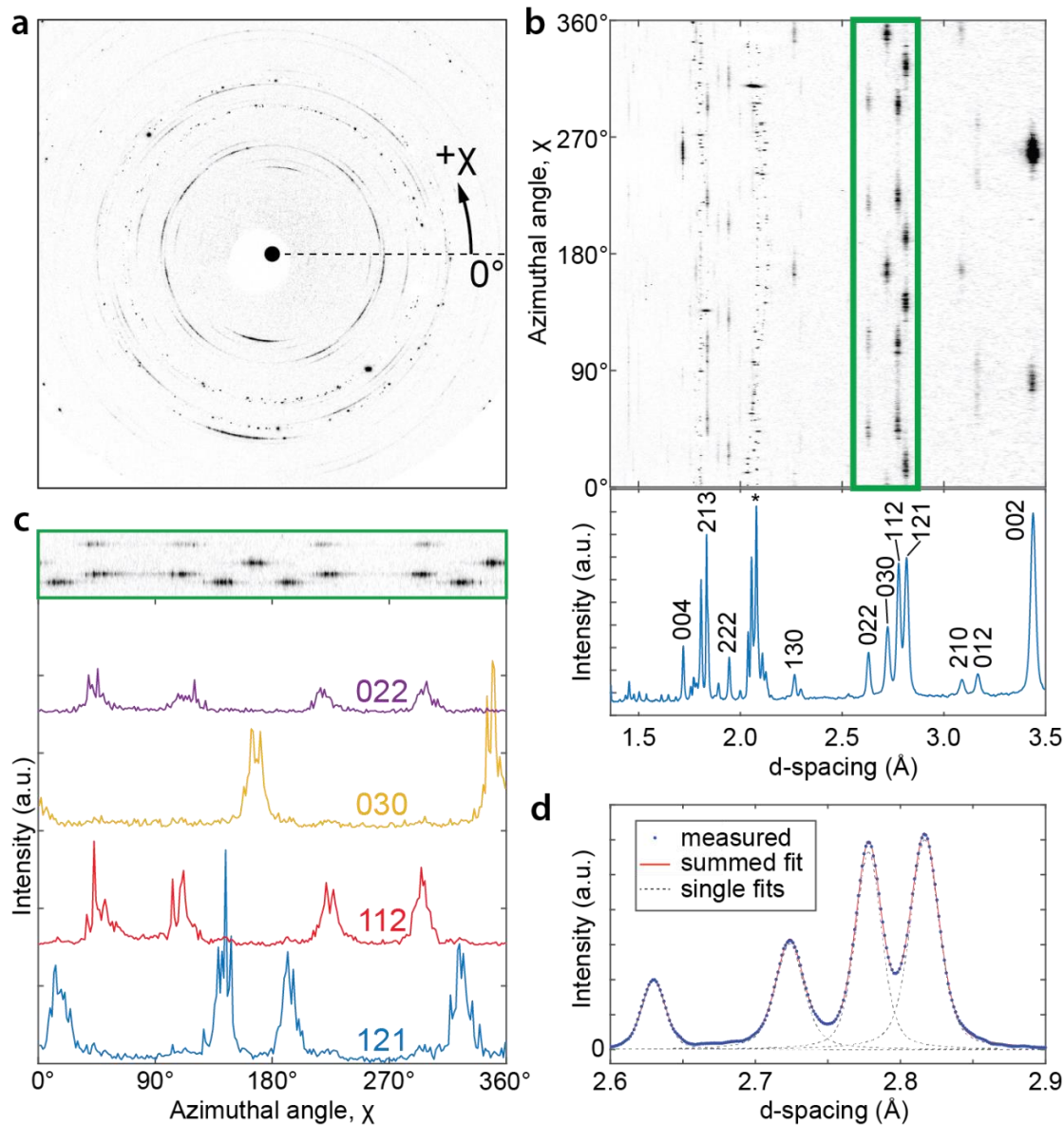
Figure 4.7. Data processing
(**a**) A single background-corrected 2D diffraction pattern of highly-ordered human enamel from the top view section. Darker grays indicate higher intensity. (**b, top**) Cartesian transform of diffraction pattern in panel A plotted as azimuthal angle (χ) vs. d-spacing (Å). (**b, bottom**) Corresponding 1D diffraction pattern generated by integrating over 360° azimuthally. Indexed peaks for hydroxyapatite (OHAp) structure. Starred peaks correspond to erroneous scattering not originating in the enamel volume. (**c**) Intensity vs. azimuthal angle for selected families of reflections within the OHAp quadruplet: 022 (purple), 030 (yellow), 112 (red), and 121 (blue). (**d**) Example of fitting the OHAp quadruplet of the 1D diffraction pattern of panel **b**. A linear combination of 4 pseudo-Voigt profiles (grey dashed lines) are simultaneously fit to the background-corrected data (blue dots) to compose the final fit (red line). Adapted from [124].

4.4.5   1D DIFFRACTION PROFILE PEAK FITTING

The 2D diffraction patterns were integrated over the azimuthal angle (χ) to yield 1D profiles (**Figure 4.7b, bottom**). The diffraction peaks *hkl* within these 1D patterns were fit with symmetric pseudo-Voigt profiles, yielding precise values of peak position (mean), peak breadths (full width at half maximum intensity, FWHM, and integral breadth, β), and peak intensities (intensity of the mean) for each map.

4.4.6   COMPUTING CRYSTALLOGRAPHIC PARAMETERS

The *a* and *c* lattice parameters were computed from the peak positions of the 030 and 121, or 030 and 002 reflections plotted vs. *d*-spacing. Because the 030 and 121 peaks fall very close to the 112 and 022 reflections (OHAp quadruplet), all four of the peaks were simultaneously fit by a linear combination of 4 pseudo-Voigt functions (e.g. **Figure 4.7d**). Because OHAp is hexagonal, the *a* lattice parameter can be directly computed from the 030 peak position and from the 002 peak mean (if present). However, when the enamel orientation does not yield 002 diffraction, the *c* lattice parameter was computed using the value of *a* and the 121 peak position. Once *a* and *c* are determined, the unit cell volume was computed according to the hexagonal crystal system.

To estimate the average crystallite size perpendicular to the 030 and 121 diffracting planes, peak broadening (β_{hkl}) was related to crystallite size (p_{hkl}) according to the Scherrer equation:

$$p_{hkl} = \frac{\kappa\,\lambda}{\beta_{hkl}\,Cos(\theta)},$$

where κ is a constant (assumed to be 1 in this study), λ is the X-ray wavelength, and θ is the Bragg angle.[140] Here, the integral breadth definition of peak broadening is used, i.e. the width of a

rectangle that is as tall as the diffraction peak with the same integrated area. The instrumental peak broadening determined from fitting a single crystalline Si standard is then subtracted in quadrature, followed by a linear subtraction of broadening due to the relatively consistent intrinsic strain observed across the sample. This finally yields the corrected values for peak broadening from which estimates of crystallite size are computed according to the Scherrer equation.

Williamson-Hall analysis was also performed to determine a measure of crystallite size and microstrain for combined patterns within specified subsamples of the total front section map. Eleven well-defined diffraction peaks between d-spacings from 1.5 – 8.4 Å (2θ between 28° and 5°) were fit, and the peak positions and integral breadths were used to generate a plot via the relationship:

$$\beta_{hkl}(\theta)\,cos\,(\theta)\ =\ \frac{K\lambda}{p} + 4\,\varepsilon\,sin\,(\theta),$$

where the only new parameter, ε, is the microstrain [141]. When $\beta_{hkl}(\theta)\,cos\,(\theta)$ is plotted vs. $4\,sin\,(\theta)$ and fit by a line, the slope and intercept give the microstrain and average particle size respectively [134]. Because this analysis incorporates many *hkl* reflections distributed across 2θ, it yields a pseudo-average of particle size over a range of crystallographic directions. For highly anisotropic crystallites like those in enamel, this implies that values intermediate between the smallest and largest dimensions of the crystallites are expected.

4.4.7   COUNTING COHERENT DOMAINS

To estimate the number of individual coherent domains oriented to diffract within each irradiated volume, an automated 'spot counting' script was implemented. Briefly, 29 clearly distinguishable *hkl* reflections with adequate intensity above background were selected for this

analysis. A region of the diffraction pattern with no diffraction peaks was used to define the background intensity. For each reflection, a peak finding function was applied to the pattern of diffracted intensity vs. azimuthal angle, identifying any peak that was at least twice as prominent as the most prominent peak observed in the noise-only region of the pattern. The number of all such peaks identified across these 29 *hkl* reflections is reported as a conservative estimate of coherent domains within the irradiated volume. It should be noted that all decisions made for computational convenience in this analysis were chosen to favor an undercounting of spots. Some very weak *hkl* reflections were omitted from the analysis; the minimum prominence was chosen to be quite high (omitting some weak peaks from the count), and no correction was attempted to account for domains that are not oriented to diffract. The authors note that, although it is possible for a domain to simultaneously produce two diffraction spots, the geometric conditions for diffraction are so strict that this occurrence must be rare and should not affect the arguments made in this study.

4.4.8   MEAN *c*-AXIS ORIENTATION

For sections in which the crystallographic *c*-axes of the enamel crystallites are nearly in the plane of the sample (top and side views), strongly textured 002 and 004 diffraction arcs are observed (e.g. **Figure 4.7a**), and these arcs represent a range of crystallite orientations. From the 002 azimuthal intensity profile, the χ angle for the mean projected *c*-axis orientation can be determined as follows for each position across the specimen. A custom Matlab script was used to approximate the azimuthal position, azimuthal breadth, and peak prominence of the 002 diffraction arcs for each pattern. For computational convenience, this was achieved through the use of a low-pass filter to smooth the azimuthal profile, followed by application of Matlab's findpeaks function.

The most prominent peak within each pattern was taken as the preferred *c*-axis orientation for that position, and 2D vector fields were generated to illustrate the orientation and strength of the *c*-axis texturing across the samples (see **Figure 4.2**).

4.4.9   ROTATION SERIES STEREOGRAPHIC PROJECTION ANALYSIS

For each of the 6 sample rotations (-24°, -16°, -8°, 0°, 8°, and 16°), the horizontal linescan (23 patterns) was manually examined to define the left and right edges of the sample. The edges were assigned as the first pattern in which enamel diffraction was observed on both sides, no matter how weak the intensity. This consistently yielded 16 sample-containing patterns per linescan (7.5 µm across), allowing for direct registration after deleting air patterns on either side. By manually reviewing corresponding patterns between rotation angles, a position with high diffracted intensity and variation in the 002 and 004 reflections was selected for further analysis. The 002 and 004 diffraction rings were each individually analyzed as follows: the azimuthal intensity profiles were extracted for the same position at each of the 6 rotation angles, the intensity was normalized to the maximum intensity observed in any of the 6 profiles, and all azimuthal ranges over which the intensity surpassed 25% of this maximum were recorded. With knowledge of the 2θ for the 002 and 004 reflections, each band of >25% intensity from each rotation angle was recorded on a stereographic projection, rotating 8° between patterns to preserve the relative orientation between the subset of diffracting domains observed at each rotation angle. This analysis allows one to visualize the larger orientational distribution of *c*-axes within the selected enamel region. A detailed description of constructing a stereographic projection can be found by reviewing standard texts such as *Elements of X-ray Diffraction.*[134]

5.   ATOM PROBE TOMOGRAPHY OF ENAMEL PATHOLOGIES

Work from this chapter is currently ongoing and will be a published manuscript in the near future. The work with teeth affected by molar incisor hypomineralization and fluorosis was done as a collaboration with Dr. Sophia Houari from the University of Paris, Garancière Dental School. The *in vitro* caries model was done in collaboration with Professor Ana Bedran-Russo and her post doc Camila Zamperini.

5.1   INTRODUCTION

Atom probe tomography has enabled thorough characterization of enamel composition on the nanoscale. Having established the structure of healthy human enamel, we can now use this technique to investigate any changes that may occur to the chemistry or structure of crystallites as a result of various pathologies. In this chapter, I will discuss preliminary APT analysis of teeth from patients with molar incisor hypomineralization (MIH), fluorosis, and a sub-surface carious lesion model created *in vitro*.

5.1.1   MOLAR INCISOR HYPOMINERALIZATION

Molar incisor hypomineralization (MIH) is a condition that affects approximately 17% of children worldwide[90] and causes a change in the appearance of enamel on permanent incisors or first permanent molars. This condition results from decreased ameloblast activity during the maturation stage of enamel formation and has varying degrees of severity.[142] The visual effect ranges from mild opaque patches in the enamel (**Figure 5.1a**) to complete enamel breakdown after the tooth erupts (**Figure 5.1b**).
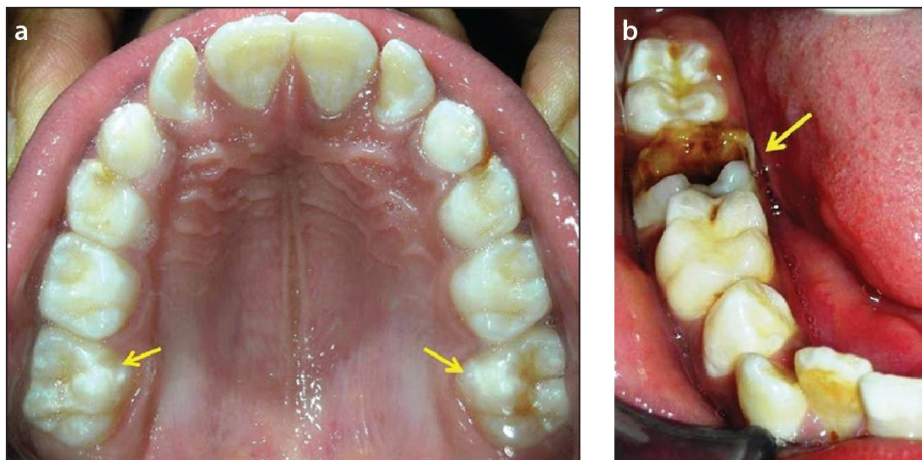
Figure 5.1. Examples of (a) mild and (b) severe MIH. Images from [143]

Lesions, or the affected regions where the enamel appears opaque, are visually distinct from healthy enamel, and have increased porosity.[90,144] Patients often report sensitivity in teeth affected by MIH.[90] Taken together, lower mineral density and decreased oral hygiene due to sensitivity render these teeth especially susceptible to caries.[90,142] There are many factors thought to cause MIH: severe illnesses contracted during amelogenesis, which may damage ameloblasts; antibiotics or toxins ingested through breastfeeding; and a low birth weight.[142] Amelogenesis is a sensitive process, and changes in factors such as pH of the enamel matrix and availability of Ca, P, and O ions, in addition to the health of ameloblasts, will have profound effects on the resulting mineral, making identification of the root cause difficult. Increased understanding of the chemical and structural changes in enamel crystallites from MIH lesions may help elucidate the mechanism by which this disease operates.

5.1.2 FLUOROSIS

In 1901, a dentist named Frederick McKay noticed patients from Colorado Springs, Colorado had dark discoloration on their teeth. After determining that it was due to the source of

the town's drinking water, and finding a similar situations in towns in Idaho and Arkansas, he finally determined in 1931 that these water supplies all had fluorine in them.[14] Further observations established that the teeth discolored due to the highly fluoridated drinking water were also resistant to caries, and lower doses of fluoride in the water could be used to prevent caries, but also have no effect on the tooth appearance.[14] Since that discovery, fluoride has been intentionally added to community water supplies to strengthen teeth against decay.[15] However, as with those initial cases, if developing teeth are overexposed to fluoride (over 1.2 ppm) during the amelogenesis process, a condition called fluorosis develops.[145] In the least severe cases, fluorosis causes opaque, white patches on enamel (**Figure 5.2a**), and in the most severe cases, enamel is pitted or even lost, resulting in secondary staining (**Figure 5.2d**).

Figure 5.2. Images of increasingly severe fluorosis. Images taken from [146]

This white, chalky appearance is caused by increased porosity in the enamel, and, with higher doses or longer exposure to fluoride, extends deeper into the enamel, resulting in poor mineralization and potential loss of the mineral.[146] DenBesten and coworkers found that, in fluorosis, enamel formation is disrupted by a decrease in the activity of proteinases that remove enamel matrix proteins from maturing enamel.[147] As a result, more proteins are retained in the mature enamel, taking up space that would otherwise be occupied by mineral, thus decreasing the density of enamel. Other studies found that enamel crystallites from fluorosis lesions had a

significant size disparity with those typically found in healthy enamel, with many crystals larger, and many much smaller.[148-149] However, other groups did not find any differences in crystallite morphology.[150-151]

5.1.3 CARIES

As the most prevalent infectious disease, dental caries affects nearly everyone by the time they reach adulthood. For a more detailed description see Section 1.3. Briefly, caries occurs when demineralization via plaque-derived acids is faster than remineralization by contact with saliva. The earliest sign of caries is called a white spot enamel lesion (WSEL) and it consists of a sub-surface lesion covered by a fully mineralized surface zone. This is detectable as a white, chalky patch on the tooth (**Figure 5.3**).

Figure 5.3. Teeth with multiple white spot lesions (white, chalky regions). Image from [152]

Improved understanding of how caries affects enamel crystallites may allow us to develop novel detection and prevention techniques, as well as more effective therapies.

5.2   PRELIMINARY RESULTS AND DISCUSSION

Work from this chapter is currently ongoing, and will be part of a published manuscript in the near future.

5.2.1   ATOM PROBE TOMOGRAPHY OF MIH-AFFECTED TEETH

Using the procedure described in Chapter 2 (Section 2.4.8), a FIB/SEM was used to extract two 30 μm x 2 μm liftouts from MIH lesions in two separate patients. From these liftouts, a total of 16 tips were prepared for APT analysis. Of those, 5 tips for the first patient and 7 tips for the second patient produced high quality data sets for further analysis. Reconstructions from these tips suggest that there are no obvious morphological changes that occur to the crystallites as a result of this condition (**Figure 5.4a-d**).
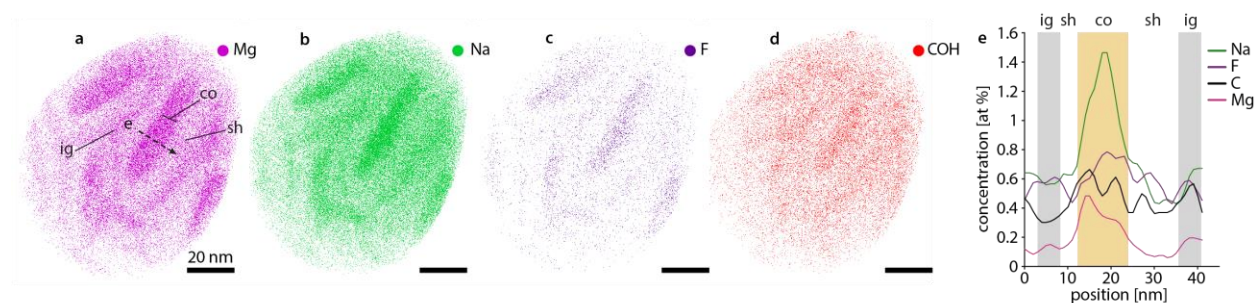
Figure 5.4. Atom probe reconstruction of enamel from a tooth affected by MIH (patient 1)
Intergranular (ig), core (co), and shell (sh) regions indicated in (**a**). (**e**) A 1D concentration profile taken across dashed line in (**a**).

In this reconstruction, we see elevation of Mg, Na, F, and COH in the intergranular phase as well as in the core, consistent with the observations we made in APT of healthy human enamel. A 1D concentration profile taken across the crystal in the center of the reconstruction reveals a dual peak in the Mg in the core (**Figure 5.4e**). While the peaks are not as well separated as in Chapter 2, this dual peak is consistent with the Mg distribution in healthy enamel. A reconstruction from a second tooth with MIH showed similar ion distribution, with a clearer biomodal distribution of Mg in the crystallite core (**Figure 5.5a**).
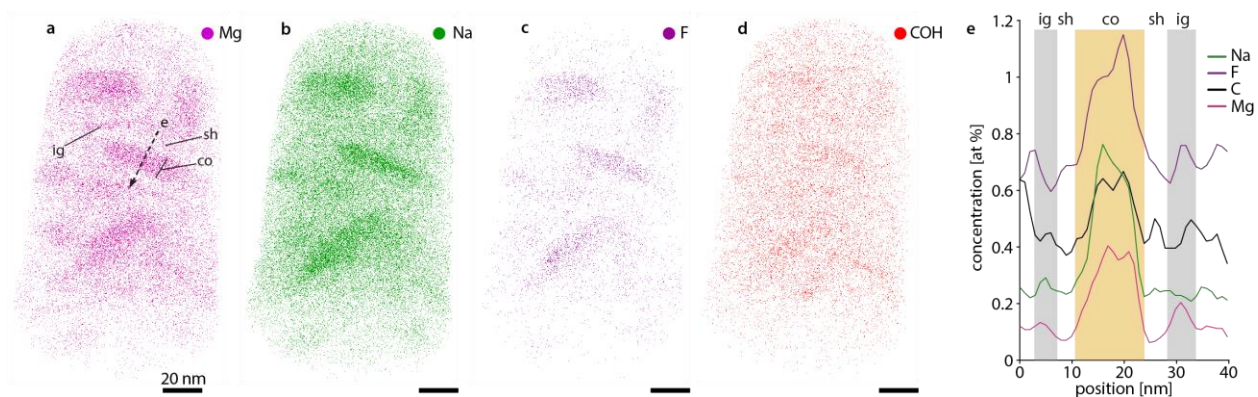
Figure 5.5. Atom probe reconstruction of enamel from a tooth affected by MIH (patient 2)
Intergranular (ig), core (co), and shell (sh) regions indicated in (**a**). (**e**) A 1D concentration profile
taken across dashed line in (**a**).

5.2.2   ATOM PROBE TOMOGRAPHY OF FLUOROSED TEETH

Preliminary APT of fluorosed teeth from 2 patients also suggests that the core-shell

structure of crystallites is not affected by this condition. The first sample contains multiple

crystallites with impurity rich cores (**Figure 5.6**, **Figure 5.7**).
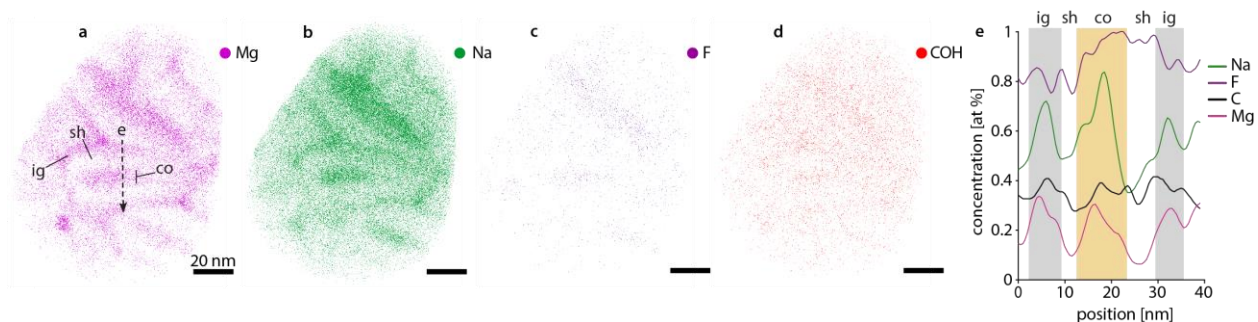
Figure 5.6. Atom probe reconstruction from tooth with fluorosis (patient 1)
Intergranular (ig), core (co), and shell (sh) regions indicated in (**a**). (**e**) A 1D concentration profile
taken across dashed line in (**a**).
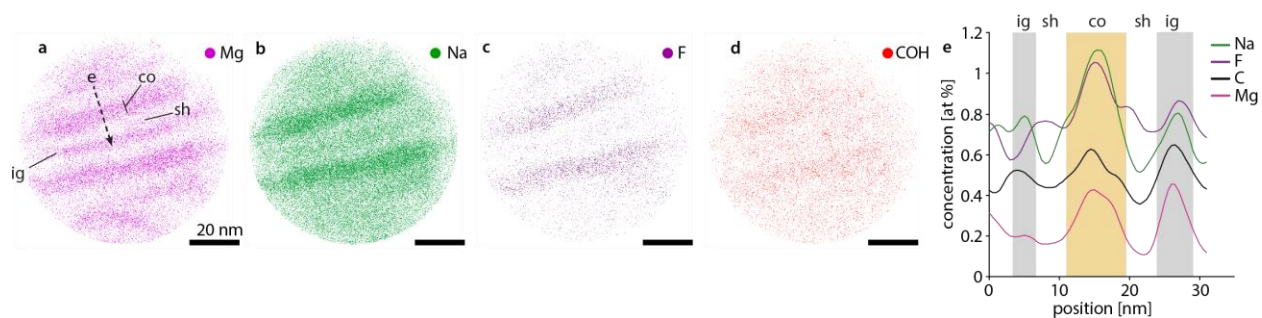
Figure 5.7. Atom probe reconstruction from tooth with fluorosis (patient 2).
Intergranular (ig), core (co), and shell (sh) regions indicated in (**a**). (**e**) A 1D concentration profile taken across dashed line in (**a**).

5.2.3   BULK COMPOSITION COMPARISON

Bulk compositional information gathered in the atom probe was compiled for each tip. It reveals that the concentration of majority species (O, Ca, and P) are relatively similar between each sample group, with the possible exception of MIH (patient 1). These values are also consistent with concentrations we see in healthy human enamel (**Table 5.1**). Minority constituent elements were more variable. Mg concentration appears higher in the fluorosis (patient 2) and healthy, fluoridated sample relative to the other samples. Na concentration appears somewhat variable between the different sample types, but F appears elevated in the two fluorosis samples and the healthy, fluoridated enamel, as expected. In order to better investigate the variance between samples, and between sample groups, we used a 1-way analysis of variance (ANOVA) test and multiple comparisons to determine if these differences were statistically significant.

Table 5.1. Bulk composition of each APT sample separated by pathology. Healthy enamel compositions used for comparison.

	Sample ID (HIT)	#hits (M)	H [at%]	Mg [at%]	O [at%]	Ca [at%]	Na [at%]	F [at%]	Cl [at%]	P [at%]	C [at%]	K [at%]	Fe [at%]
MIH (patient 1)	29357	7.2	1.51	0.30	41.69	47.21	0.25	0.20	0.05	8.69	0.07		
	29358	20.7	1.39	0.22	50.70	30.91	0.53	0.12	0.07	15.73	0.12	0.00	
	29360	18.6	3.91	0.23	47.33	33.36	0.48	0.43	0.09	13.96	0.10	0.00	0.03
	29367	20.5	4.43	0.28	46.95	33.33	0.59	0.57	0.09	13.56	0.15	0.01	0.01
	29370	32	3.47	0.20	49.25	31.07	0.57	0.28	0.09	14.92	0.13	0.01	0.00
	average		**2.94**	**0.24**	**47.18**	**35.18**	**0.49**	**0.32**	**0.08**	**13.37**	**0.12**	**0.01**	**0.01**
MIH (patient 2)	29095	19	3.31	0.19	52.58	27.90	0.31	0.33	0.23	15.05	0.10	0.00	
	29117	23	3.91	0.19	52.72	26.65	0.32	0.34	0.19	15.52	0.14	0.01	
	29181	4	2.91	0.24	53.09	28.05	0.34	0.38	0.20	14.65	0.07		
	29182	9	2.67	0.23	51.21	29.70	0.39	0.29	0.16	15.18	0.12	0.01	0.01
	29183	6.7	2.10	0.23	49.90	32.21	0.41	0.23	0.15	14.58	0.12	0.01	
	29191	26.6	2.83	0.18	49.47	31.66	0.39	0.28	0.14	14.95	0.09	0.01	
	29209	28	3.54	0.20	54.75	23.97	0.31	0.28	0.17	16.60	0.15	0.01	0.01
	average		**3.04**	**0.21**	**51.96**	**28.59**	**0.35**	**0.30**	**0.18**	**15.22**	**0.11**	**0.01**	**0.01**
Fluorosis (patient 1)	29613	13	3.78	0.23	46.96	33.47	0.61	0.78	0.08	13.73	0.16	0.01	0.02
	29614	11	3.23	0.22	47.62	33.74	0.49	0.71	0.11	13.65	0.14	0.00	
	29615	17	2.35	0.22	49.05	32.63	0.50	0.59	0.08	14.45	0.10	0.01	
	29631	12.7	2.78	0.21	48.97	32.05	0.44	0.63	0.09	14.47	0.12	0.00	0.01
	29633	7	3.00	0.23	45.94	36.40	0.54	0.63	0.06	12.99	0.12	0.00	
	average		**3.03**	**0.22**	**47.71**	**33.66**	**0.52**	**0.67**	**0.08**	**13.86**	**0.13**	**0.01**	**0.02**
Fluorosis (patient 2)	28913	6.3	3.25	0.35	46.60	35.32	0.60	0.29	0.05	13.03	0.14	0.00	
	28914	8.6	5.35	0.39	46.20	32.84	0.54	0.37	0.09	13.93	0.14		0.04
	28932	16.9	4.36	0.36	46.76	33.12	0.78	0.40	0.08	13.94	0.14	0.01	0.01
	28937	14	5.83	0.33	45.54	33.16	0.71	0.50	0.07	13.25	0.18	0.01	0.01
	28955	13.6	4.53	0.31	46.79	33.49	0.58	0.41	0.08	13.65	0.14	0.01	0.00
	28956	15	4.57	0.36	47.21	32.47	0.66	0.44	0.10	13.75	0.18	0.01	0.02
	average		**4.65**	**0.35**	**46.52**	**33.40**	**0.65**	**0.40**	**0.08**	**13.59**	**0.15**	**0.01**	**0.02**
Healthy Fluoridated	165799	27.8	4.37	0.36	46.91	32.66	1.03	0.66	0.09	13.75	0.16	0.00	0.00
	165891	28	5.49	0.28	48.17	30.23	0.75	0.52	0.08	14.32	0.16	0.00	0.00
	165912	60	3.95	0.39	46.11	34.84	1.01	0.55	0.07	12.96	0.13	0.00	0.00
	average		**4.60**	**0.34**	**47.06**	**32.58**	**0.93**	**0.58**	**0.08**	**13.67**	**0.15**		
Healthy Untreated	168387	35	1.72	0.30	48.79	36.62	0.46	0.22	0.14	11.70	0.05	0.00	0.00
	24660	9.05	4.60	0.23	48.94	30.48	0.63	0.51	0.13	14.31	0.15	0.00	0.00
	average		**3.16**	**0.27**	**48.87**	**33.55**	**0.54**	**0.36**	**0.13**	**13.01**	**0.10**		

Boxplots rendered using the results of the 1-way-ANOVA for the minority constituent elements are shown below (**Figure 5.8**). The concentration of F is elevated most in fluorosis (patient 1) and sound, treated enamel, and is slightly elevated in fluorosis (patient 2) (**Figure 5.8a**). Na appears variable between all samples, with a high amount in the sound, treated enamel due to the NaF treatment (**Figure 5.8b**). Mg appears elevated in fluorosis (patient 2) and sound, treated (**Figure 5.8c**), but C concentration is fairly consistent across all sample groups (**Figure 5.8d**). Cl is significantly higher in MIH (patient 2); however, the other MIH sample did not show elevated amounts (**Figure 5.8e**). The concentration of K also appears to be relatively consistent with the exception of the sound enamel samples (K was not included in the analysis of healthy enamel, but is not at a high enough concentration to appreciably alter the bulk composition of those samples) (**Figure 5.8f**).
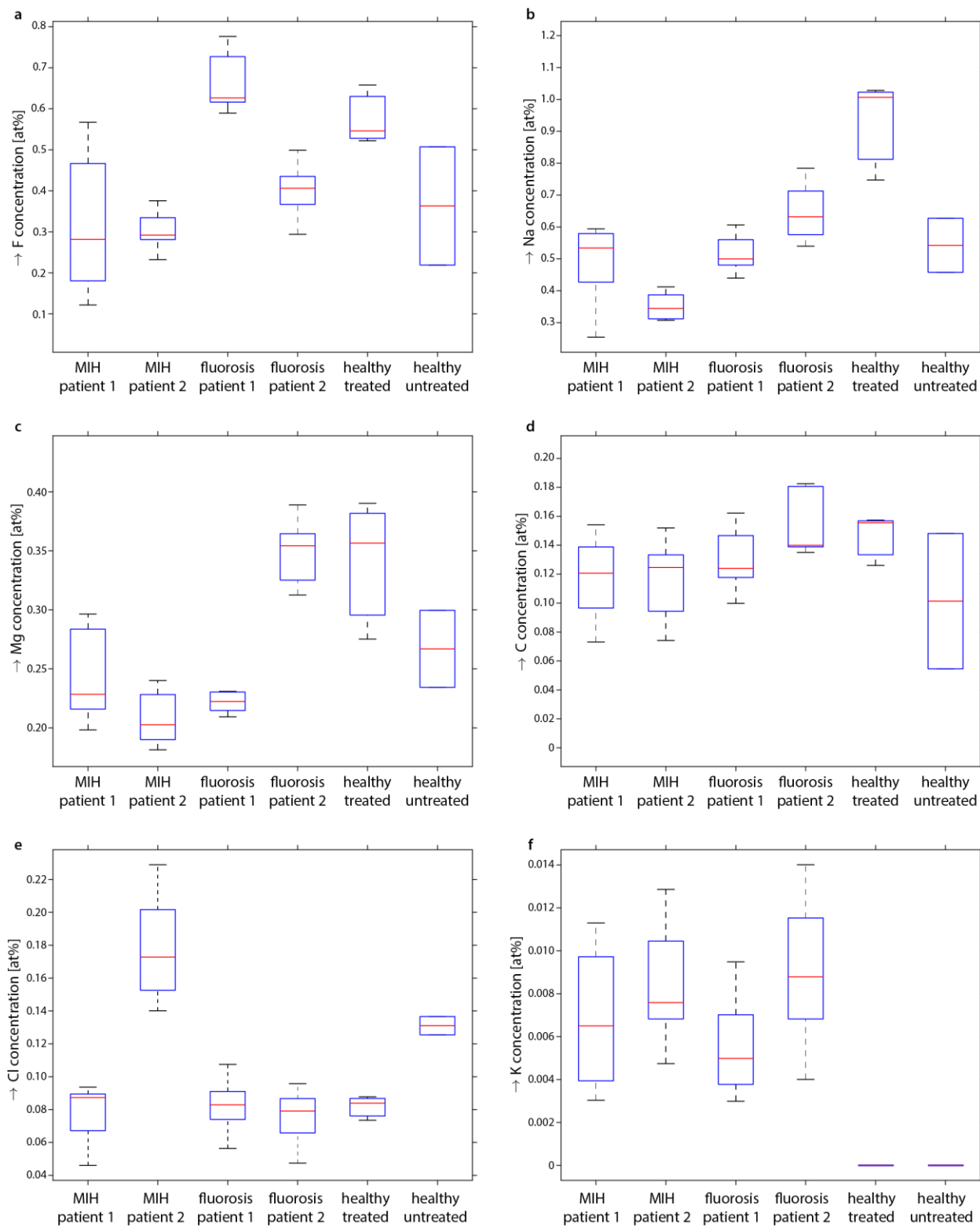
Figure 5.8. Boxplots comparing mean and variance for concentrations of trace elements between the different experimental groups.

A multiple comparison analysis was then used to determine if the mean concentration for each element was significantly different between experimental groups. This analysis revealed that MIH (patient 2) had a higher concentration of O and Cl (**Figure 5.9a,b**). In MIH (patient 2), concentration of Ca appeared low and P was high, but these means were not different enough to be indicated as statistically significant in the multiple comparisons analysis. Multiple comparison plots for Mg and Na (**Figure 5.9c,d**) reveal that fluorosis (patient 2) had a similar concentration of Mg compared to the fluoridated sound enamel and was significantly higher than the rest of the sample groups. All samples had statistically similar Na concentrations except for the sound enamel that was treated with NaF, which was expected to have a high Na concentration. Finally, a comparison of the concentration of F between samples (**Figure 5.9e,f**) revealed no statistically significant difference between fluorosis (patient 2) and the rest of the non-fluorosis samples. By contrast, fluorosis (patient 1) had a significantly higher mean concentration than all of the other sample groups with the exception of the fluoridated healthy enamel.
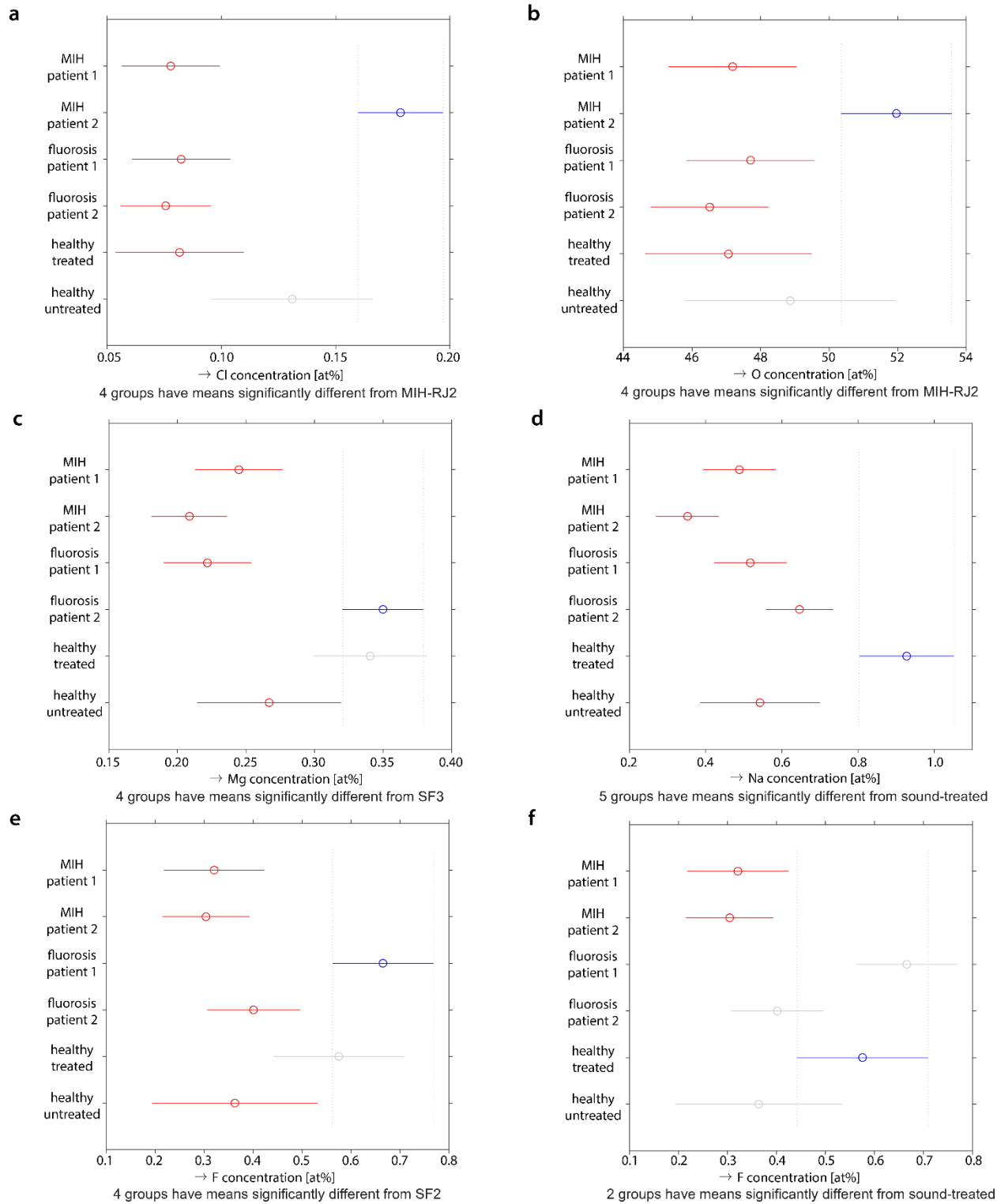
Figure 5.9. Multiple comparison analysis.
Multiple comparison of means for (**a**) Cl, (**b**) O, (**c**) Mg, (**d**) Na, and (**e,f**) F.

5.2.4 *IN VITRO* CARIES

A sub-surface lesion was created *in vitro* after 3 days of cyclical exposure to 10% sucrose (8 cycles per day). SEM confirmed the presence of a mineralized surface zone covering a lesion with decreased mineral density (**Figure 5.10**).
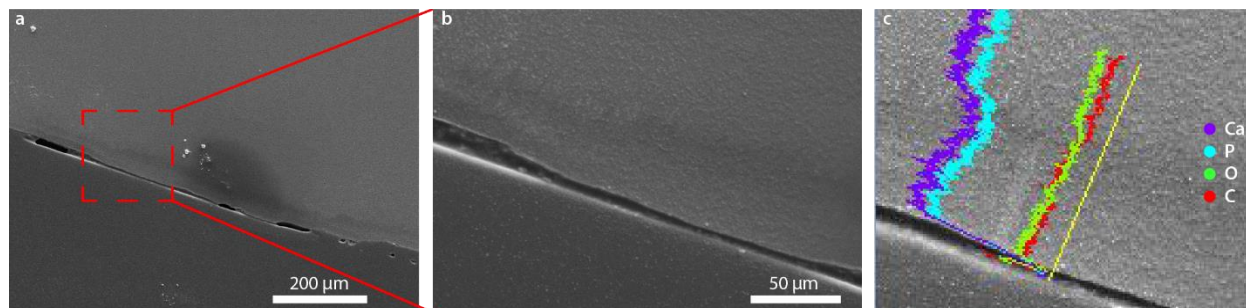
Figure 5.10. SEM of artificial white spot enamel lesion.
(**c**) EDS line spectrum showing decreased concentration of Ca and P in lesion region.

APT analysis was then performed on FIB liftouts from the surface zone, lesion, and sound enamel on the same tooth. Reconstructions from the surface zone and lesion suggest disruption of the crystallite structure seen in healthy enamel. There appears to be co-localization of Mg, F, C, and H in large clusters in both the surface zone and the lesion (**Figure 5.11**, **Figure 5.12**). The distribution of Na was largely homogeneous (not shown). The co-localization of C and H suggest that at least some of this carbon is organic in nature, and does not belong to carbonate inclusions. Individual crystallites are also not apparent, making it difficult to ascertain where these pockets of organic exist in the structure of enamel.
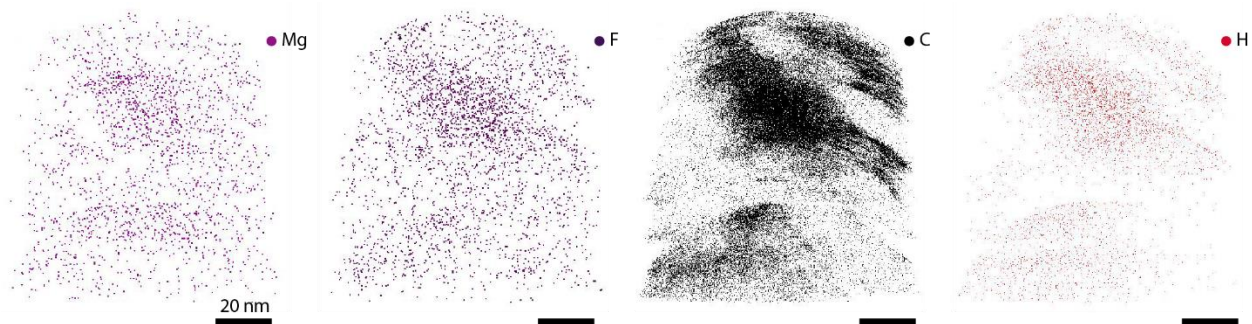
Figure 5.11. APT reconstruction of surface zone enamel.
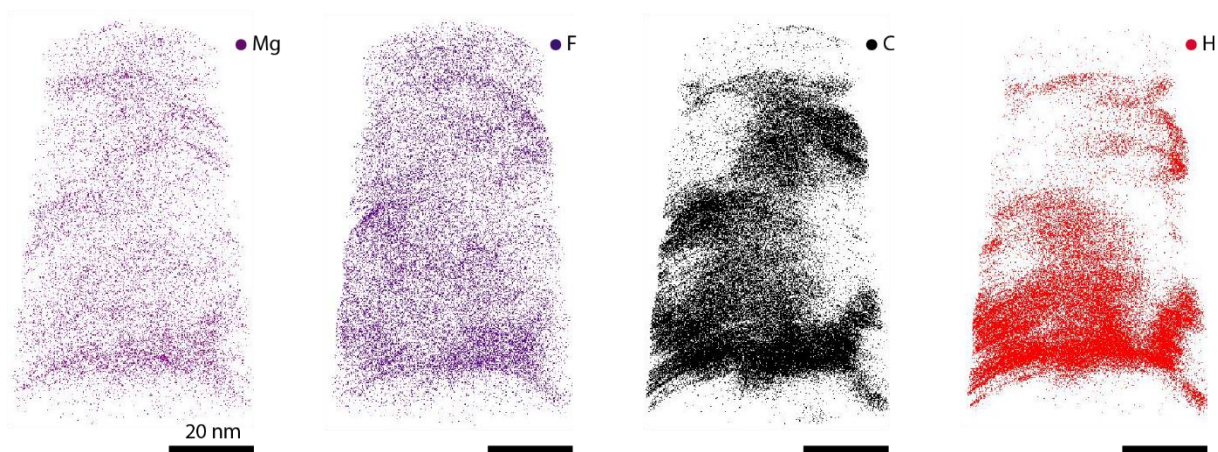
Figure 5.12. **APT reconstruction of enamel from the sub-surface lesion.**

Comparison to the APT of sound enamel within the same tooth reveals that, while the boundaries between crystallites are not clear, co-localization of high concentrations of Mg, Na, and F is observed in regions consistent with the size of crystallite cores (**Figure 5.13**). There is also significantly less C present in the reconstruction compared to those from the surface zone and lesions regions, with no large pockets of C or H present.
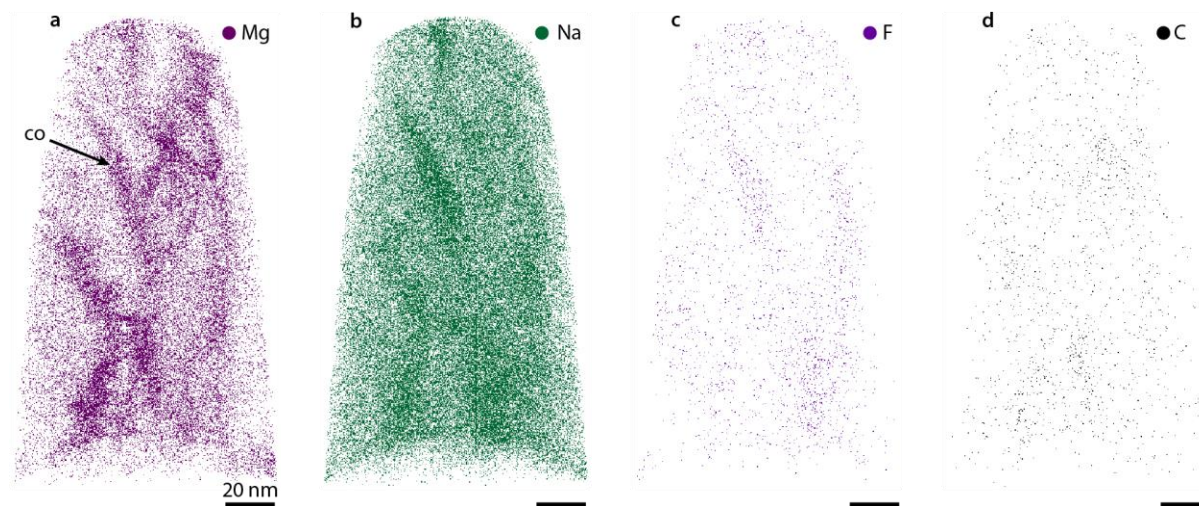
Figure 5.13. APT reconstruction of sound enamel taken from tooth in which artificial sub-surface lesion was induced
Potential crystallite core indicated by arrow in (**a**).

Bulk compositional analysis of tips from these three regions reveals a high concentration of H, Mg, C, and Cl in the surface zone and lesion relative to sound enamel (**Table 5.2**). This suggests that, during the formation of the sub-surface lesion, enough mineral dissolves that ions and potentially larger hydrocarbons diffuse relatively far into the enamel. The sound region, where nail polish masked the tooth surface, showed no significant diffusion of these ions into the enamel.

Table 5.2. Bulk composition for tips taken from sound, surface zone, and lesion enamel.

	HIT number	#hits (M)	H [at%]	Mg [at%]	O [at%]	Ca [at%]	Na [at%]	F [at%]	P [at%]	C [at%]	Cl [at%]
Sound	29376	7	2.3	0.2	53.1	26.9	0.3	0.3	16.4	0.1	0.2
	29377	14.8	2.7	0.2	52.1	27.6	0.4	0.6	16.1	0.1	
	29451	24	2.6	0.2	51.9	28.3	0.3	0.3	16.1	0.1	0.1
	29573	26	2.5	0.2	51.4	29.0	0.4	0.3	15.9	0.1	0.1
	29675	46	4.9	0.2	53.6	22.9	0.3	0.6	16.7	0.7	0.1
	Average		**3.0**	**0.2**	**52.4**	**26.9**	**0.3**	**0.4**	**16.2**	**0.2**	**0.1**
	Stdev		**1.1**	**0.0**	**0.9**	**2.4**	**0.0**	**0.1**	**0.3**	**0.2**	**0.0**
SZ	28979	3.4	2.8	1.1	60.3	12.3	0.1	0.3	22.0	0.4	0.5
	28980	13.2	3.0	1.5	59.0	11.6		0.5	22.9	0.8	0.8
	28982	24.3	3.0	0.0	59.2	12.4	0.1	0.4	22.4	1.9	0.5
	29282	19	4.6	3.3	53.6	15.7		0.4	19.7	2.0	0.7
	29297	10	4.5	2.9	55.6	12.6	0.1	0.5	21.0	2.1	0.7
	Average		**3.6**	**1.8**	**57.5**	**12.9**	**0.1**	**0.4**	**21.6**	**1.4**	**0.6**
	Stdev		**0.9**	**1.4**	**2.8**	**1.6**	**0.0**	**0.1**	**1.3**	**0.8**	**0.1**
Lesion	28543	20.6	8.2	0.0	50.7	14.4		0.5	19.8	6.2	
	28548	5.3	5.2	3.1	52.5	18.2	0.1	0.5	17.7	1.9	0.5
	28549	22	1.9	0.0	56.3	19.2	0.1	0.2	20.1	1.5	0.5
	Average		**5.1**	**1.0**	**53.2**	**17.3**	**0.1**	**0.4**	**19.2**	**3.2**	**0.5**
	Stdev		**3.1**	**1.8**	**2.9**	**2.6**	**0.0**	**0.2**	**1.3**	**2.6**	**0.0**

Multiple comparisons analysis was used to determine which compositional differences were statistically significant. The concentration of Ca and Na in sound enamel were significantly higher than either the surface zone or the lesion. Sound enamel also had a lower concentration of Cl and P relative to the other two regions. C in sound enamel was significantly lower than in the lesion, but not the surface zone, and O in the sound enamel was significantly lower than the surface zone, but not the lesion. As part of the lesion induction procedure, this sample spent a significant amount of time in a brain heart infusion (BHI) solution. BHI contains amino acids, salt, and disodium phosphate (among other components), which likely contribute to these results; the high concentration of Cl, P, and C in the lesion and surface zone areas is consistent with parts of the

BHI solution infiltrating the sample. The higher concentration of Na in the sound enamel is counterintuitive (BHI contains NaCl and NaF treatment in healthy enamel revealed that Na readily diffuses into the interphase); however the peak in the mass spectrum may have been masked by the background of the calcium peak in noisier spectra.

5.3 CONCLUSIONS

Preliminary APT of teeth affected by MIH and fluorosis confirms that, among the analyzed volumes, there was not a drastic departure from the core-shell architecture we see in healthy human enamel crystallites.[30] In both MIH and fluorosis, lesions are visible because of increased porosity, but these results suggest that this porosity persists over a larger length scale than can be captured by APT. Between the fluorosis samples, only fluorosis (patient 1) had a statistically significantly higher concentration of F than the other samples (with the exception of fluoridated, sound enamel). Crystallites in the MIH affected teeth did not show any significant differences in bulk composition from the other groups, except that the concentration of Cl was high in MIH (patient 2). In our analysis of the artificial sub-surface lesion, we found evidence that, during the formation of the lesion, enough mineral must have been dissolved out for ions and perhaps molecules from the external solution to penetrate into the lesion. These elements co-localized in relatively large pockets, and are visible in APT reconstructions.

5.4 MATERIALS AND METHODS

5.4.1 PREPARATION OF ENAMEL SECTIONS

Teeth affected by MIH and fluorosis were provided by Dr. Sophia Houari. Enamel sections were prepared similarly to those described in Section 2.4.2. Briefly, samples were embedded in

Epo-Tek 301 epoxy, sectioned so the region of interest (i.e. lesion was exposed), ground with SiC paper (600, 800, 1200 grit), and polished on a Buehler Trident polishing cloth with polycrystalline diamond suspensions (3 μm, 1 μm), rinsed and dried. Unless otherwise noted, samples were affixed to an aluminum stub using carbon tape, coated with AuPd (~25 nm) using a Denton Desk IV sputter coating system (Denton Vacuum, Moorestown, NJ). The surface of the sample was then grounded to the stub using colloidal silver paint.

5.4.2   ARTIFICIAL SUB-SURFACE LESION

Artificial sub-surface lesions were prepared using the following procedure with the assistance of Dr. Camila Zamperini, a researcher working with Professor Ana Bedran-Russo. First, teeth were sterilized overnight using gaseous ethylene oxide. Once sterilized, teeth were sectioned to isolate buccal surface from the root and lingual portions of the tooth. A 3 mm x 3 mm piece of tape was placed on the tooth surface, and the remainder of the exposed enamel was painted with nail polish to protect it from the demineralization process. After the nail polish dried, the tape was removed to provide a window in which the lesion would be induced. The bacteria *Streptococcus mutans* was grown in a solution of 100 μL concentrated *S. mutans* and 10 mL BHI for 18 hours at 5% CO_2, 37°C. A solution of 3.7 g brain and hear infusion (BHI)/50 mL nanopure H_2O was prepared and autoclaved. A saline solution (0.9% NaCl in nanopure H_2O) was also sanitized in the autoclave.

In order to establish a biofilm on the window on the buccal surface of the tooth, 9 mL of 1% sucrose in BHI was combined with 1 mL of the *S. mutans* solution described above. The tooth was placed in a well plate and incubated in this solution for 6 hours at 5% CO_2, 37°C. The solution was then replaced with 100% BHI and incubated overnight. For the next three days, every hour

and 15 minutes 8 times throughout the day, the BHI storage solution was removed, the sample was immersed in 1 mL of 10% sucrose in BHI for 3 minutes, then the sucrose solution was removed and replaced with BHI solution only and the sample was placed back in the incubator at 37°C, 5% CO_2. After 3 days, the biofilm was removed from the tooth with a toothbrush before the tooth was stored in water and refrigerated at 4°C until prepared as described above for SEM.

5.4.3 SCANNING ELECTRON MICROSCOPY (SEM)

SEM was performed using a Hitachi S4800-II or a Hitachi SU8030 (Hitachi High-Tech, Schaumburg, IL), both equipped with a cold cathode field emission electron gun, operated at an accelerating voltage of 5kV and an emission current of 8600 nA. Images were acquired using secondary electron contrast.

5.4.4 ATOM PROBE TOMOGRAPHY

Samples for APT were extracted from the various regions of interest (MIH, fluorosis, and carious lesions; surface zone enamel, and sound enamel) using a Dual Beam SEM/FIB (Helios NanoLab; FEI Company), and following the protocol described in Section 2.4.8. Briefly, a 200 nm thick layer of protective platinum was deposited using the electron beam (5 kV, 1.4 nA) on a 2 μm x 25 μm area of interest.. A thicker coating of FIB platinum (~400 nm) was then deposited using the ion beam (30 kV, 93 pA). An angled cut was then made on either side of the Pt strap, and one end was cut free and attached to an in-situ manipulator (Omniprobe, Dallas, TX) using FIB-Pt. After cutting the final side free, 1-2 μm segments were attached to the top of silicon posts on the APT array with FIB-Pt. Tips were sharpened in the ion beam using annular mill patters with progressively smaller inner and outer diameters (16-30kV, 0.28−0.47 nA). The majority of contamination/gallium implantation was removed by a final cleaning step (2 kV, 0.25 nA).

APT analysis was performed using a LEAP 5000 XS (CAMECA Instruments) with a laser operating at a wavelength of 355 nm and a pulse frequency of 250 kHz, at a power of 40 pJ. The temperature in the analysis chamber was kept 25 K, the pressure $<10^{-8}$ Pa. The DC potential on the microtip was adjusted to maintain an evaporation rate of 0.005 ions per laser pulse. 3D reconstructions of the sample tips were made using the IVAS software package (CAMECA Instruments). Standard parameters were used for all reconstructions.

6. SUMMARY AND FUTURE OUTLOOKS

6.1 SUMMARY

This work began with an introduction into the field of biomineralization, and why it is of interest to materials scientists. There was then a brief description of how the biomineral enamel is formed, its hierarchical structure down to the nanoscale crystallites, and caries as the most ubiquitous disease that affects enamel. Chapter 2 explored more deeply the structure of enamel, and investigated the chemical gradients that exist inside the crystallites themselves. It was proposed that the minority constituent ion gradients may affect both enamel's mechanical and chemical properties, and that improved understanding of these features may provide insight into the mineralization process during amelogenesis. Chapter 3 focused on the atom probe technique itself, and on studying how apatite evaporates in the high electric field of the instrument. Through this work, it appears very likely that there is some ion mobility on the sample tip. Additionally, some of the known problems with quantifying oxygen concentration in APT may be due to neutral oxygen atoms generated that do not fly through the electric field in the same way as charged fragments, and thus may not be counted in the mass spectrum.

Chapter 4 focused on x-ray diffraction studies of FIB liftouts from human enamel at orthogonal orientations, and explored the use of diffraction patterns to determine the orientation of the c-axis of the crystallites. This chapter also described changes in lattice parameter length and lattice volume of crystallites in various regions of the structure. Finally, our work supports the hypothesis that enamel crystallites are not a single coherent domain along their entire length, but more likely contain small angle grain boundaries to allow them to have a bent morphology. Finally, Chapter 5 discussed preliminary results from APT of teeth affected by 2 clinically diagnosed

pathologies (molar incisor hypomineralization and fluorosis), as well as a sample in which an artificial sub-surface lesion was induced. While the crystallite structure in the teeth affected by MIH and fluorosis seemed unaffected by those conditions, APT of the surface zone and lesion regions did not show the typical crystallite morphology, suggesting that this process has a more marked effect on the architecture of the crystallites. In this chapter, analysis of variance and multiple comparison testing was used to determine which chemical changes that occur due to these pathologies were significant, and which may be due to experimental variability.

6.2   FUTURE OUTLOOKS

6.2.1   CHEMISTRY OF THE AMORPHOUS INTERGRANULAR PHASE

In Chapter 2, we established that APT can be used to elucidate the chemical distribution in individual enamel crystallites and the amorphous intergranular phase between them. Previous work has highlighted the importance of the chemistry of the interphase region on the susceptibility to dissolution by acid.[25] Using MATLAB (or another software package) it is feasible to input the 3D APT data for further analysis of these boundaries. Creating an isosurface using the CaF concentration in the fluoridated samples would allow us to select only the intergranular region. We could then programmatically determine which side of the isosurface ions lie on on, and, by selecting only ions inside the isosurface, extract the composition of only the interphase region. This information could then be leveraged to better understand the preferential dissolution of this phase, and suggest potential treatments to decrease the solubility of the interphase. Comparison of intergranular phase concentrations from patients across many different environments could/would establish which ions can diffuse into enamel via the amorphous intergranular phase, and how those ions affect its solubility.

6.2.2 MODELING CRYSTALLITE DISSOLUTION

Now that we can resolve the impurity distribution in enamel crystallites with very high resolution, we can use this information to computationally determine the effect of chemical distribution on both mechanical and chemical properties of these crystallites. Using density functional theory (DFT) and molecular dynamics (MD) simulations, the impurity gradients can be used as inputs to create a highly accurate model of an enamel crystallite. DFT can first be used to determine how the impurities are likely incorporated into the crystallite lattice, and how the lattice changes as a result of these impurities. Given the biological variability of tooth chemistry, this method would allow for the study of different trace element concentrations without the need for large amounts of extracted teeth from different regions. The crystal structured calculated by DFT can then be used for MD simulations to model what happens to the crystallite under acidic conditions. Further, MD simulations can be used both to reveal trends in the effect of ion concentration on solubility and probe how changes to the concentrations of impurities in the crystallite core affect the dissolution rate. These trends can then be compared to experimental work for validation.

This approach to modeling crystallites can also be used to aid in the development of new treatments for the prevention of caries. Others have used MD to investigate the uptake of fluorine into hydroxyapatite, and the effect of the substitution of F^- for OH^- in the lattice on dissolution when exposed to water.[153] This type of work can be expanded to investigate different elemental substitutions, the likelihood they incorporate into enamel on a relevant time scale, and their affect on the dissolution rate of enamel. However, as the amorphous intergranular phase is particularly

sensitive to treatments and acid exposure, it's properties would need to be captured by the model as well to improve the accuracy predictions and screen potential treatments for effectiveness.[25]

6.2.3   ENAMEL CRYSTALLOGRAPHY

Our microdiffraction experiments showed that crystal lattice dimensions differ across the enamel rod, with interrod enamel having lower unit cell volume. This change in unit cell dimensions may be due to compositional differences in crystallites within a single rod, but this has yet to be verified. If the composition of crystallites varies systematically across a rod, that information is important for contextualizing our APT experiments. Since only a few crystallites can be observed at a time in APT, it is important to know if those crystallites are taken from near the interrod region or from a rod head, as the chemistry of crystallites from those regions could differ. Targeted FIB liftouts within a single rod could be used to quantify compositional differences between these regions. TEM electron diffraction of a neighboring rod could be used to verify the systematic change in lattice parameters across the rod, and allow us to correlate these lattice parameter changes to differences in concentration of impurity inclusions in the lattice.

Another important finding from our microdiffraction experiments is that hydroxyapatite crystallites in human enamel are not a single coherent domain along their entire length. Crystal counting reveals that the crystallite is more likely made of up ~100 nm long domains separated by an incoherent boundary. Morphologically, this structure likely allows the crystallites near the interrod to curve as the accepted model describes. It is important to verify these results via high resolution electron diffraction. Using the FIB/SEM, a section can be prepared with the long axis of the crystallites parallel to the long axis of the liftout. Dark-field imaging could then be used to ascertain orientation of sections of the crystallite along the *c*-axis, allowing us to quantify the

misorientation between sections and locate the boundaries between them for further analysis. This can then be used to refine the current model of enamel structure.

6.2.4 ANALYSIS OF ENAMEL PATHOLOGIES

Our preliminary analysis of teeth affected by MIH, fluorosis, and *in vitro* caries demonstrated that APT is an excellent tool for illuminating relatively small changes in minority element concentration in human enamel. While there were no apparent changes in the crystallite core-shell structure, and the Mg "sandwich" structure found in healthy enamel was still present in the crystallite core, the bulk composition did change in a significant way, especially for fluorosis. In order to fully contextualize these results and eliminate the effect of biological variability between tooth chemistry, it is important to perform APT analysis of healthy regions of the same teeth. A direct comparison between healthy and affected regions in the same tooth could then be made, allowing us to understand what is compositionally different about the lesion regions. Additional analysis across many teeth will also improve the statistical power of these results.

Using this approach across many dental diseases, we can begin to fully characterize the effect the disease has on the resulting mineral and structure. Through analyzing multiple pathologies, we can start to build a library of the impact each disease has on the chemistry and structure of enamel crystallites, and how that may in turn affect the mineral's chemical and mechanical properties. This information can then be combined with information from the biological community on how diseases affect enamel matrix proteins to formulate a mechanistic model. With such a model in place, these two scientific communities can begin to work together to formulate a way to fight caries and mitigate its effects on enamel.

REFERENCES

[1]   H. A. Lowenstam, S. Weiner, *On Biomineralization*, Oxford University Press, **1989**.

[2]   S. Mann, *Biomineralization: Principles and Concepts in Bioinorganic Materials Chemistry*, Oxford University Press, **2001**.

[3]   H. A. Lowenstam, *Science* **1981**, *211*, 1126-1131. "*Minerals formed by organisms*".

[4]   F. Nudelman, H. H. Chen, H. A. Goldberg, S. Weiner, L. Addadi, *Faraday Discussions* **2007**, *136*, 9-25. "*Spiers Memorial Lecture Lessons from biomineralization: comparing the growth strategies of mollusc shell prismatic and nacreous layers in*".

[5]   F. Nudelman, E. Shimoni, E. Klein, M. Rousseau, X. Bourrat, E. Lopez, L. Addadi, S. Weiner, *Journal of Structural Biology* **2008**, *162*, 290-300. "*Forming nacreous layer of the shells of the bivalves Atrina rigida and Pinctada margaritifera: An environmental- and cryo-scanning electron microscopy study*".

[6]   Y. Xia, M. Karahka, H. J. Kreuzer, *Journal of Applied Physics* **2015**, *118*, 7. "*Field evaporation of ZnO: A first-principles study*".

[7]   J. P. Simmer, A. S. Richardson, Y.-Y. Hu, C. E. Smith, J. Ching-Chun Hu, *International Journal of Oral Science* **2012**, *4*, 129-134. "*A post-classical theory of enamel biomineralization… and why we need one*".

[8]   A. Nanci, *Ten Cate's Oral Histology: Development, Structure, and Function*, 8 ed., C.V. Mosby Co., **2012**.

[9]   C. Robinson, R. C. Shore, S. J. Brookes, S. Strafford, S. R. Wood, J. Kirkham, *Critical Reviews in Oral Biology & Medicine* **2000**, *11*, 15. "*The Chemistry of Enamel Caries*".

[10]   L. Gordon, L. Tran, D. Joester, *ACS Nano* **2012**, *6*, 10667-10675. "*Atom Probe Tomography of Apatites and Bone-Type Mineralized Tissues*".

[11]   *Oral Health,* accessed on,

[12]   L. Torlakovic, I. Olsen, C. Petzold, H. Tiainen, B. Ογααρδ, *American Journal of Orthodontics and Dentofacial Orthopedics* **2012**, *142*, 7. "*Clinical color intensity of white spot lesions might be a better predictor of enamel demineralization depth than traditional clinical grading*".

[13]   J. Featherstone, *Australian Dental Journal* **2008**, *53*, 4. "*Dental caries: a dynamic disease process*".

[14]   *The Story of Fluoridation,* accessed on, http://www.nidcr.nih.gov/oralhealth/Topics/Fluoride/TheStoryofFluoridation.htm

[15]   *Community Water Fluoridation,* accessed on, http://www.cdc.gov/fluoridation/index.html

[16]   M. Curzon, T. Cutress, *Trace Elements and Dental Disease*, John Wright PSG Inc., Littleton, Massachusetts, USA Bristol, England, **1983**.

[17]   M. Curzon, F. Losee, *Journal of the American Dental Association* **1977**, *94*, 9. "*Dental caries and trace element composition of whole human enamel: Eastern United States*".

[18]   T. Ludwig, B. Bibby, *Caries Research* **1969**, *3*, 11. "*Geographic Variations in the Prevalence of Dental Caries in the United States of America*".

[19]   T. F. Kelly, M. K. Miller, *Review of Scientific Instruments* **2007**, *78*. "*Invited Review Article: Atom Probe Tomography*".

[20]   D. N. Seidman, K. Stiller, *MRS Bulletin* **2009**, *34*, 7. "*An Atom-Prove Tomography Primer*".

[21]   D. J. Larson, T. J. Prosa, R. M. Ulfig, B. P. Geiser, T. F. Kelly, *Local Electrode Atom Probe Tomography: A User's Guide*, Springer Science + Business Media, New York, **2013**.

[22]   E. P. Silaeva, M. Karahka, H. J. Kreuzer, *Current Opinion in Sold State and Materials Science* **2013**, *17*, 6. "*Atom Probe Tomography and Field Evaporation of Insulators and Semiconductors: Theoretical Issues*".

[23]   R. G. Forbes, *Applied Surface Science* **1995**, *87*, 11. "*Field Evaporation Theory: A review of Basic Ideas*".

[24]   P. R. Heck, F. J. Stadermann, D. Isheim, O. Auciello, T. L. Daulton, A. M. Davis, J. W. Elam, C. Floss, J. Hiller, D. J. Larson, J. B. Lewis, A. Mane, M. J. Pellin, M. R. Savina, D. N. Seidman, T. Stephan, *Meteoritics & Planetary Science* **2014**, *49*, 15. "*Atom-probe Analysis of Nanodiamonds from Allende*".

[25]   L. M. Gordon, M. J. Cohen, K. W. MacRenaris, J. D. Pasteris, T. Seda, D. Joester, *Science* **2015**, *347*, 746-750. "*Amorphous intergranular phases control the properties of rodent tooth enamel.*".

[26]   L. M. Gordon, L. Tran, D. Joester, *ACS Nano* **2012**, *6*, 9. "*Atom Probe Tomography of Apatites and Bone-Type Mineralized Tissues*".

[27]   L. M. Gordon, D. Joester, *Nature* **2011**, *469*, 4. "*Nanoscale Chemical Tomography of Buried Organic-inortanic Interfaces in the Chiton Tooth*".

[28]   L. Brian, W. Xiaoyue, G. Kathryn, *Scientific Reports* **2017**, *7*. "*Atomic scale chemical tomography of human bone*".

[29]   A. La Fontaine, A. Zavgorodniy, H. Liu, R. Zheng, M. Swain, J. Cairney, *Science Advances* **2016**, *2*. "*Atomic-scale compositional mapping reveals Mg-rich amorphous calcium phosphate in human dental enamel*".

[30]   K. A. DeRocher, P. J. M. Smeets, B. H. Goodge, M. J. Zachman, P. V. Balachandran, L. Stegbauer, M. J. Cohen, L. M. Gordon, J. M. Rondinelli, L. F. Kourkoutis, D. Joester, *Nature* **2020**, *583*, 66-71. "*Chemical Gradients in Human Enamel Crystallites*".

[31]   O. D. Klein, O. Duverger, W. Shaw, R. S. Lacruz, D. Joester, J. Moradian-Oldak, M. K. Pugach, J. T. Wright, S. E. Millar, A. B. Kulkarni, J. D. Bartlett, T. G. H. Diekwisch, P. DenBesten, J. P. Simmer, *International Journal Of Oral Science* **2017**, *9*, e3. "*Meeting report: a hard look at the state of enamel research*".

[32]   J. D. Featherstone, *Advances in Dental Research* **2009**, *21*, 4-7. "*Remineralization, the natural caries repair process--the need for new approaches*".

[33]   A. Nanci, *Ten Cate's oral histology: Development, structure and function*, **2008**.

[34]   J. Moradian-Oldak, *Frontiers In Bioscience* **2012**, *17*, 1996-2023. "*Protein-mediated enamel mineralization*".

[35]   R. S. Lacruz, S. Habelitz, J. T. Wright, M. L. Paine, *Physiological Reviews* **2017**, *97*, 939-994. "*Dental Enamel Formation and Implications for Oral Health and Disease.(Report)*".

[36]   C. Robinson, *Frontiers in Physiology* **2014**, *5*, 1-6. "*Enamel maturation: a brief background with implications for some enamel dysplasias*".

[37]   E. D. Yilmaz, G. A. Schneider, M. V. Swain, *Philosophical Transactions of the Royal Society A-Mathematical Physical and Engineering Sciences* **2015**, *373*. "*Influence of structural hierarchy on the fracture behaviour of tooth enamel*".

[38]   Y.-R. Zhang, W. Du, X.-D. Zhou, H.-Y. Yu, *International Journal of Oral Science* **2014**, *6*, 61-69. "*Review of research on the mechanical properties of the human tooth*".

[39]   J. Teruel, A. Alcolea, A. Hernández, A. Ortiz-Ruiz, *Archives of Oral Biology* **2015**, *60*. "*Comparison of chemical composition of enamel and dentine in human, bovine, porcine and ovine teeth*".

[40]   T. Yanagisawa, Y. Miake, *Journal of Electron Microscopy* **2003**, *52*, 8. "*High-resolution electron microscopy of enamel-crystal demineralization and remineralization in carious lesions*".

[41]   J. Reyes-Gasga, J. Hemmerle, E. F. Bres, *Microscopy and Microanalysis* **2016**, *22*, 9. "*Aberration-Corrected Transmission Electron Microscopy Study of the Central Dark Line Defect in Human Tooth Enamel Crystals*".

[42]   D. A. Muller, *Nature materials* **2009**, *8*, 263-270. "*Structure and bonding at the atomic scale by scanning transmission electron microscopy*".

[43]   J. Miao, P. Ercius, S. J. Billinge, *Science* **2016**, *353*, aaf2157. "*Atomic electron tomography: 3D structures without crystals*".

[44]   B. H. Savitzky, I. El Baggari, C. B. Clement, E. Waite, B. H. Goodge, D. J. Baek, J. P. Sheckelton, C. Pasco, H. Nair, N. J. Schreiber, J. Hoffman, A. S. Admasu, J. Kim, S.-W. Cheong, A. Bhattacharya, D. G. Schlom, T. M. McQueen, R. Hovden, L. F. Kourkoutis, *Ultramicroscopy* **2018**, *191*, 56-65. "*Image registration of low signal-to-noise cryo-STEM data*".

[45]   E. F. Bres, J. L. Hutchison, B. Senger, J. C. Voegel, R. M. Frank, *Ultramicroscopy* **1991**, *35*, 17. "*HREM study of irradiation damage in human dental enamel crystals*".

[46]   A. Meldrum, L. M. Wang, R. C. Ewing, *American Mineralogist* **1997**, *82*, 858-869. "*Electron-irradiation-induced phase segregation in crystalline and amorphous apatite: A TEM study*".

[47]   D. A. Muller, L. F. Kourkoutis, M. Murfitt, J. H. Song, H. Y. Hwang, J. Silcox, N. Dellby, O. L. Krivanek, *Science* **2008**, *319*, 1073. "*Atomic-Scale Chemical Imaging of Composition and Bonding by Aberration-Corrected Microscopy*".

[48]   R. F. Egerton, P. Li, M. Malac, *Micron* **2004**, *35*, 399-409. "*Radiation damage in the TEM and SEM*".

[49]   J. S. Wall, *Contamination in the STEM at ultrahigh vacuum*, SEM Inc., Chicago, **1980**.

[50]   S. Butterworth, *Experimental Wireless & the Wireless Engineer* **1930**, *7*, 536–541. "*On the theory of filter amplifiers*".

[51]   R. Egerton, *Electron Energy Loss Spectroscopy in the TEM, Vol. 72*, **2009**.

[52]   J. L. Hart, A. C. Lang, A. C. Leff, P. Longo, C. Trevor, R. D. Twesten, M. L. Taheri, *Scientific Reports* **2017**, *7*. "*Direct Detection Electron Energy-Loss Spectroscopy: A Method to Push the Limits of Resolution and Sensitivity*".

[53]   A. de Juan, R. Tauler, *Critical Reviews in Analytical Chemistry* **2006**, *36*, 163-176. "*Multivariate Curve Resolution (MCR) from 2000: Progress in Concepts and Applications*".

[54]   D. Li, M. S. Peng, T. Murata, *Canadian Mineralogist* **1999**, *37*, 199-206. "*Coordination and local structure of magnesium in silicate minerals and glasses: MgK-edge XANES study*".

[55]   M. J. Cohen, Northwestern University (Evanston, IL), **2014**.

[56]   K. Thompson, D. Lawrence, D. J. Larson, J. D. Olson, T. F. Kelly, B. Gorman, *Ultramicroscopy* **2007**, *107*, 131-139. "*In situ site-specific specimen preparation for atom probe tomography*".

[57]   L. M. Gordon, L. Tran, D. Joester, *ACS nano* **2012**, *6*, 10667-10675. "*Atom probe tomography of apatites and bone-type mineralized tissues*".

[58]   L. M. Gordon, D. Joester, *Frontiers in Physiology* **2015**, *6*. "*Mapping residual organics and carbonate at grain boundaries and in the amorphous interphase in mouse incisor enamel*".

[59]   C. Robinson, J. Kirkham, S. J. Brookes, W. A. Bonass, R. C. Shore, *The International journal of developmental biology* **1995**, *39*, 145-152. "*The chemistry of enamel development*".

[60]   C. Robinson, J. A. Weatherell, A. S. Hallsworth, *Caries Research* **1981**, *15*, 70-77. "*Distribution of Magnesium in Mature Human Enamel*".

[61]   *Periodic table of the elements,* accessed on, http://www.mrl.ucsb.edu/~seshadri/Periodic/

[62]   J. Hughes, M. Cameron, K. Crowley, *Structural Variations in Natural F, OH, and Cl Apatites, Vol. 74*, **1989**.

[63]   F. C. M. Driessens, J. W. E. van Dijk, J. M. P. M. Borggreven, *Calcified Tissue Research* **1978**, *26*, 127-137. "*Biological calcium phosphates and their role in the physiology of bone and dental tissues I. Composition and solubility of calcium phosphates*".

[64]   D. Laurencin, N. Almora-Barrios, N. H. de Leeuw, C. Gervais, C. Bonhomme, F. Mauri, W. Chrzanowski, J. C. Knowles, R. J. Newport, A. Wong, Z. Gan, M. E. Smith, *Biomaterials* **2011**, *32*, 1826-1837. "*Magnesium incorporation into hydroxyapatite*".

[65]   R. D. Shannon, C. T. Prewitt, *Acta Crystallographica Section B* **1969**, *25*, 925-946. "*Effective ionic radii in oxides and fluorides*".

[66]   J. M. Hughes, M. Cameron, K. D. Crowley, *American Mineralogist* **1989**, *74*, 870-876. "*Structural variations in natural F, OH, and Cl apatites*".

[67] R. Z. LeGeros, T. Sakae, C. Bautista, M. Retino, J. P. Legeros, *Advances in Dental Research* **1996**, *10*, 225-231. "*Magnesium and Carbonate in Enamel and Synthetic Apatites*".

[68] S. Ben Abdelkader, I. Khattech, C. Rey, M. Jemal, *Thermochimica Acta* **2001**, *376*, 25-36. "*Synthése, caractérisation et thermochimie d'apatites calco-magnésiennes hydroxylées et fluorées*".

[69] O. Babushkin, T. Lindbäck, A. Holmgren, J. Li, L. Hermansson, *Journal of Materials Chemistry* **1994**, *4*, 413-415. "*Thermal expansion of hot isostatically pressed hydroxyapatite*".

[70] A. C. Deymier, A. K. Nair, B. Depalle, Z. Qin, K. Arcot, C. Drouet, C. H. Yoder, M. J. Buehler, S. Thomopoulos, G. M. Genin, J. D. Pasteris, *Biomaterials* **2017**, *127*, 75-88. "*Protein-free formation of bone-like apatite: New insights into the key role of carbonation*".

[71] J. C. Voegel, R. M. Frank, *Calcified Tissue Research* **1977**, *24*, 19-27. "*Stages in dissolution of human enamel crystals in dental-caries*".

[72] H. Tohda, S. Takuma, N. Tanaka, *Journal of Dental Research* **1987**, *66*, 1647-1653. "*Intercrystalline structure of enamel crystals affected by caries*".

[73] H. J. Gao, B. H. Ji, I. L. Jager, E. Arzt, P. Fratzl, *Proceedings of the National Academy of Sciences of the United States of America* **2003**, *100*, 5597-5600. "*Materials become insensitive to flaws at nanoscale: Lessons from nature*".

[74] M. Yahyazadehfar, J. Ivancik, H. Majd, B. B. An, D. S. Zhang, D. Arola, *Applied Mechanics Reviews* **2014**, *66*, 03080301-03080319. "*On the Mechanics of Fatigue and Fracture in Teeth*".

[75] A. Stoffers, J. Barthel, C. H. Liebscher, B. Gault, O. Cojocaru-Mirédin, C. Scheu, D. Raabe, M. Thuvander, J. Cairney, S. Gerstl, **2017**, *23*, 291-299. "*Correlating Atom Probe Tomography with Atomic-Resolved Scanning Transmission Electron Microscopy: Example of Segregation at Silicon Grain Boundaries*".

[76] M. Šupová, *Ceramics International* **2015**, *41*. "*Substituted hydroxyapatites for biomedical applications: A review*".

[77] K. J. Roche, K. T. Stanton, *Journal of Fluorine Chemistry* **2014**, *161*, 102-109. "*Measurement of fluoride substitution in precipitated fluorhydroxyapatite nanoparticles*".

[78] M. S. Sader, K. Lewis, G. A. Soares, R. Z. LeGeros, *Materials Research* **2013**, *16*, 779-784. "*Simultaneous incorporation of magnesium and carbonate in apatite: effect on physico-chemical properties*".

[79] F. Yao, J. P. LeGeros, R. Z. LeGeros, *Acta Biomater* **2009**, *5*, 2169-2177. "*Simultaneous incorporation of carbonate and fluoride in synthetic apatites: Effect on crystallographic and physico-chemical properties*".

[80] M. Fleet, X. Liu, *American Mineralogist - AMER MINERAL* **2008**, *93*, 1460-1469. "*Accommodation of the carbonate ion in fluorapatite synthesized at high pressure*".

[81] G. Daculsi, B. Kerebel, *Journal of Ultrastructure Research* **1978**, *65*, 163-172. "*High-resolution electron-microscope study of human enamel crystallites - size, shape, and growth*".

[82] E. Beniash, R. A. Metzler, R. S. Lam, P. U. Gilbert, *Journal of Structural Biology* **2009**, *166*, 133-143. "*Transient amorphous calcium phosphate in forming enamel*".

[83] C. Robinson, P. Fuchs, J. A. Weatherell, *Journal of Crystal Growth* **1981**, *53*, 160-165. "*The appearance of developing rat incisor enamel using a freeze fracturing technique*".

[84] J. Kirkham, A. Firth, D. Vernals, N. Boden, C. Robinson, R. C. Shore, S. J. Brookes, A. Aggeli, *Journal of Dental Research* **2007**, *86*, 426-430. "*Self-assembling Peptide Scaffolds Promote Enamel Remineralization*".

[85] H. U. Luder, C. Gerth-Kahlert, S. Ostertag-Benzinger, D. F. Schorderet, *Plos One* **2013**, *8*, 1-7. "*Dental Phenotype in Jalili Syndrome Due to a c.1312 dupC Homozygous Mutation in the CNNM4 Gene*".

[86] D. Yamazaki, Y. Funato, J. Miura, S. Sato, S. Toyosawa, K. Furutani, Y. Kurachi, Y. Omori, T. Furukawa, T. Tsuda, S. Kuwabata, S. Mizukami, K. Kikuchi, H. Miki, *Plos Genetics* **2013**, *9*, 1-14. "*Basolateral Mg2+ Extrusion via CNNM4 Mediates Transcellular Mg2+ Transport across Epithelia: A Mouse Model*".

[87] Y. Nakano, M. H. Le, D. Abduweli, S. P. Ho, L. V. Ryazanova, Z. X. Hu, A. G. Ryazanov, P. K. Den Besten, Y. Zhang, *Frontiers in Physiology* **2016**, *7*, 1-11. "*A Critical Role of TRPM7 As an Ion Channel Protein in Mediating the Mineralization of the Craniofacial Hard Tissues*".

[88] T. Aoba, S. Shimoda, E. C. Moreno, *Journal of Dental Research* **1992**, *71*, 1826-1831. "*Labile or Surface Pools of Magnesium, Sodium, and Potassium in Developing Porcine Enamel Mineral*".

[89] H. Chai, J. J. W. Lee, P. J. Constantino, P. W. Lucas, B. R. Lawn, *Proceedings of the National Academy of Sciences of the United States of America* **2009**, *106*, 7289-7293. "*Remarkable resilience of teeth*".

[90] M. J. Hubbard, J. E. Mangum, V. A. Perez, G. J. Nervo, R. K. Hall, *Frontiers in Physiology* **2017**, *8*. "*Molar Hypomineralisation: A Call to Arms for Enamel Researchers*".

[91] Y. C. Park, B. C. Park, S. Romankov, K. J. Park, J. H. Yoo, Y. B. Lee, J.-M. Yang, *Journal of Microscopy* **2014**, *255*, 180-187. "*Use of permanent marker to deposit a protection layer against FIB damage in TEM specimen preparation*".

[92] M. J. Zachman, Z. Y. Tu, S. Choudhury, L. A. Archer, L. F. Kourkoutis, *Nature* **2018**, *560*, 345-+. "*Cryo-STEM mapping of solid-liquid interfaces and dendrites in lithium-metal batteries*".

[93] B. Ravel, M. Newville, *Journal of Synchrotron Radiation* **2005**, *12*, 537-541. "*ATHENA, ARTEMIS, HEPHAESTUS: data analysis for X-ray absorption spectroscopy using IFEFFIT*".

[94] S. M. Antao, W. H. Mulder, I. Hassan, W. A. Crichton, J. B. Parise, *American Mineralogist* **2004**, *89*, 1142-1147. "*Cation disorder in dolomite, CaMg(CO3)(2), and its influence on the aragonite plus magnesite <-> dolomite reaction boundary*".

[95] W. A. Dollase, R. J. Reeder, *American Mineralogist* **1986**, *71*, 163-166. "*Crystal-structure refinement of huntite, CaMg3(CO3)4, with x-ray-powder data*".

[96] C. Calvo, R. Gopal, *American Mineralogist* **1975**, *60*, 120-133. "*Crystal-structure of whitlockite from Palermo Quarry*".

[97] J. J. Rehr, R. C. Albers, *Reviews of Modern Physics* **2000**, *72*, 621-654. "*Theoretical approaches to x-ray absorption fine structure*".

[98] R. J. Reeder, G. M. Lamble, P. A. Northrup, *American Mineralogist* **1999**, *84*, 1049-1060. "*XAFS study of the coordination and local relaxation around Co2+, Zn2+, Pb2+, and Ba2+ trace elements*".

[99] C. Holt, M. Vankemenade, J. E. Harries, L. S. Nelson, R. T. Bailey, D. W. L. Hukins, S. S. Hasnain, P. L. Debruyn, *Journal of Crystal Growth* **1988**, *92*, 239-252. "*Preparation of amorphous calcium-magnesium phosphates at pH-7 and characterization by x-ray absorption and fourier-transform infrared-spectroscopy*".

[100] J. E. Harries, D. W. L. Hukins, C. Holt, S. S. Hasnain, *Journal of Crystal Growth* **1987**, *84*, 563-570. "*Conversion of amorphous calcium-phosphate into hydroxyapatite investigated by EXAFS spectroscopy*".

[101] M.-l. Qi, G.-y. Xiao, Y.-p. Lu, *Acta Metallurgica Sinica (English Letters)* **2016**, *29*, 609-613. "*Rapid Hydrothermal Synthesis of Submillimeter Ultralong Flexible Hydroxyapatite Fiber Using Different pH Regulators*".

[102] O. V. Dolomanov, L. J. Bourhis, R. J. Gildea, J. A. K. Howard, H. Puschmann, *Journal of Applied Crystallography* **2009**, *42*, 339-341. "*OLEX2 : a complete structure solution, refinement and analysis program*".

[103] G. M. Sheldrick, *Acta Crystallographica, Section C: Crystal Structure Communications* **2015**, *71*, 3-8. "*Crystal structure refinement with SHELXL*".

[104] J. P. Perdew, A. Ruzsinszky, G. I. Csonka, O. A. Vydrov, G. E. Scuseria, L. A. Constantin, X. Zhou, K. Burke, *Physical Review Letters* **2008**, *100*, 4. "*Restoring the Density-Gradient Expansion for Exchange in Solids and Surfaces*".

[105] P. Giannozzi, S. Baroni, N. Bonini, M. Calandra, R. Car, C. Cavazzoni, D. Ceresoli, G. L. Chiarotti, M. Cococcioni, I. Dabo, A. D. Corso, S. d. Gironcoli, S. Fabris, G. Fratesi, R. Gebauer, U. Gerstmann, C. Gougoussis, A. Kokalj, M. Lazzeri, L. Martin-Samos, N. Marzari, F. Mauri, R. Mazzarello, S. Paolini, A. Pasquarello, L. Paulatto, C. Sbraccia, S. Scandolo, G. Sclauzero, A. P. Seitsonen, A. Smogunov, P. Umari, R. M. Wentzcofitch, *Journal of Physics: Condensed Matter* **2009**, *21*, 1-19. "*QUANTUM EXPRESSO: a modular and open-source software project for quantum simulations of materials*".

[106] D. Vanderbilt, *Physical Review B: Condensed Matter and Materials Physics* **1990**, *41*, 7892-7895. "*Soft self-consistent pseudopotentials in a generalized eigenvalue formalism*".

[107] A. D. Corso, *Computational Materials Science* **2014**, *95*, 337-350. "*Pseudopotentials periodic table: From H to Pu*".

[108] *WebPlotDigitizer,* accessed on, https://automeris.io/WebPlotDigitizer/

[109] D. W. Saxey, *Ultramicroscopy* **2011**, *111*, 7. "*Correlated Ion Analysis and the Interpretation of Atom Probe Mass Spectra*".

[110] D. Santhanagopalan, D. K. Schreiber, D. E. Perea, R. L. Martens, Y. Janssen, P. Khalifah, Y. S. Meng, *Ultramicroscopy* **2015**, *148*, 57-66. "*Effects of laser energy and wavelength on the analysis of LiFePO4 using laser assisted atom probe tomography*".

[111] A. H. Meckel, W. J. Griebstein, R. J. Neal, *Archives of Oral Biology* **1965**, *10*, 775-783. "*Structure of Mature Human Dental Enamel as Observed by Electron Microscopy*".

[112] D. F. G. Poole, A. W. Brooks, *Arch Oral Biol* **1961**, *5*, 14-26. "*The Arrangement of Crystallites in Enamel Prisms*".

[113] A. Boyde, in *Scientific Foundations of Dentistry* (Eds.: B. Cohen, I. R. Kramer), William Heinemann Medical Books Ltd., London, **1976**, pp. 341-343.

[114] S. Habelitz, *Journal of dental research* **2015**, *94*, 759-767. "*Materials engineering by ameloblasts*".

[115] A. Boyde, *Proc R Soc Med* **1967**, *60*, 923-928. "*The development of enamel structure*".

[116] T. Yanagisawa, Y. Miake, *Microscopy* **2003**, *52*, 605-613. "*High-resolution electron microscopy of enamel-crystal demineralization and remineralization in carious lesions*".

[117] B. Kerebel, G. Daculsi, L. M. Kerebel, *Journal of Dental Research* **1979**, *58*, 844-851. "*Ultrastructural Studies of Enamel Crystallites*".

[118] M. Al-Jawad, O. Addison, M. A. Khan, A. James, C. J. Hendriksz, *Journal of Dentistry* **2012**, *40*, 1074-1080. "*Disruption of enamel crystal formation quantified by synchrotron microdiffraction*".

[119] M. Al-Mosawi, G. R. Davis, A. Bushby, J. Montgomery, J. Beaumont, M. Al-Jawad, *Scientific Reports* **2018**, *8*. "*Crystallographic texture and mineral concentration quantification of developing and mature human incisal enamel*".

[120] L. M. Simmons, M. Al-Jawad, S. H. Kilcoyne, D. J. Wood, *European Journal of Oral Sciences* **2011**, *119*, 19-24. "*Distribution of enamel crystallite orientation through an entire tooth crown studied using synchrotron X-ray diffraction*".

[121] J. Xue, A. V. Zavgorodniy, B. J. Kennedy, M. V. Swain, W. Li, *Journal of Microscopy* **2013**, *251*, 144-153. "*X-ray microdiffraction, TEM characterization and texture analysis of human dentin and enamel*".

[122] J. E. Glas, *Archives of Oral Biology* **1962**, *7*, 91-IN15. "*Studies on the ultrastructure of dental enamel—II: The orientation of the apatite crystallites as deduced from X-ray diffraction*".

[123] M. Al-Jawad, A. Steuwer, S. H. Kilcoyne, R. C. Shore, R. Cywinski, D. J. Wood, *Biomaterials* **2007**, *28*, 2908-2914. "*2D mapping of texture and lattice parameters of dental enamel*".

[124] R. Free, K. DeRocher, R. Xu, D. Joester, S. R. Stock, *Advances in X-ray Analysis* **2020**, *Accepted*. "*A Method for Mapping Submicron-Scale Crystallographic Order/Disorder Applied to Human Tooth Enamel*".

[125] R. A. Young, P. E. Mackie, *Materials Research Bulletin* **1980**, *15*, 17-29. "*Crystallography of Human Tooth Enamel: Initial Structure Refinement*".

[126] R. M. Wilson, J. C. Elliott, S. E. P. Dowker, *American Mineralogist* **1999**, *84*, 1406-1414. "*Rietveld refinement of the crystallographic structure of human dental enamel apatites*".

[127] C. Robinson, R. Shore, S. Brookes, S. Strafford, S. Wood, J. Kirkham, *Critical Reviews in Oral Biology & Medicine* **2000**, *11*, 481. "*The chemistry of enamel caries*".

[128] J. C. Elliott*, Vol. 48*, **2002**, pp. 427-453.

[129] E. C. Moreno, T. Aoba, *Calcified Tissue International* **1991**, 6-13. "*Comparative Solubility Study of Human Dental Enamel, Dentin, and Hydroxyapatite*".

[130] R. A. Young, W. E. Brown, in *Biological Mineralization and Demineralization* (Ed.: G. H. Nancollas), Springer Berlin Heidelberg, Berlin, Heidelberg, **1982**, pp. 101-141.

[131] R. Z. LeGeros, *Nature* **1965**, 403-404. "*Effect of Carbonate on the Lattice Parameters of Apatite*".

[132] J. D. Featherstone, I. Mayer, F. C. M. Driessens, R. M. H. Verbeeck, H. J. M. Heijligers, *Calcified Tissue International* **1983**, *35*, 169-171. "*Synthetic Apatites Containing Na, Mg, and CO3 and Their Comparison with Tooth Enamel Mineral*".

[133] J. Li, University of Birmingham (Birmingham, UK), **2010**.

[134] B. D. Cullity, S. R. Stock, *Elements of X-ray Diffraction*, 3rd ed., Pearson, **2001**.

[135] K. Little, *Journal of the Royal Microscopical Society* **1958**, *78*, 58-66. "*IV.—ELECTRON MICROSCOPE STUDIES ON HUMAN DENTAL ENAMEL*".

[136] G. Daculsi, L. Menanteau, L. M. Kerebel, D. Mitre, *Calcified Tissue International* **1984**, *36*, 550-555. "*Length and Shape of Enamel Crystals*".

[137] C. A. Grove, G. Judd, G. S. Ansell, *J Dent Res* **1972**, *51*, 22-29. "*Determination of hydroxyapatite crystallite size in human dental enamel by dark-field electron microscopy*".

[138] C. A. Schneider, W. S. Rasband, K. W. Eliceiri, *Nature Methods* **2012**, *9*, 671-675. "*NIH Image to ImageJ: 25 years of image analysis*".

[139] A. P. Hammersley, S. O. Svensson, M. Hanfland, A. N. Fitch, D. Hausermann, *High Pressure Research* **1996**, *14*, 235-248. "*Two-Dimensional Detector Software: From Real Detector to Idealised Image or Two-Theta Scan*".

[140] J. I. Langford, A. J. C. Wilson, *Journal of Applied Crystallography* **1977**, *11*, 102-113. "*Scherrer after Sixty years: A Survey and Some New Results in the Determination of Crystallite Size*".

[141] W. H. Hall, *Proc. Phys. Soc. Sect. A* **1949**, *62*, 741-743. "*X-ray line broadening in metals*".

[142] N. Garg, A. K. Jain, S. Saha, J. Singh, *Int J Clin Pediatr Dent* **2012**, *5*, 190-196. "*Essentiality of early diagnosis of molar incisor hypomineralization in children and review of its clinical presentation, etiology and management*".

[143] S. Bhaskar, S. Hegde, *Journal of Indian Society of Pedodontics and Preventive Dentistry* **2014**, *32*, 322-329. "*Molar-incisor hypomineralization: Prevalence, severity and clinical characteristics in 8- to 13-year-old children of Udaipur, India*".

[144] K. L. Weerheijm, *Eur J Paediatr Dent* **2003**, *4*, 114-120. "*Molar incisor hypomineralisation (MIH)*".

[145] W. H. Bowen, *The Journal of the American Dental Association* **2002**, *133*, 1405-1407. "*Fluorosis: Is it really a problem?*".

[146] P. DenBesten, W. Li, *Monogr Oral Sci* **2011**, *22*, 81-96. "*Chronic fluoride toxicity: dental fluorosis*".

[147] P. K. DenBesten, Y. Yan, J. D. Featherstone, J. F. Hilton, C. E. Smith, W. Li, *Arch Oral Biol* **2002**, *47*, 763-770. "*Effects of fluoride on rat dental enamel matrix proteinases*".

[148] T. Yanagisawa, S. Takuma, O. Fejerskov, *Adv Dent Res* **1989**, *3*, 203-210. "*Ultrastructure and composition of enamel in human dental fluorosis*".

[149] T. Yanagisawa, S. Takuma, H. Tohda, O. Fejerskov, R. W. Fearnhead, *J Electron Microsc (Tokyo)* **1989**, *38*, 441-448. "*High resolution electron microscopy of enamel crystals in cases of human dental fluorosis*".

[150] C. Robinson, K. Yamamoto, S. D. Connell, J. Kirkham, H. Nakagaki, A. D. Smith, *Eur J Oral Sci* **2006**, *114 Suppl 1*, 99-104; discussion 127-109, 380. "*The effects of fluoride on the nanostructure and surface pK of enamel crystals: an atomic force microscopy study of human and rat enamel*".

[151] O. Fejerskov, N. W. Johnson, L. M. Silverstone, *Scand J Dent Res* **1974**, *82*, 357-372. "*The ultrastructure of fluorosed human dental enamel*".

[152] S. Guzman-Armstrong, J. Chalmers, J. J. Warren, *American Journal of Orthodontics and Dentofacial Orthopedics* **2010**, *138*, 690-696. "*White spot lesions: Prevention and treatment*".

[153] N. H. de Leeuw, *The Journal of Physical Chemistry B* **2004**, *108*, 1809-1811. "*Resisting the Onset of Hydroxyapatite Dissolution through the Incorporation of Fluoride*".